THEORETICAL STUDY OF THE DYNAMIC RESPONSE OF A CHIMNEY* TO EARTHQUAKE AND WIND

Prepared by

T.Y. Yang, L.C. Shiau, Hsu Lo, and J.L. Bogdanoff

School of Aeronautics and Astronautics
Purdue University
West Lafayette, Indiana

Submitted to

THE NATIONAL SCIENCE FOUNDATION

April 1, 1978

---

*Tennessee Valley Authority (TVA) Power Plant Unit #3, at Paradise, Kentucky.

50272-101

REPORT DOCUMENTATION PAGE	1. REPORT NO. NSF/RA-780527	2.	3. Recipient's Accession No. PB293561

4. Title and Subtitle
Theoretical Study of the Dynamic Response of A Chimney * to Earthquake and Wind

5. Report Date
April 1, 1978

6.

7. Author(s)
T.Y. Yang, L.C. Shiau, H. Lo, J.L. Bogdanoff

8. Performing Organization Rept. No.

9. Performing Organization Name and Address
Purdue University
School of Aeronautics and Astronautics
West Lafayette, Indiana

10. Project/Task/Work Unit No.

11. Contract(C) or Grant(G) No.
(C)
(G) ENV74051575

12. Sponsoring Organization Name and Address
Applied Science and Research Applications (ASRA)
National Science Foundation
1800 G Street, N.W.
Washington, D.C. 20550

13. Type of Report & Period Covered

14.

15. Supplementary Notes
* Tennessee Valley Authority (TVA) Power Plant Unit #3, at Paradise, Kentucky

16. Abstract (Limit: 200 words)

Analytical studies of the elastic and inelastic responses of a chimney to an earthquake are performed. The chimney studied is at the steam generating plant at Paradise, Kentucky of Tennessee Valley Authority. The report describes the geometry and the material property of the chimney at a TVA Power Plant. An existing computer program SAP IV is employed to study the elastic response of the chimney. Both time history and response spectrum analyses are employed to obtain the displacements and forces at various heights of the chimney. A simple method is developed to generate the ground response spectrum as the input data for the response spectrum analysis. In the description of the inelastic response of a chimney to an earthquake, the plastic bending analysis of a chimney is described first. By using the initial strain concept to treat the effects of plastic strains, a governing linear matrix equation is established. Based on the equations and the procedure developed, the behavior of a chimney subjected to cyclic loading is then analyzed. A general equation for the relationship between moment and curvature is derived. The plastic strain distributions in the element at any stage are found through this relationship. Finally, the inelastic response of the chimney is solved by using a step-by-step integration method coupled with the governing equations and the moment curvature relationship. A computer program is developed to predict the inelastic dynamic behavior of the chimney.

17. Document Analysis a. Descriptors

Earthquakes
Seismology
Wind
Dynamic structural analysis
Earthquake resistant structures
Chimneys
Dynamic response

b. Identifiers/Open-Ended Terms

Tennessee Valley Authority
Paradise, Kentucky

c. COSATI Field/Group

18. Availability Statement	19. Security Class (This Report)	21. No. of Pages
NTIS		151
	20. Security Class (This Page)	22. Price PCA07/MF A01

(See ANSI-Z39.18) See Instructions on Reverse

OPTIONAL FORM 272 (4-77)
(Formerly NTIS-35)
Department of Commerce

THEORETICAL STUDY OF THE DYNAMIC RESPONSE OF A CHIMNEY* TO EARTHQUAKE AND WIND

Prepared by

T.Y. Yang, L.C. Shiau, Hsu Lo, and J.L. Bogdanoff

School of Aeronautics and Astronautics
Purdue University
West Lafayette, Indiana

Submitted to

THE NATIONAL SCIENCE FOUNDATION

April 1, 1978

---

*Tennessee Valley Authority (TVA) Power Plant Unit #3, at Paradise, Kentucky.

Contents

Abstract

An analytical investigation of the response of chimney to earthquake and wind is presented in this report. The 823 foot tall chimney is modeled using Bernoulli-Euler beam finite elements. The modal superposition method is used for analyzing the elastic response while the numerical direct integration method is used to solve the equations for the inelastic response. A mathematical model that enables one to predict the vortex-excited resonant responses of two cylinders in line in the wind direction is developed.

For the elastic case, the cracks developed in the chimney and the effect of the shear deformation are considered. Several assumed values of the critical damping are included in the analysis. The stress distributions around the flue openings are found by using quadrilateral plate finite elements. The comparison of the results between time history analysis and response spectrum analysis is made.

For the inelastic case, the material is assumed to have elastic-perfectly plastic behavior. Moment-curvature equations for a pipe-type section are derived and combined with the Wilson-θ method to predict the inelastic dynamic response of the chimney.

For the dynamic response of cylinder to wind, a modified ven der Pol equation is employed as the governing equation for the fluctuating lift on the cylinder and is combined with the equation of motion for the cylinder. The results are compared with available experimental data.

Part I

Dynamic Response of a Tall Chimney to an Earthquake

I. INTRODUCTION

Due to the increasing demands for air pollution control, the height of tall chimneys has been steadily increasing to satisfy these requirements. With the increase in the height of these chimneys, their resistance to dynamic forces such as earthquakes and winds becomes increasingly critical. A survay of literature shows that the studies of the dynamic behavior, especially the inelastic dynamic behavior, of a tall slender chimney subjected to a moderate earthquake has not received as much attention as that of tall buildings or other tower structures (5, 8, 9, 12, 13, 14, 19). Although many design codes provide some guidelines for estimating the dynamic forces and the corresponding displacements of the chimney, a more detailed and reliable analysis method for both elastic and inelastic dynamic responses of the chimney is still lacking.

Rumman (17), in 1967, presented a paper on the earthquake forces on reinforced concrete chimneys. In his paper, the elastic response of the chimney to earthquake forces was computed by the mode-superposition method. He used the Stodola method to calculate the natural modes of the chimney. Recently, a number of investigators (1, 4, 10, 11, 16, 20) used either the mode-superposition method or a step-by-step direct integration method to analyze the dynamic behavior of a tall chimney. Their studies were also concentrated on the elastic response of the chimney to earthquake. During a major earthquake, the resulting deformations and stresses developed in the chimney may exceed the elastic limit of the structural materials. In that case, the structural response cannot be assumed to be linearly elastic.

The determination of inelastic response for a chimney or other structures having distributed mass and load is extremely difficult because the direction of the dynamic force changes from time to time. This will cause the material properties, moment curvature relationship and initial strains to change with time as well. In order to simplify such complexity, a number of investigators (9, 18, 19) assumed an idealized elastic-plastic moment curvature relationship to study the inelastic response of tall buildings or frames. The structure is initially treated as an elastic system. When the bending moment at certain section reaches its ultimate bending capacity, it is assumed that an idealized plastic hinge has formed at this section and a new elastic system is obtained. The analysis is continued until a second hinge is formed or the rotation of the first hinge reverses in direction, thus indicating that this point returns to elastic range again. This type of analysis is applied only to structures having many degrees of structural redundancy. For a static determinate structure, such as a free standing chimney, this kind of analysis is not applicable because the structure will fail when the bending moment at any point reaches the ultimate bending capacity. Therefore, a different approach must be established for the study of inelastic response of the chimney.

The purpose of this research is to perform analytical studies of the elastic and inelastic responses of a chimney to an earthquake. The chimney studied is the one at the steam generating plant at Paradise, Kentucky of Tennessee Valley Authority. Chapter II describes the geometry and the material property of the chimney at a TVA Power Plant. The 823 foot tall chimney is modeled by eight pipe-type beam finite elements

and the base beam element is remodeled by 244 quadrilateral plate elements for studying the stress concentrations around the flue openings. Chapter III briefly describes the elements and the formulations used for the analysis.

In Chapter IV, an existing computer program SAP IV is employed to study the elastic response of the chimney. Several assumed values of damping coefficients are included in the analysis. Both time history and response spectrum analyses are employed to obtain the displacements and forces at various heights of the chimney. A simple method is developed to generate the ground response spectrum as the input data for the response spectrum analysis.

Chapter V describes the inelastic response of a chimney to an earthquake. The plastic bending analysis of a chimney is described first. By using the initial strain concept to treat the effects of plastic strains, a governing linear matrix equation is established to analyze the problem. The incremental procedure is used in the solution of the governing matrix equations. Based on the equations and the procedure developed, the behavior of a chimney subjected to cyclic loading is then analyzed. A general equation for the relationship between moment and curvature is derived. The plastic strain distributions in the element at any stage are found through this relationship. Finally, the inelastic response of the chimney is solved by using a step-by-step integration method coupled with the governing equations and the moment curvature relationship. A computer program is finally developed to predict the inelastic dynamic behavior of the chimney.

II. System Description and Modeling

The chimney studied here is the one at the Steam Generating Plant at Paradise, Kentucky of Tennessee Valley Authority. The chimney is composed of two slender cylindrical reinforced concrete shells as shown in Figure 2.1. The inner shell serves as a liner and has two inches fiber glass insulation on its outer surface. The inner shell also has a stainless steel cap at the top covering the gap between the inner and outer shells. There is no significant structural connection between the two shells. There is a 4 feet 6 inches minimum air space between the two shells.

The foundation of the chimney is imbedded in limestone rock. It is assumed to be fixed against rotation and lateral displacement at an elevation of 390 feet. The height of the chimney is 823 feet above the foundation. Each of the two shells has a pair of side flue openings. They are rectangular in shape with dimensions of 28 feet by 14 feet. The base lines of the openings are 73.5 feet above the chimney base. The circumferential distance between the center lines of the two openings is 50 feet for the outer shell and 38 feet for the inner shell. Each opening at the inner shell is connected to the opening at the outer shell by steel framed flue duct. The concrete around the openings is heavily reinforced.

The yielding strength of the A432 reinforcing steel is 60,000 psi and the ultimate compressive strength of the concrete is 4,300 psi. According to the recommendation of the TVA, the modulus of elasticity is 4.5×10^6 psi for the concrete and 29×10^6 psi for the reinforcing steel.

Figure 2.2 shows the assumed stress-strain relationships for the concrete and steel. If the stress developing in the concrete or steel

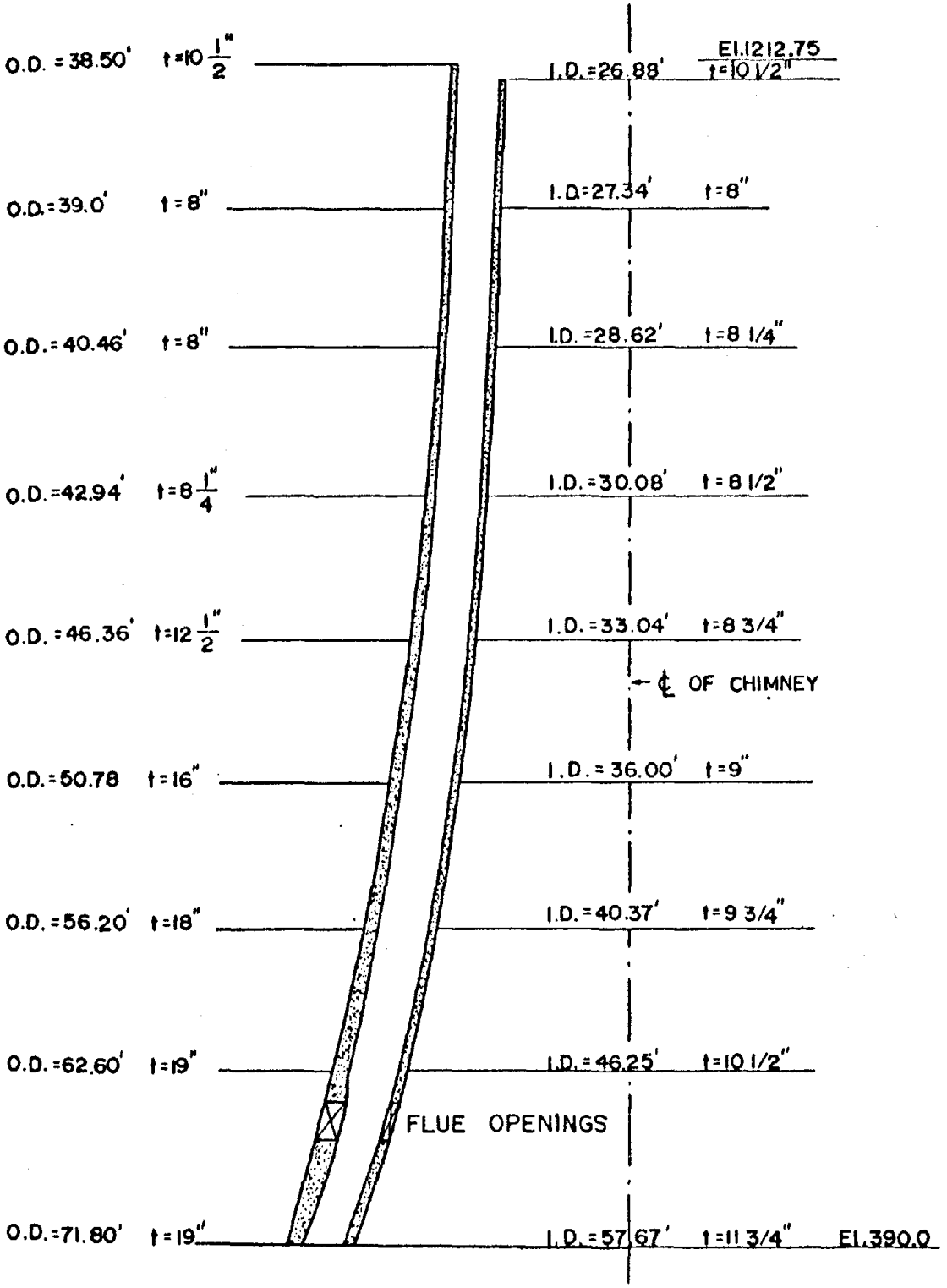

Figure 2.1 Description of the chimney.

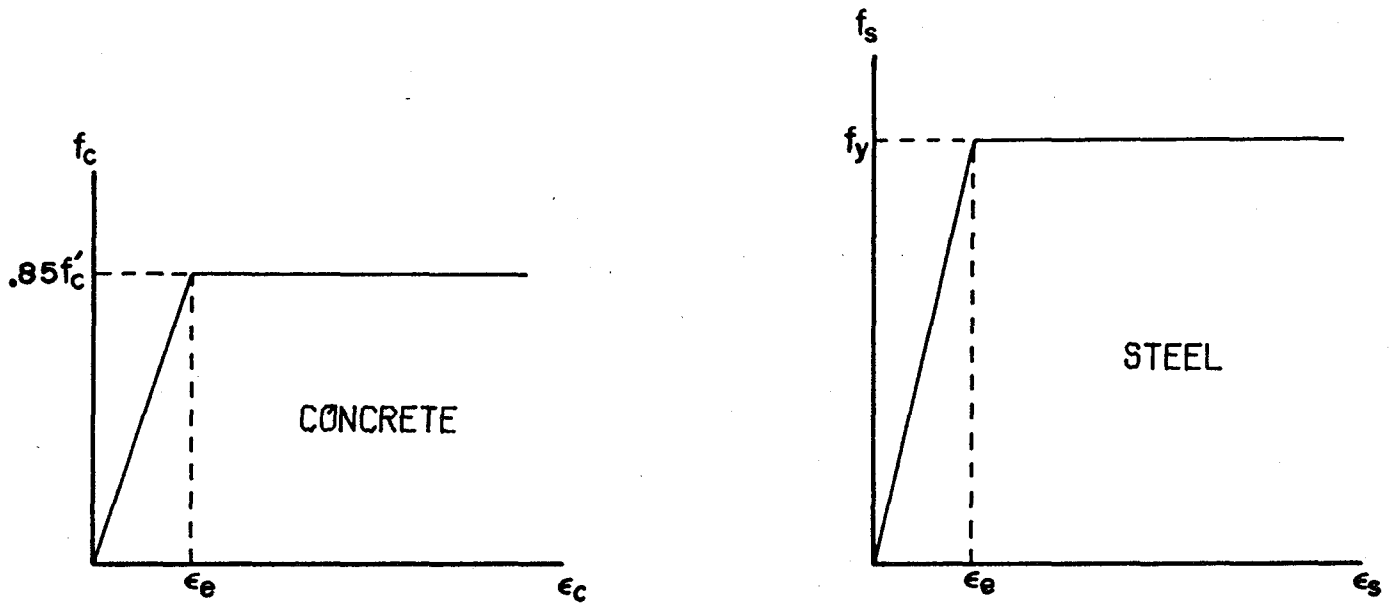

Figure 2.2 Idealized stress-strain relationship for concrete and steel

is beyond the elastic limit as shown in the above figures, the material is assumed to be in the plastic range and cannot take any additional stress.

The Modeling

The 823 foot tall chimney is modeled by 8 pipe-type beam finite elements as shown in Figure 2.3. Various geometric quantities for each element of both shells are tabulated in Table I.

For the case with flue openings, the first element in Figure 2.3 is modified to an equivalent homogeneous beam finite element. This is done by first modeling the element by 70 quadrilateral plate finite elements and then finding the static equivalent axial area and moments of inertia for the equivalent beam element. The results for equivalent thickness are also shown in Table I.

Figure 2.4 shows the model for local stress analysis around the flue openings. The modeling is obtained by modifying the first beam finite element into 244 quadrilateral plate finite elements.

For calculating the section area of beam elements or plate elements, the reinforcing steel area of that section is transformed into equivalent concrete area, thus making the section homogeneous.

Table I. Geometric Quantities for the Chimney

Element Number	Outer Shell			
	ℓ(in)*	D(in)*	t(in)*	m/unitℓ *
1 (no holes)	1440	783.0	23.81	13.104
1 (with holes)	1440	783.0	20.50	11.280
2	1200	694.3	19.17	9.331
3	1200	624.9	17.88	7.842
4	1200	568.6	15.17	6.048
5	1200	525.7	10.92	3.999
6	1200	492.3	8.73	2.985
7	1200	468.8	8.36	2.721
8	1233	455.8	9.40	2.983
Element Number	Inner Shell			
	ℓ(in)	D(in)	t(in)	m/unitℓ
1 (no holes)	1440	637.2	13.93	6.053
1 (with holes)	1440	637.2	11.94	5.188
2	1200	529.9	10.30	3.725
3	1200	467.6	9.54	3.044
4	1200	423.1	9.04	2.608
5	1200	387.4	8.86	2.340
6	1200	360.6	8.67	2.133
7	1200	343.9	8.35	1.958
8	1104	334.6	9.39	2.144

* = length of the element (inch)
D = diameter of the element (inch)
t = thickness of the element (inch)
m = mass of the element (slug)

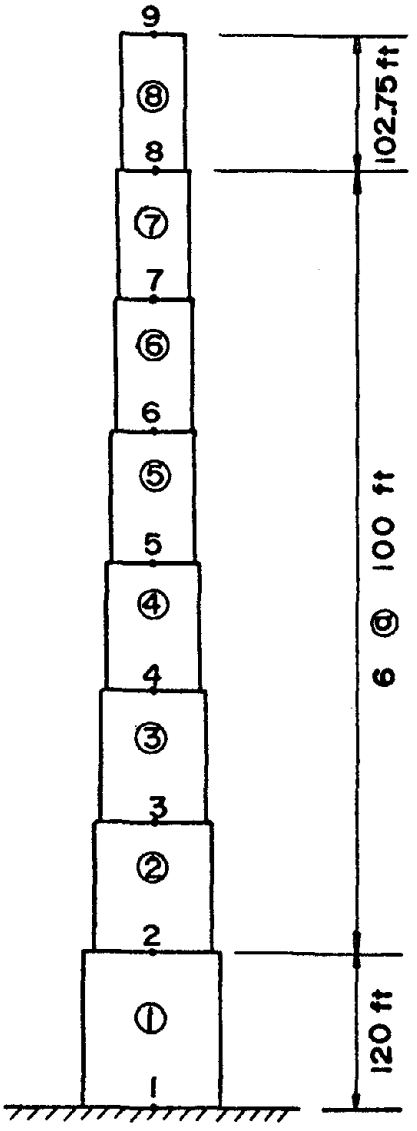

Figure 2.3 Eight-element modeling of the chimney

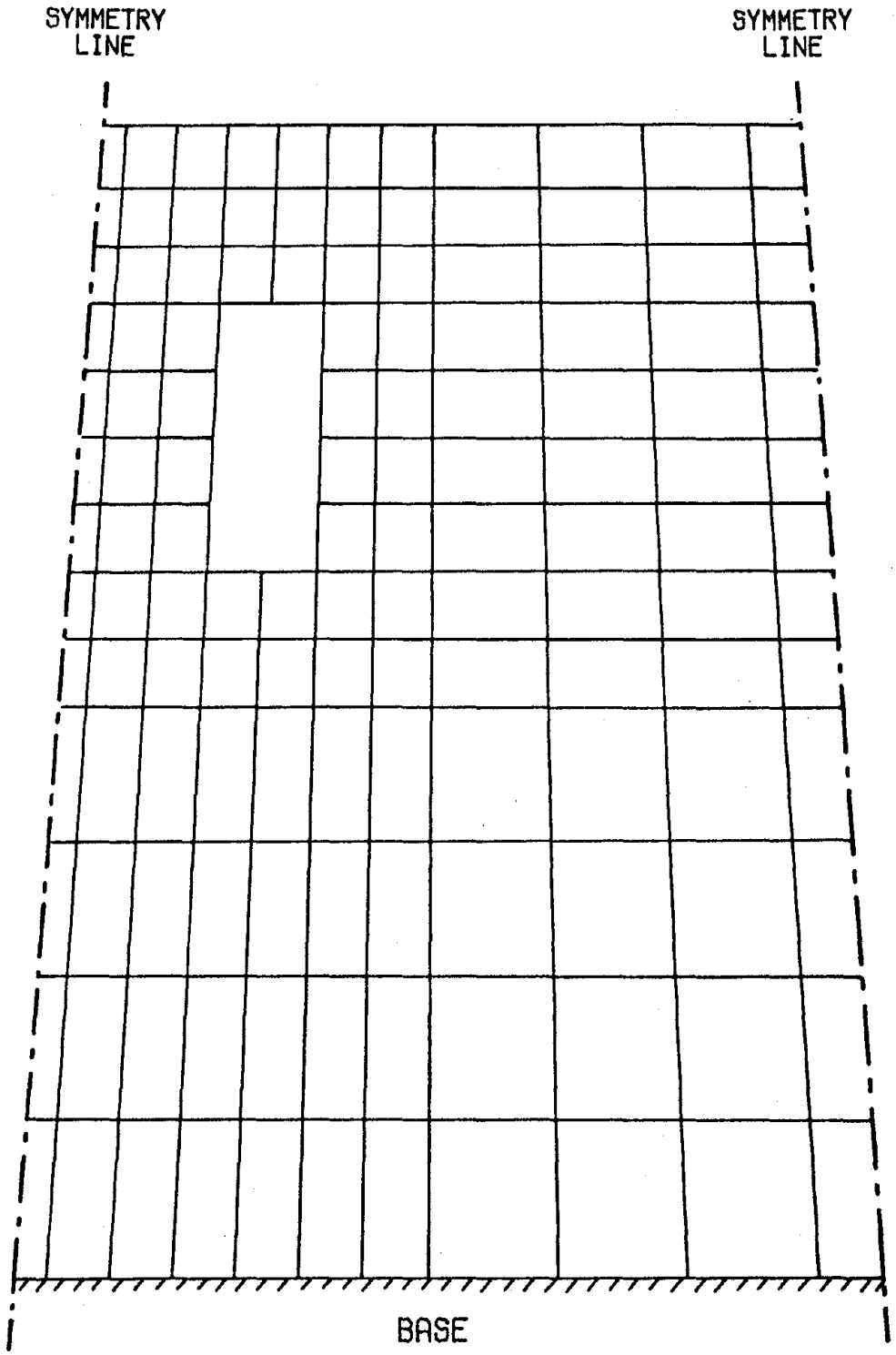

Figure 2.4 Plate element modeling of the first beam element for stress concentration analysis around flue openings.

III. Finite Elements and Formulations

As mentioned in the preceding section, two types of finite elements are used in the analysis. The major element used for both elastic and inelastic analyses is the beam finite element. This element is discussed in more detail in this section.

1. The Beam Finite Element

A typical beam finite element with two displacements and two rotational degrees of freedom at each nodal point is shown in Figure 3.1.

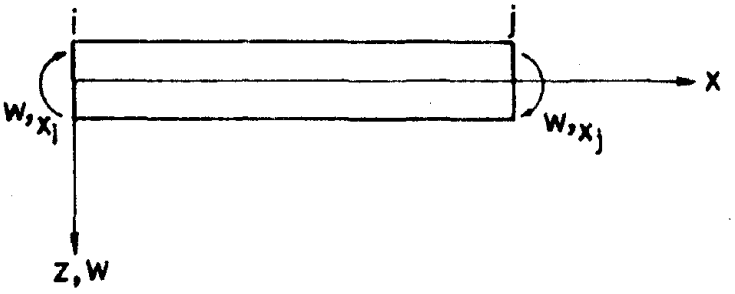

Figure 3.1 Typical beam finite element.

The displacement function in the z-direction is assumed to be in the form of a cubic polynomial function

$$w(x) = a_1 + a_2x + a_3x^2 + a_4x^3 \tag{3.1}$$

where w is the displacement in the z-direction, x is the coordinate axis defined in Figure 3.1 and the a's are the coefficients to be found. This equation satisfies all the completeness and compatibility requirements because it includes all rigid body motion and constant strain state. Substituting the nodal coordinates and displacements into Equation (3.1), it can be expressed in terms of the generalized nodal displacements as

$$w(x) = (1 - \frac{3x^2}{\ell^2} + \frac{2x^3}{\ell^3})w_i + (x - \frac{2x^2}{\ell} + \frac{x^3}{\ell^2})w_{,x_i} + (\frac{3x^2}{\ell^2} - \frac{3x^3}{\ell^3})w_j + (\frac{x^3}{\ell^2} - \frac{x^2}{\ell})w_{,x_j} \quad (3.2)$$

where w_i and w_j are the displacements at nodal points i and j respectively and $w_{,x_i}$, $w_{,x_j}$ are the rotations at nodal points i and j as shown in Figure 3.1.

From the beam theory, the total strain at any point within the beam element is defined as

$$\varepsilon = -z \frac{d^2w}{dx^2} \quad (3.3)$$

Substituting Equation (3.2) into (3.3), we have

$$\{\varepsilon\} = [B]\{\delta\} \quad (3.4)$$

where $\{\varepsilon\}$ is the vector of total strain, $\{\delta\}$ is the vector of generalized nodal displacements and [B] is a functional matrix which depends on the assumptions of the shape function of the element.

The strain energy of the element is obtained by integrating the internal work done by the various stresses over the volumn of the element

$$U = 1/2 \int_v \sigma \varepsilon dv = 1/2 \int_v \varepsilon E \varepsilon \, dv \quad (3.5)$$

where E is the elastic modulus and σ is the stress of the element.

Expressing the above equation in terms of generalized nodal displacements, we have

$$U = 1/2 \{\delta\}^T \iiint_v [B]^T[E][B]dv \{\delta\} \quad (3.6)$$

Application of Castigliano's theorem to Equation (3.6) yields

$$\{F\} = \iiint_V [B]^T[E][B]dv \{\delta\} \tag{3.7}$$

where {F} is the vector of generalized nodal forces. Thus the stiffness matrix of the element is obtained as

$$[K] = \iiint_V [B]^T[E][B]dv \tag{3.8}$$

Equations (3.1) to (3.7) are used for elastic analysis. The inelastic formulation will be discussed in section V.

2. The Plate Finite Element

For the local analysis of the chimney, a three dimensional quadrilateral plate finite element is used. The element is composed of four triangular elements with the four common vertices meeting near the centroid of the quadrilateral. The degrees of freedom at this central nodal point are eliminated at the element level prior to the assemblage.

The membrane stiffness of each sub-triangular element is based on the constant strain assumption with linear inplane displacement functions (6). The bending stiffness of each sub-triangular element is represented by the fully compatible HCT element based on the lateral deflection function that varies cubically with the inplane coordinates (7).

IV. Elastic Response of a Chimney to Earthquake

4.1 Time History Analysis of a Chimney

A. Structural Equations of Motion

The equations of motion for a structure subjected to ground acceleration can be written in the following form:

$$[m]\{\ddot{y}\} + [c]\{\dot{y}\} + [K]\{y\} = -[m]\{\ddot{y}_g\} \tag{4.1}$$

where $\{y\}$, $\{\dot{y}\}$ and $\{\ddot{y}\}$ are, respectively, the displacement, the velocity and the acceleration vector of the body motion and $\{\ddot{y}_g\}$ is the ground motion acceleration vector. If the mass of the system is assumed to be concentrated at each nodal point, the mass matrix in Equation (4.1) can be easily formed as a diagonal lumped mass matrix. The elastic stiffness matrix [K] in Equation (4.1) is obtained from Equation (3.8) and the viscous damping matrix [c] is usually expressed by a simplified approximation as the following:

$$[c] = \alpha[m] + \beta[K] \tag{4.2}$$

where

$$\alpha + \beta\omega_n^2 = 2\xi\omega_n \tag{4.3}$$

ξ is the ratio of actual damping to critical damping and ω_n is the natural frequency in the nth mode. By knowing ξ for the system, it is possible to select the constants α and β to define the damping matrix [c]. The fundamental mode, being a predominant mode, is adopted along with the second mode to evaluate the values of α and β.

Equation (4.1) could be solved by a numerical integration method such as the step-by-step integration method. However, in analyzing the earthquake response of a linear structure, it is more efficient to use

the "mode superposition method" because the ground motion tends to excite strongly the lowest modes of vibration only.

B. Mode Superposition Method

The displacement vector {y} of the cantilever beam such as the chimney can be developed by superimposing suitable amplitudes of the natural modes of the beam

$$\{y\} = [\phi]\{Y\} \tag{4.4}$$

where the column vector $\{\phi_i\}$ is the mode shape of ith mode and Y_i is the generalized coordinate of ith mode. Substituting the above equation into Equation (4.1) and premultiplying it by the transpose of the nth mode shape vector $\{\phi\}_n^T$, it becomes

$$\{\phi\}_n^T[m][\phi]\{\ddot{Y}\} + \{\phi\}_n^T[c][\phi]\{\dot{Y}\} + \{\phi\}_n^T[K][\phi]\{Y\} = -\{\phi\}_n^T[m]\{\ddot{y}_g\}$$

By using the orthogonality property of the mode shape vector, the above equation is reduced to a single degree of freedom equation of motion for mode n

$$\bar{M}_n\ddot{Y}_n + \bar{c}_n Y_n + \bar{K}_n\dot{Y}_n = -\bar{F}_n\{\ddot{y}_g\} \tag{4.5}$$

or

$$\ddot{Y}_n + 2\xi_n\omega_n\dot{Y}_n + \omega_n^2 Y_n = -\bar{F}_n/\bar{M}_n \tag{4.6}$$

where

$$\bar{M}_n = \{\phi\}_n^T[m]\{\phi\}_n \quad , \quad F_n = \{\phi\}_n^T[m]$$

$$\bar{c}_n = \{\phi\}_n^T[c]\{\phi\}_n \quad , \quad \omega_n^2 = \bar{K}_n/\bar{M}_n$$

$$\bar{K}_n = \{\phi\}_n^T[K]\{\phi\}_n \quad , \quad \xi_n = \bar{C}_n/2\bar{M}_n\omega_n$$

The solution of the equation (4.6) can be easily obtained by using Duhamel's integral

$$Y_n(t) = \frac{\bar{F}_n}{\bar{M}_n \omega_n} \int_0^t \ddot{y}_g(\tau) e^{-\xi_n \omega_n (t-\tau)} \sin \omega_n (t-\tau) d\tau \qquad (4.7)$$

Therefore, the displacements expressed in geometric coordinates are given by Equation (4.4) and the elastic forces are given by

$$\{F\} = [K]\{y\} \qquad \text{at time } t$$

C. Results and Discussion

(1) Undamped free vibration (without crack)

The equations of motion for the undamped free vibration of a structure can be obtained by omitting the damping matrix and the applied force vector from Equation (4.1) or

$$[m]\{\ddot{y}\} + [K]\{y\} = \{0\}$$

The motion of a free vibration is assumed to be a homonic motion with natural frequency ω. Therefore, the above equation can be reduced to a determinant as

$$|[K] - \omega^2[m]| = 0$$

The solution of this equation yields the natural frequencies of the structure.

The first 12 natural frequencies and periods are tabulated in Table II for the outer shell and in Table III for the inner shell. It is seen in both tables that the flue openings have very little effect on the values of frequencies. In reality, the chimney does have the flue openings, therefore, in the following analyses, only the chimney with flue openings is considered. The 5^{th}, 8^{th}, and 11^{th} modes of the outer shell as shown in Table II with * marks are longitudinal modes and the others are flexural modes. For the inner shell, the longitudinal modes appear at 5^{th}, 9^{th}, and 11^{th} modes.

Table II. The Natural Frequencies and Periods for the Outer Shell With or Without Flue Openings.

Mode Number	Without Opening		With Opening	
	Frequency (rad./sec.)	Period (Seconds)	Frequency (rad./sec.)	Period (Seconds)
1	2.003	3.1371	1.969	3.1911
2	7.149	0.8789	7.009	0.8965
3	16.775	0.3746	16.573	0.3791
4	29.184	0.2153	29.015	0.2166
5*	31.846	0.1973	31.387	0.2002
6	43.475	0.1445	43.430	0.1447
7	58.063	0.1082	58.119	0.1081
8*	66.298	0.0948	65.275	0.0963
9	71.364	0.0881	71.436	0.0880
10	81.740	0.0769	81.811	0.0768
11*	109.990	0.0571	109.300	0.0575
12	145.550	0.0432	145.750	0.0431

* Longitudinal modes

Table III. The Natural Frequencies and Periods for the Inner Shell With or Without Flue Openings.

Mode Number	Without Opening		With Opening	
	Frequency (rad./sec.)	Period (Seconds)	Frequency (rad./sec.)	Period (Seconds)
1	1.296	4.8491	1.277	4.9223
2	5.719	1.0987	5.615	1.1190
3	13.766	0.4564	13.572	0.4629
4	24.477	0.2567	24.319	0.2584
5*	28.407	0.2212	28.034	0.2241
6	36.987	0.1699	36.975	0.1699
7	50.161	0.1253	50.252	0.1250
8	61.890	0.1015	61.980	0.1014
9*	71.445	0.0879	70.369	0.0893
10	72.901	0.0862	72.996	0.0861
11*	111.660	0.0563	110.860	0.0567
12	148.600	0.0423	148.850	0.0422

* Longitudinal modes

The first six flexural mode shapes of the outer shell are plotted in Figures 4.1 and 4.2.

(2) Response to the horizontal component of an earthquake (without crack)

The record of El Centro earthquake which occurred on May 18, 1940 is selected to analyze the time history dynamic response of the chimney. Due to the relatively long duration of intense motion of this earthquake, the first 30 seconds of the acceleration record as shown in Figure 4.3 is used for response analysis. The record in Figure 4.3 shows that the acceleration oscillates at a frequency of approximately 3 to 7 cycles per second. The results in Tables II and III for natural frequencies show that the seventh frequency (sixth flexural frequency) is approximately 9.25 Hertz for the outer shell and 8 Hertz for the inner shell, respectively. Only the first six flexural modes are used in the mode superposition to simulate the dynamic response of the chimney to the horizontal component of this earthquake.

The time history responses for the deflections at the tip of the outer shell and at the tip of the inner shell are shown in Figures 4.4 and 4.5, respectively. The maximum tip deflection is 42.6 inches at 28.3 seconds for the outer shell and 27.1 inches at 29.3 seconds for the inner shell. The late arrival of the maximum tip deflections shows that 30 seconds of ground motion is needed for the dynamic response analysis of the chimney although the accelerations are large only in the first 12 seconds of the ground motion. It also shows that the occurrence of an even larger tip defleciton of the two shells at some time after 30 seconds is possible although the magnitude of acceleration becomes considerably smaller after that time.

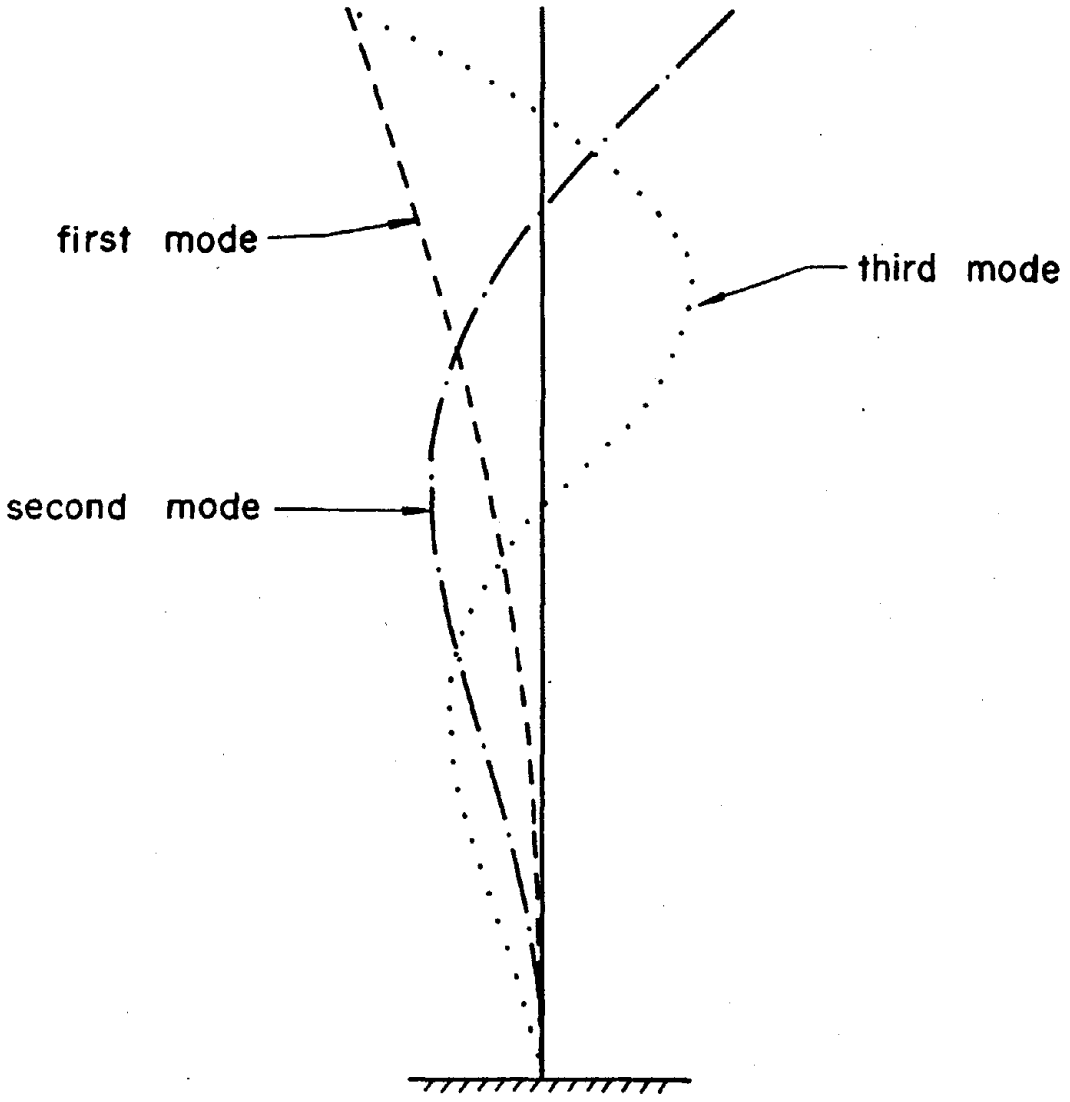

Figure 4.1 First, second, and third mode shapes for the outer shell.

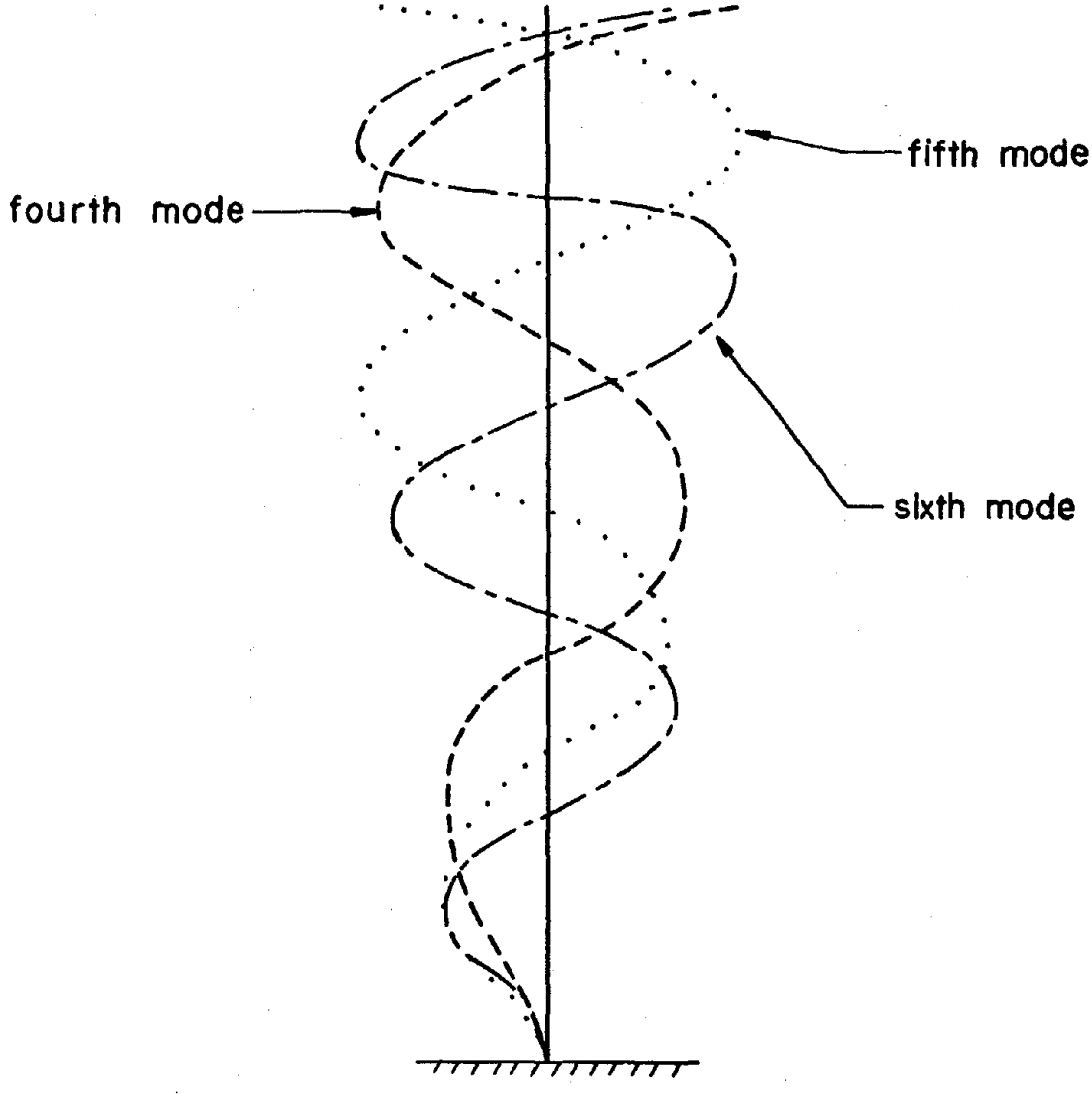

Figure 4.2 Fourth, fifth, and sixth mode shapes for the outer shell.

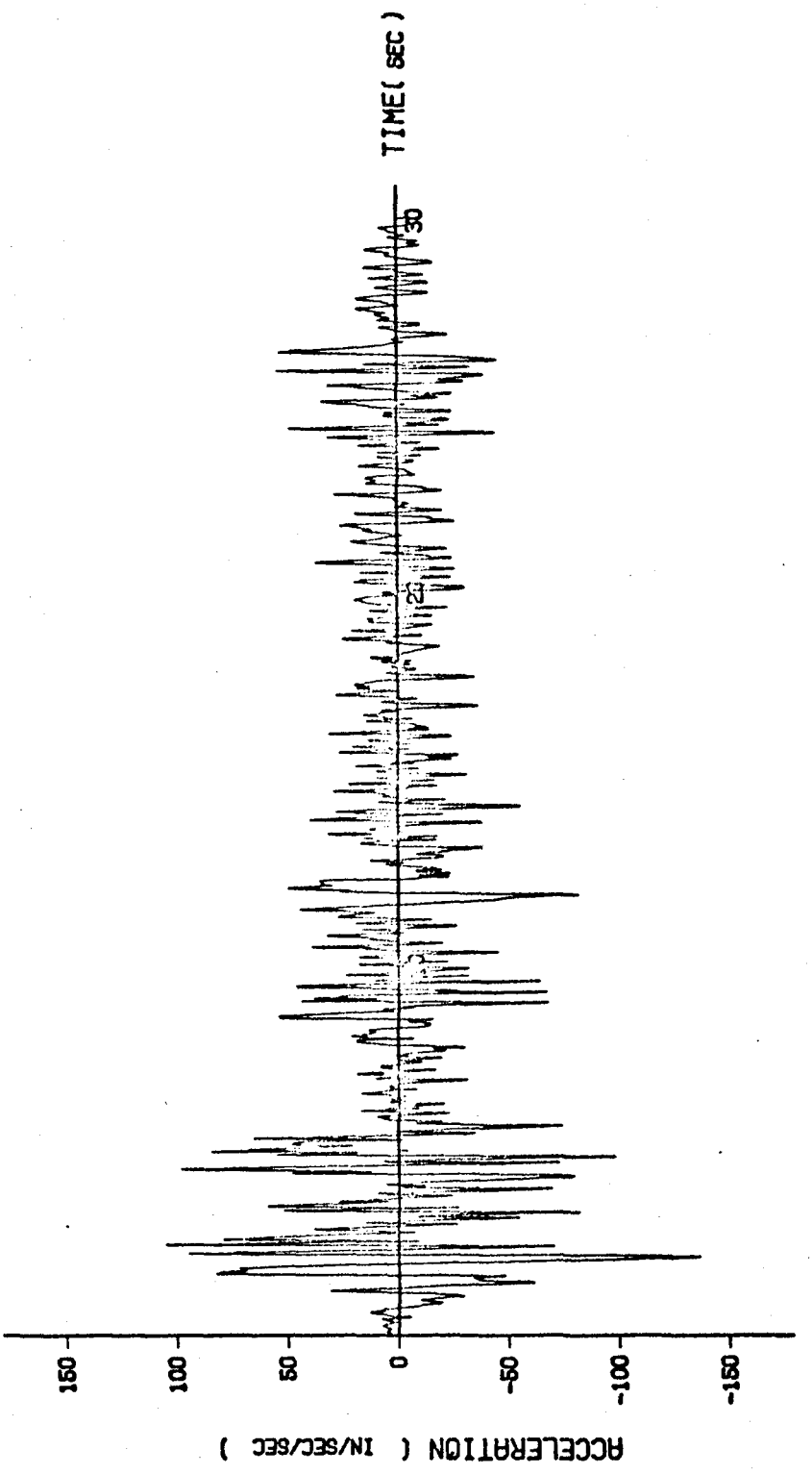

Figure 4.3 Ground acceleration, El Centro earthquake of May 18, 1940, N-S component.

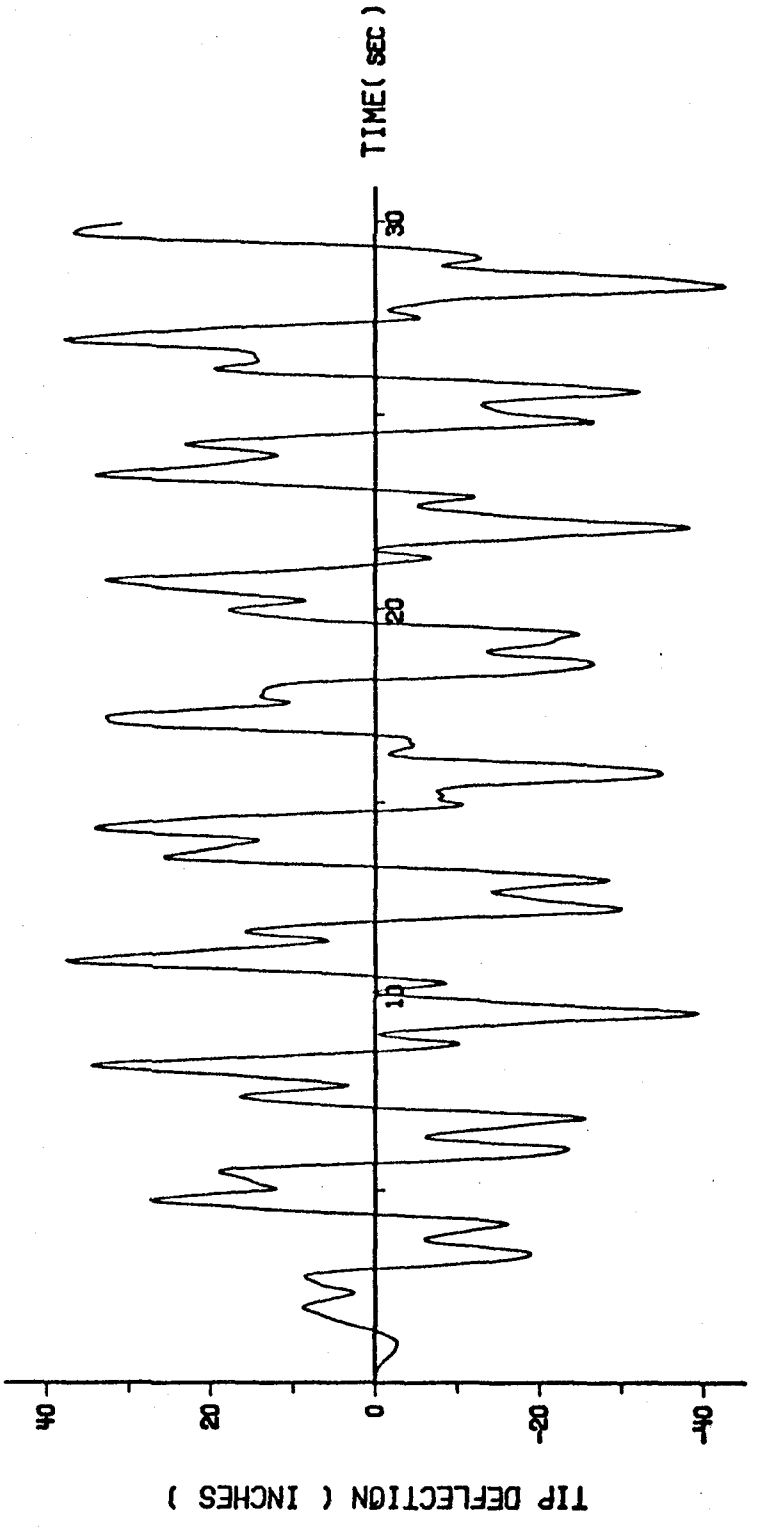

Figure 4.4 Time history response for the tip deflection of outer shell.

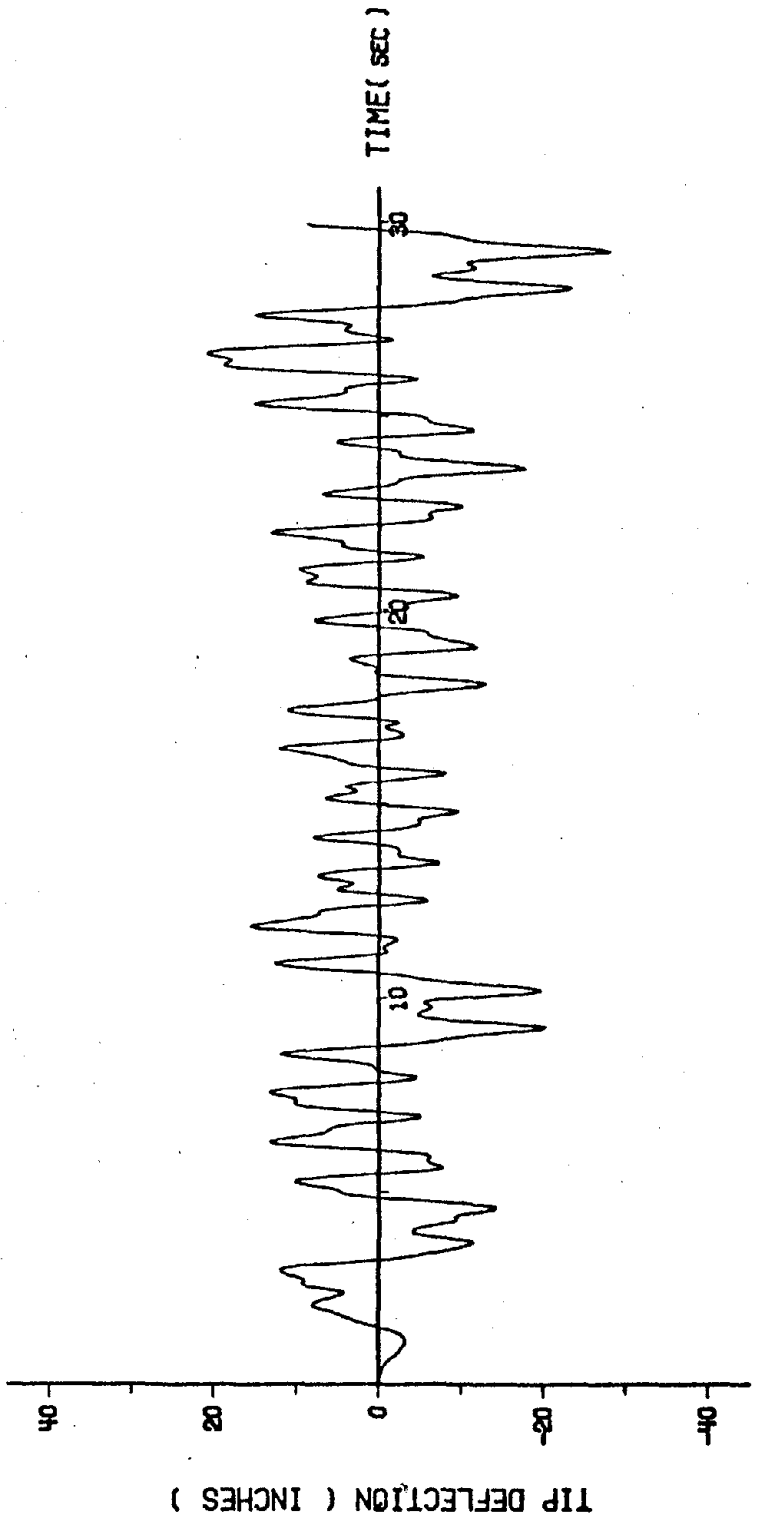

Figure 4.5 Time history response for the tip deflection of inner shell.

When both shells of the chimney are subjected to the earthquake simultaneously, the air spacings between these two shells change with time. Figure 4.6 shows the time history curve of the net spacing between the tops of the outer and inner shells. The horizontal dashed line in this figure is the original designed air space between the tips of the two shells. Figure 4.6 shows that the tip spacings are greater than zero at any moment, that is, the two shells do not collide during the entire 30 seconds history of the earthquake.

The time history responses for the base bending moment and base shearing force of the outer shell are shown in Figures 4.7 and 4.8, respectively. The maximum bending moment occurs at the time of 25.2 seconds with a magnitude of 32.05×10^6 in-kips and the maximum shearing force occurs at the time of 22.5 seconds with a magnitude of 11.96×10^3 kips. Figures 4.9 and 4.10 show the time history responses for the base bending moment and base shearing force of the inner shell, respectively. The values shown in these two figures are quite small if compared to the values of the outer shell. Figure 4.11 shows the maximum bending moments and the maximum shearing forces distributed along the height of the outer and inner shells. Although these values may not occur at the same time they are the maximum absolute values occurring at each nodal point during the entire course of the earthquake. The corresponding maximum bending stresses and shearing stresses in the steel and concrete for the two shells are shown in Figures 4.12 and 4.13. Although the maximum bending moment occurs at the base of the chimney, the maximum bending stress may not occur at this point because the cross section of the chimney is not uniform along its length. In fact, the most critical sections are at an elevation of 910 feet for the outer shell with a maximum bending stress of 4233 psi in

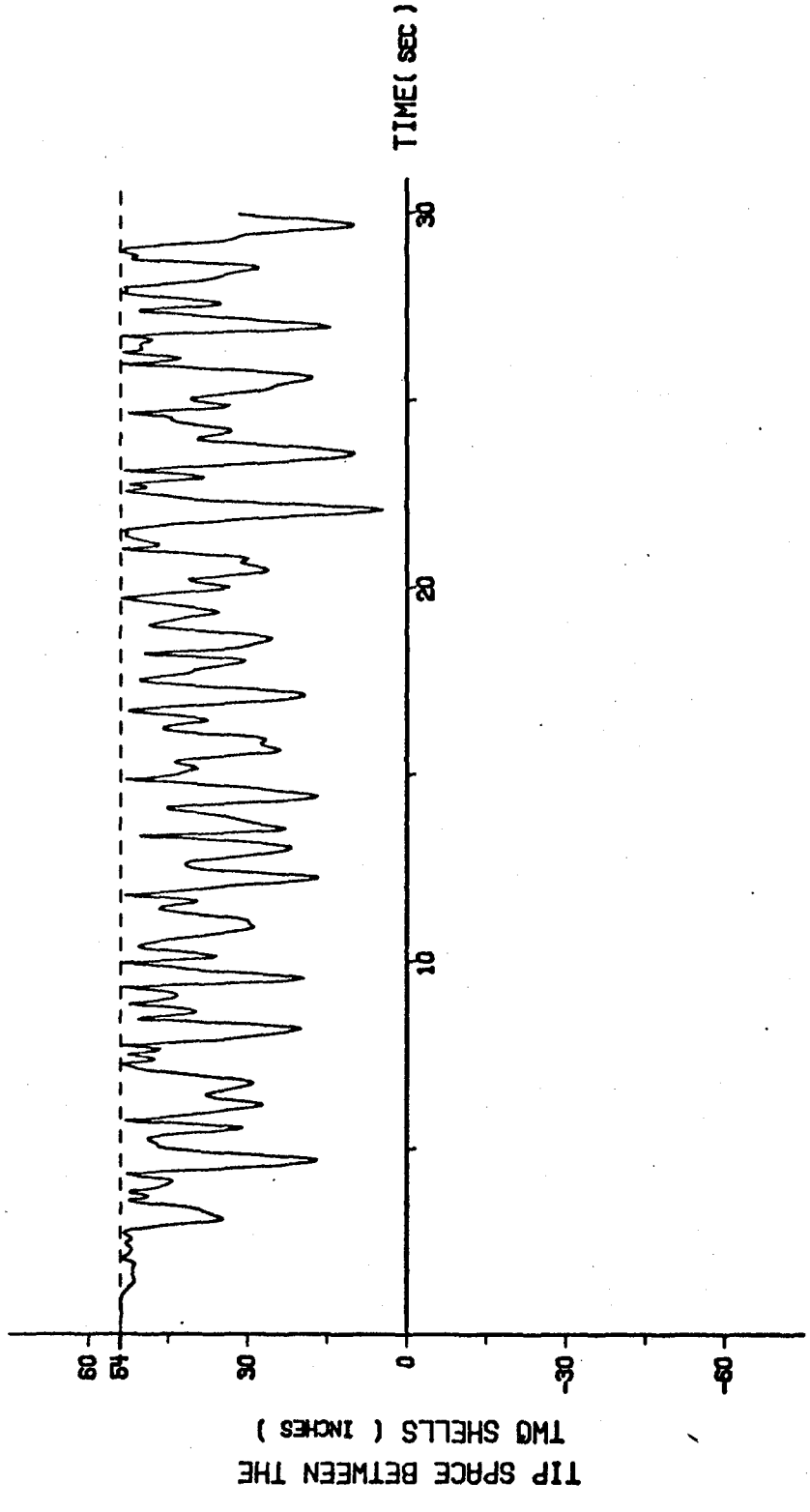

Figure 4.6 Time history curve for the spacing between tops of outer and inner shell.

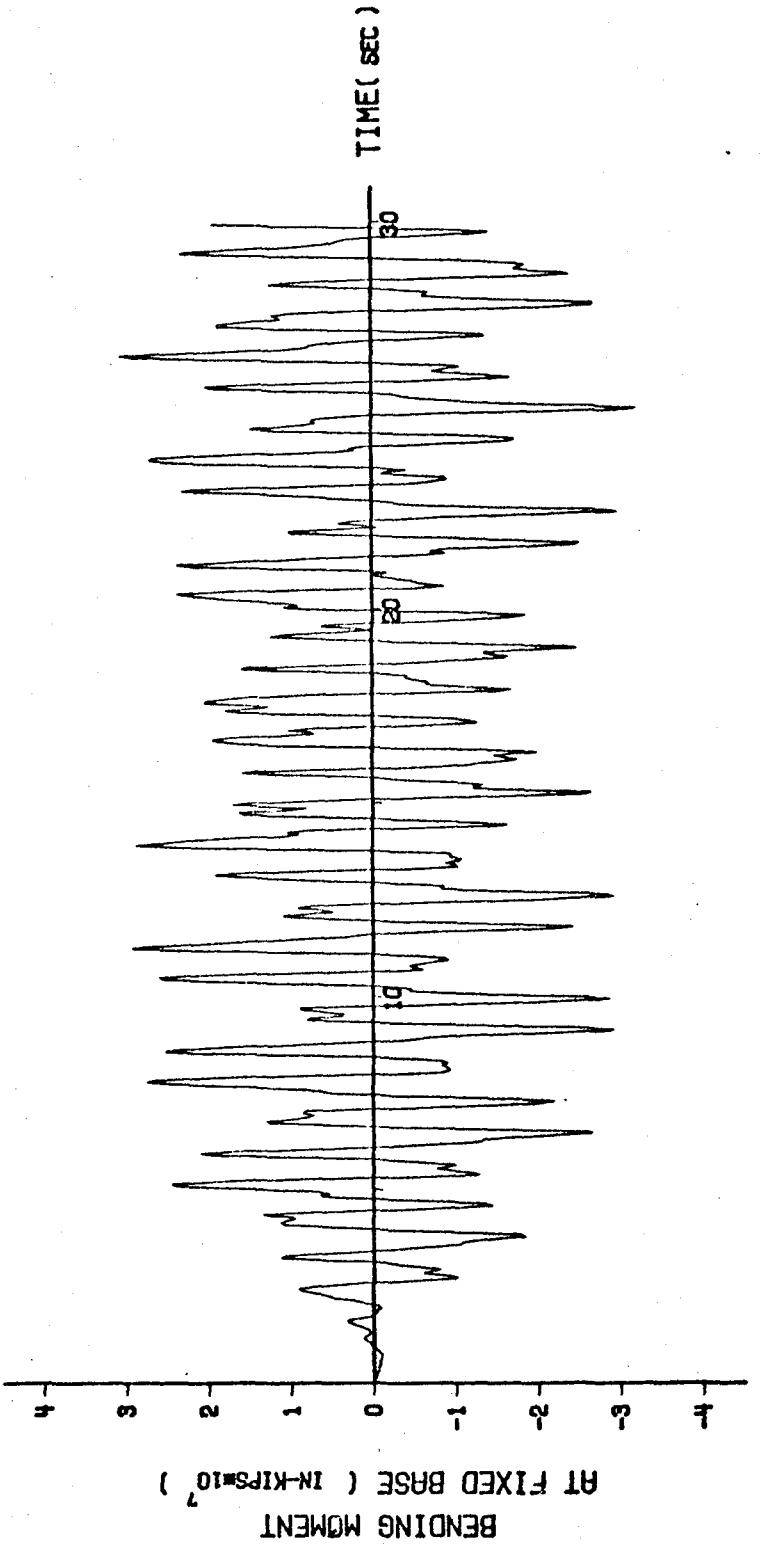

Figure 4.7 Time history response for the base bending moment of outer shell.

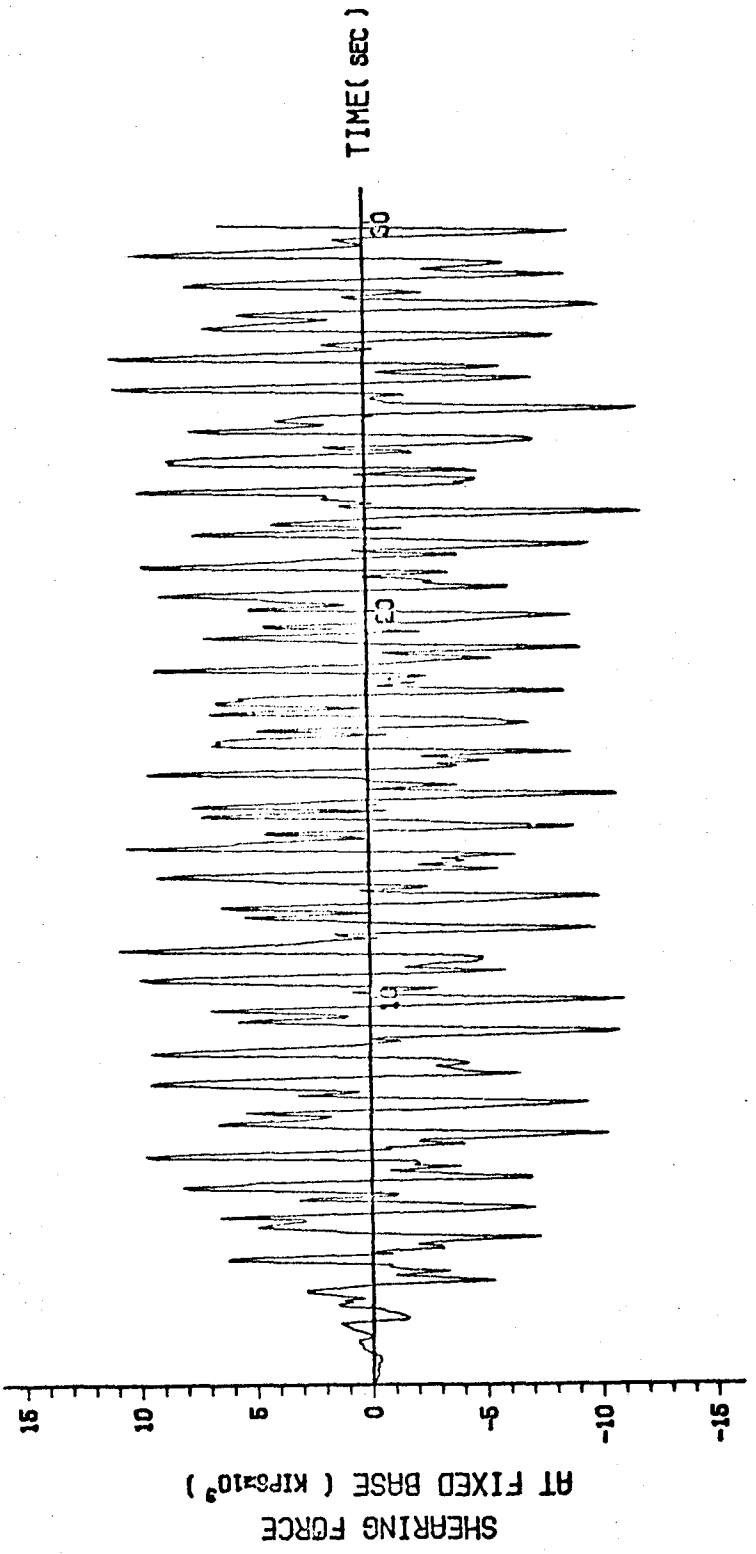

Figure 4.8 Time history response for the base shearing force of outer shell.

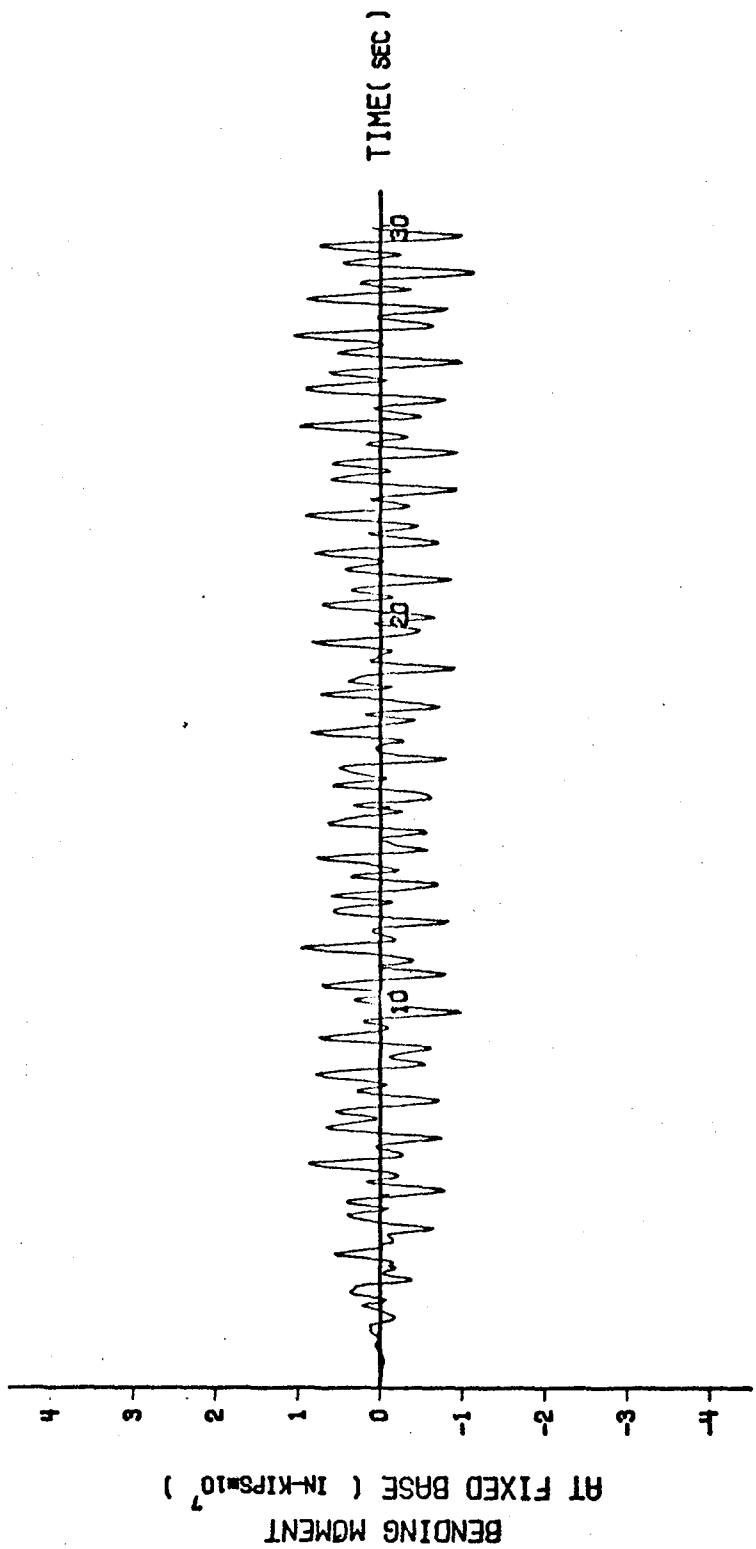

Figure 4.9 Time history response for the base bending moment of inner shell.

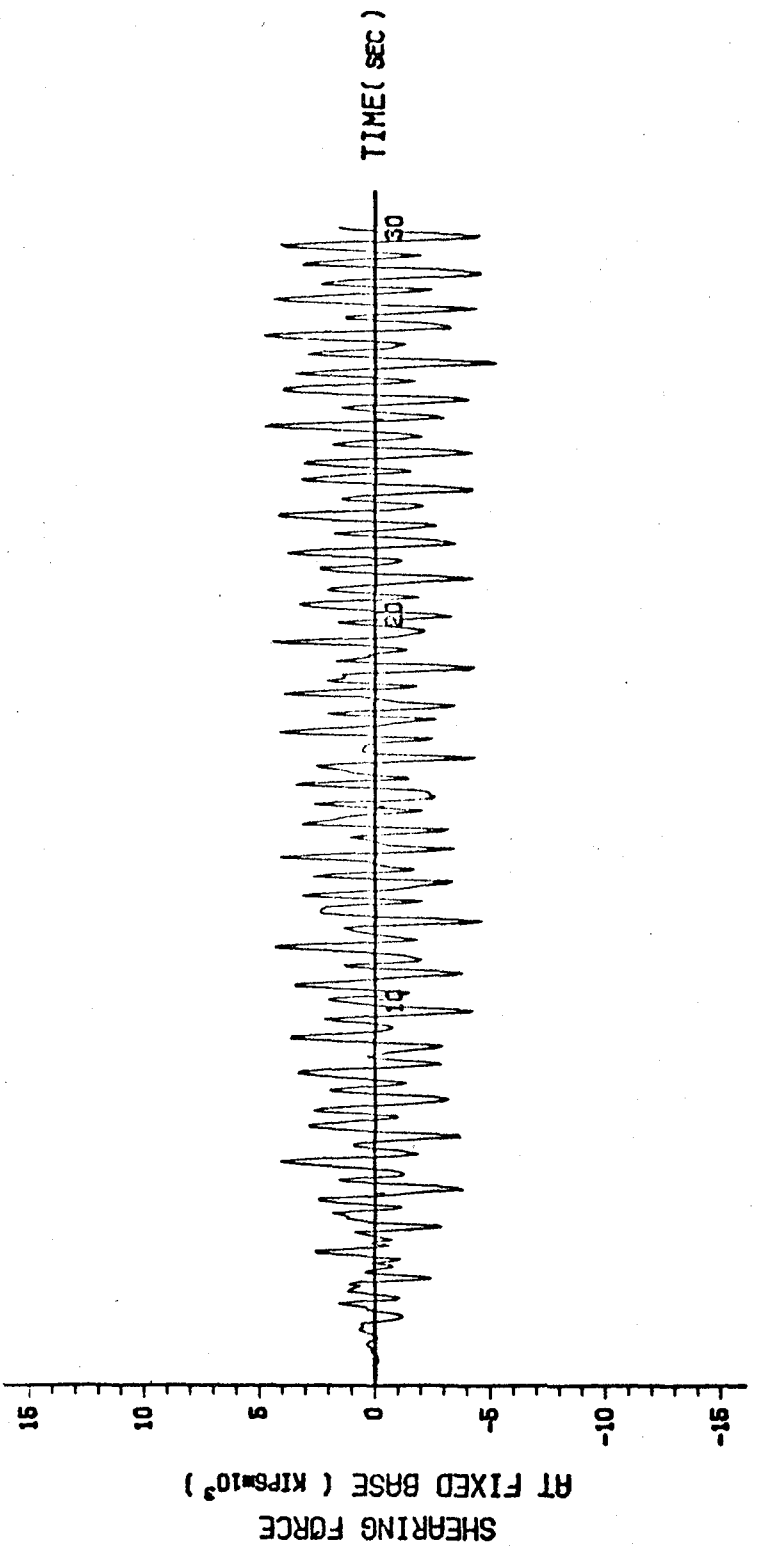

Figure 4.10 Time history response for the base shearing force of inner shell.

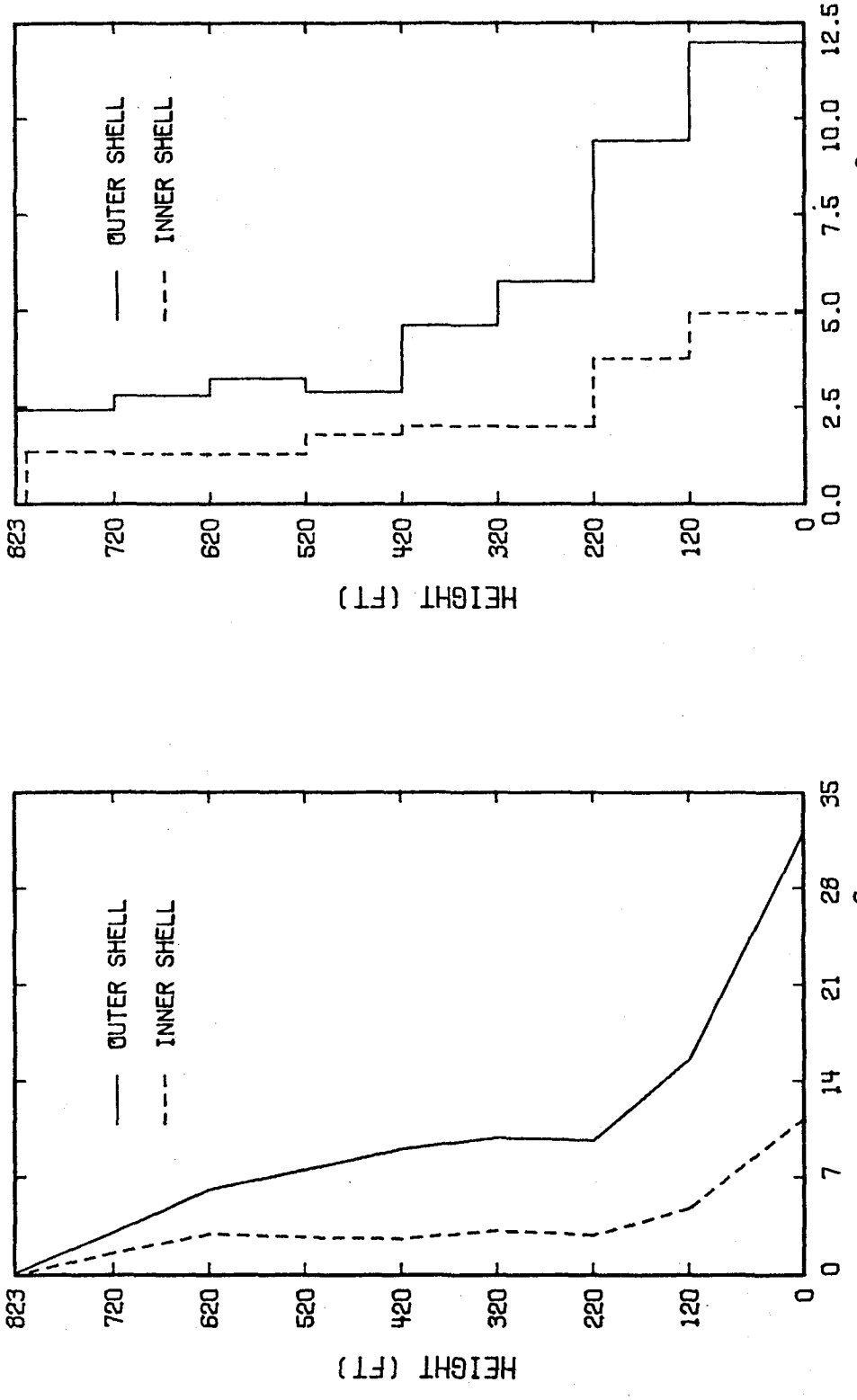

Figure 4.11 Maximum bending moment and maximum shearing force versus height for both shells.

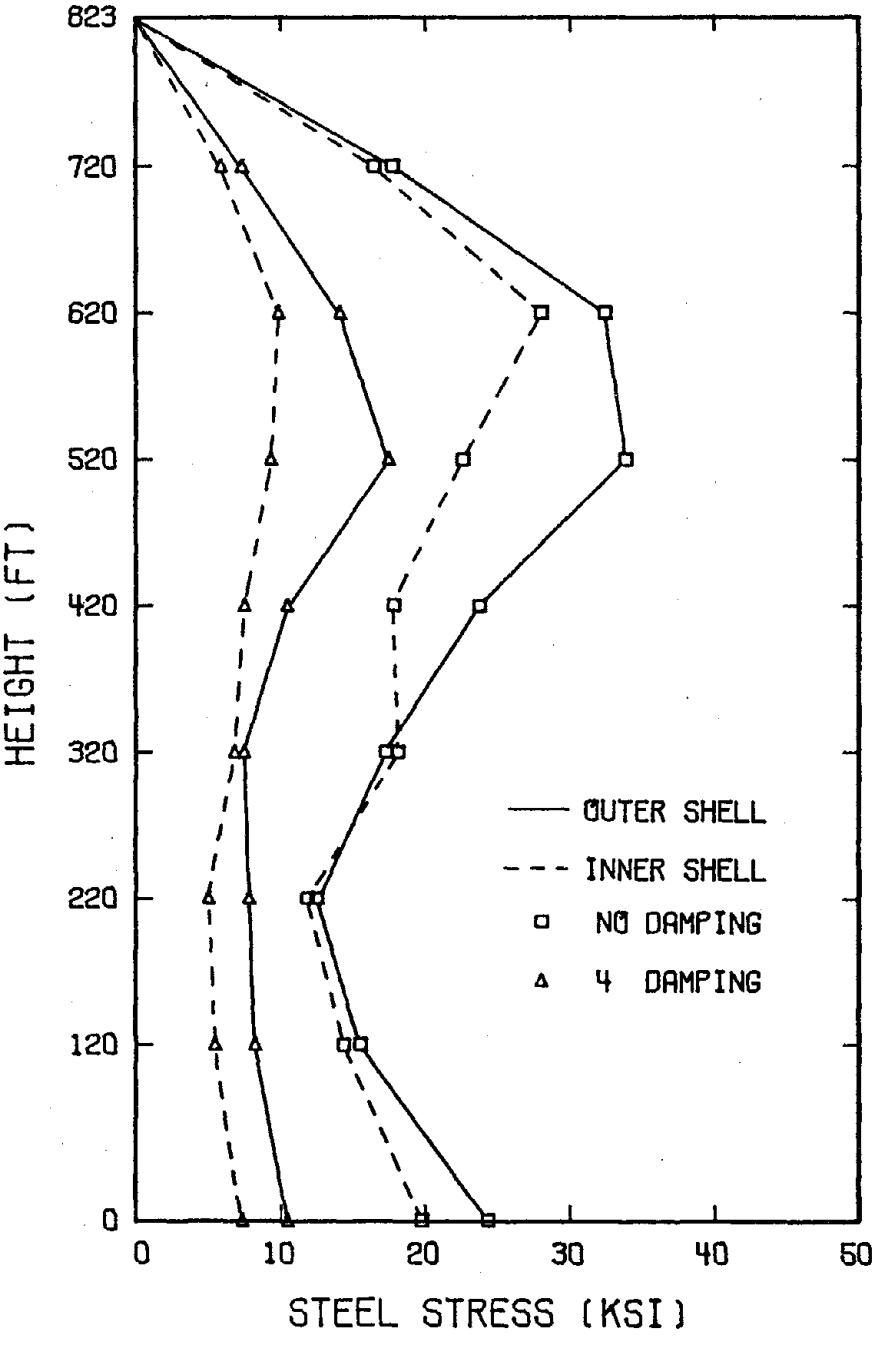

Figure 4.12 Steel stress curves for both shells with no damping and with 4% critical damping.

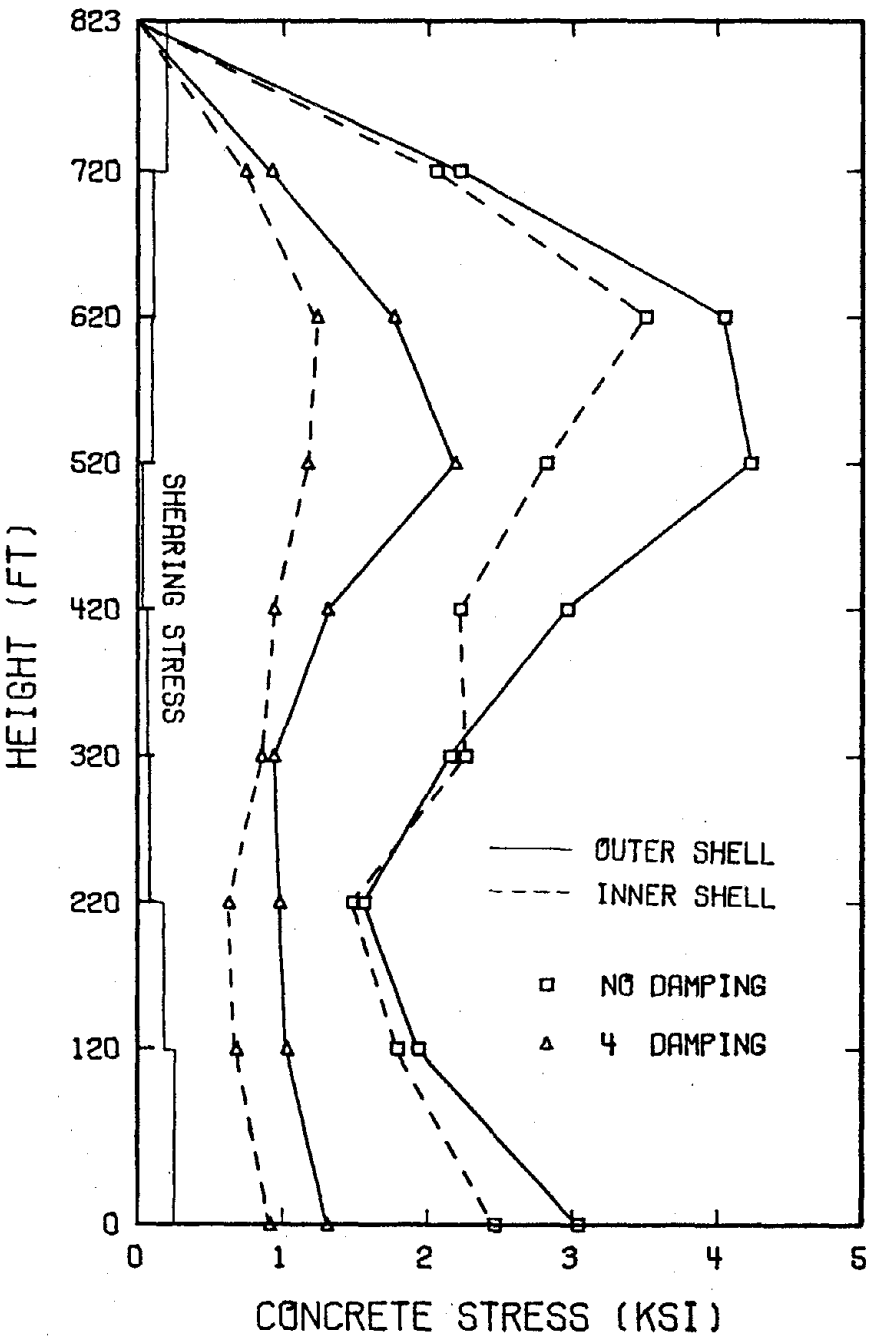

Figure 4.13 Concrete stress curves for both shells with no damping and with 4% critical damping.

the concrete and at an elevation of 1010 feet for the inner shell with a maximum bending stress of 3502 psi in the concrete. In Figure 4.13, the shearing stresses distributed in the concrete for both shells seem greater than the maximum allowable shearing stress of the concrete, 132 psi. However, besides the vertical reinforcements there is certain amount of horizontal reinforcements in the chimney which can also take the shearing force. It appears reasonable to assume that the shearing stresses are within safe limits.

(3) Damping effect on responses (without crack)

The effect of viscous damping is considered in this study. It is assumed that each of the six flexural modes has the same damping coefficient. Six different values of viscous damping coefficient are assumed: 0.5%, 1%, 2%, 4%, 7%, and 10% of its critical value. The effect of damping on the tip deflection, base bending moment, and base shearing force for both shells is studied and summarized by the plots shown in Figures 4.14, 4.15, and 4.16, respectively. It is seen that at 4 percent of critical damping, the tip deflection, base bending moment, and base shearing force all decrease by more than 50 percent of their original undamped values. The further increase in damping coefficient does not seem to decrease the three physical quantities as much.

In practical design, the viscous damping of such concrete structure is assumed to be about 4% of its critical value. Hence, all the bending stresses and shearing stresses developed in the chimney are expected to reduce by about 50 percent as shown in Figures 4.12 and 4.13. In such a situation, the material behavior of the chimney will not go into the plastic range during the history of the earthquake.

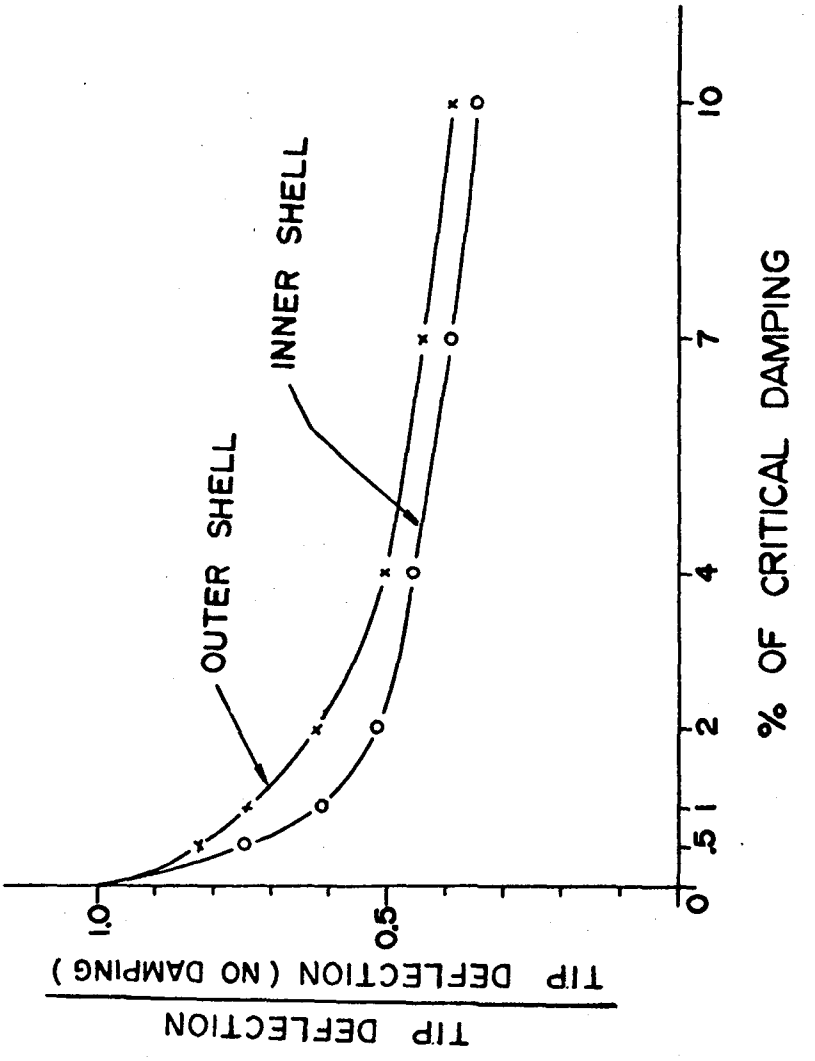

Figure 4.14 Variation of tip deflection with damping for both shells

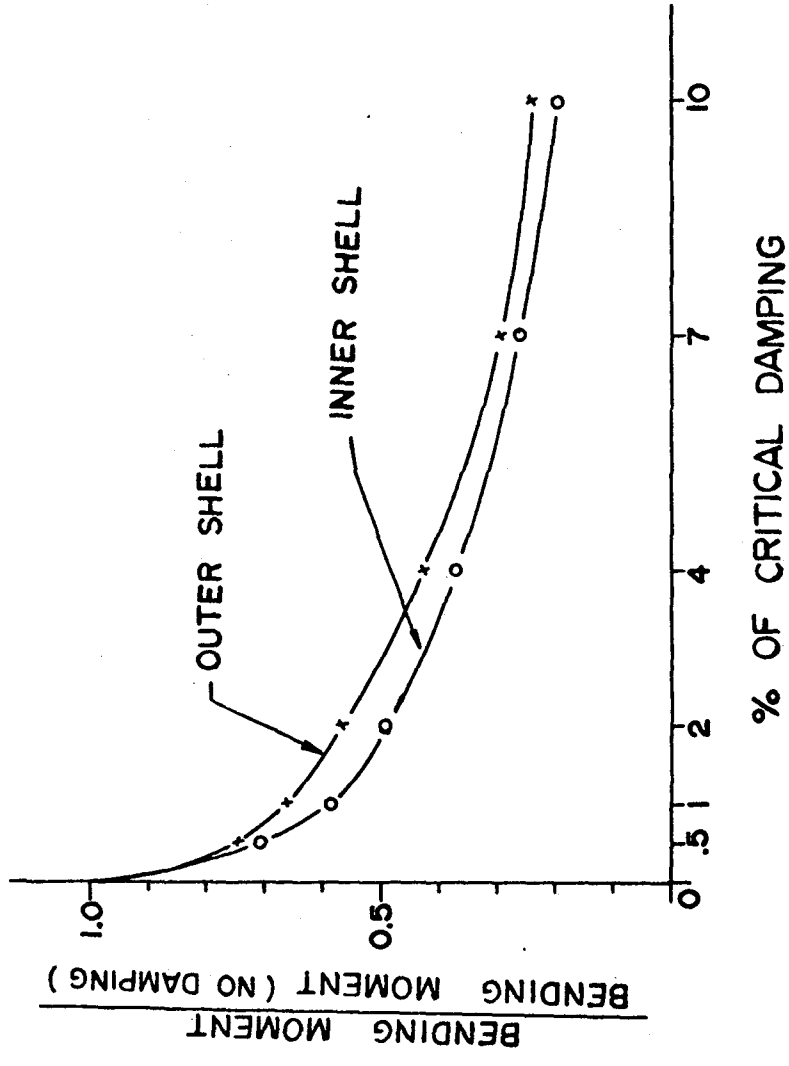

Figure 4.15 Variation of base bending moment with damping for both shells

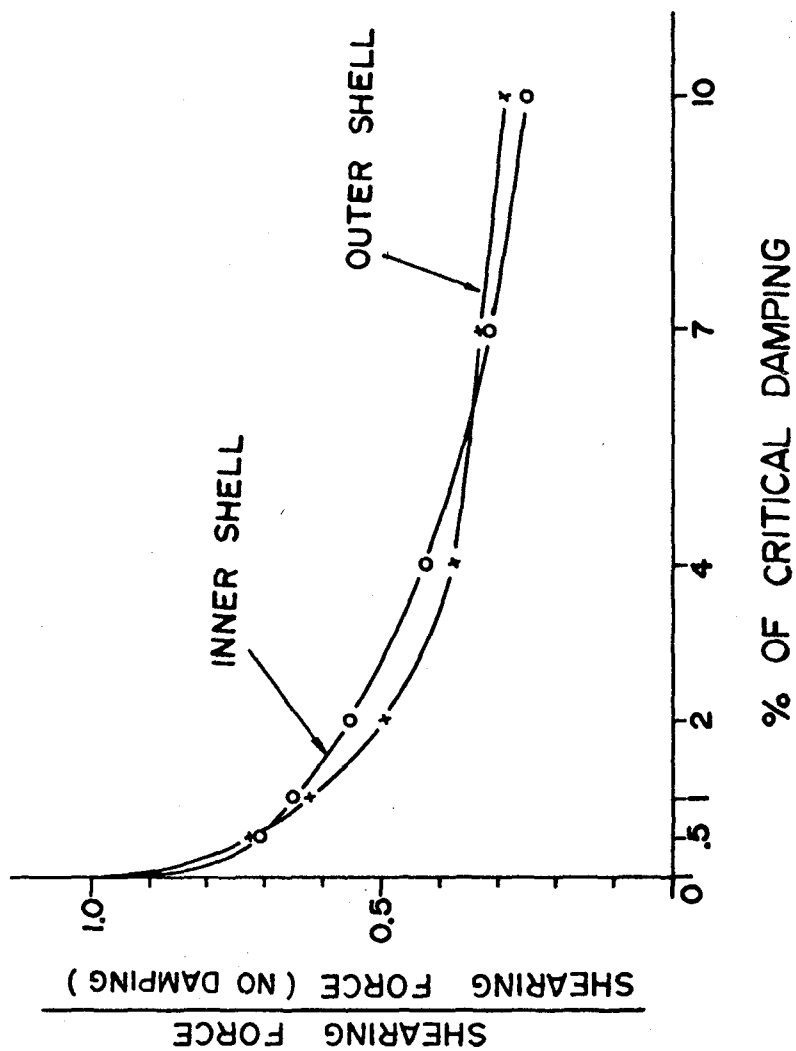

Figure 4.16 Variation of base shearing force with damping for both shells.

(4) Response to the vertical component of an earthquake (without crack)

The vertical component of the acceleration record of El Centro earthquake is shown in Figure 4.17. It is seen that the vertical component of the acceleration oscillates at a frequency of around 8 to 9 Hertz. From Tables II and III, it is learned that the second natural frequency of the vertical modes is 10.5 Hertz for the outer shell and 11.3 Hertz for the inner shell. Therefore, the first two vertical modes are used to simulate the response behaviors.

The maximum absolute values of the axial forces and the axial stresses developed in the chimney due to this vertical component of the earthquake are shown in Figure 4.18. From the relatively small quantities of the resulting axial stresses in the concrete, it is learned that the effect of these axial stresses to the vertical seismic components is negligible as compared to that of the horizontal seismic components. Therefore, it is reasonable to consider the chimney as a beam instead of a beam-column in the present study.

(5) Stress concentration around the flue openings (without crack)

The stress distributions in the region around the two flue openings in each shell are studied by performing local analysis of the lowest beam finite element of each shell. This beam finite element is modeled by 244 quadrilateral plate finite elements. Both ends are subjected to the simultaneous actions of bending moment, shearing force and axial force caused by both the horizontal and vertical components of the earthquake. The most critical time for the outer shell is at 25.2 seconds when the base bending moment equals to 32.05×10^6 in-kips; the base shearing force equals to 11,810 kips; and the base axial force equals to 217.7 kips. For the inner shell,

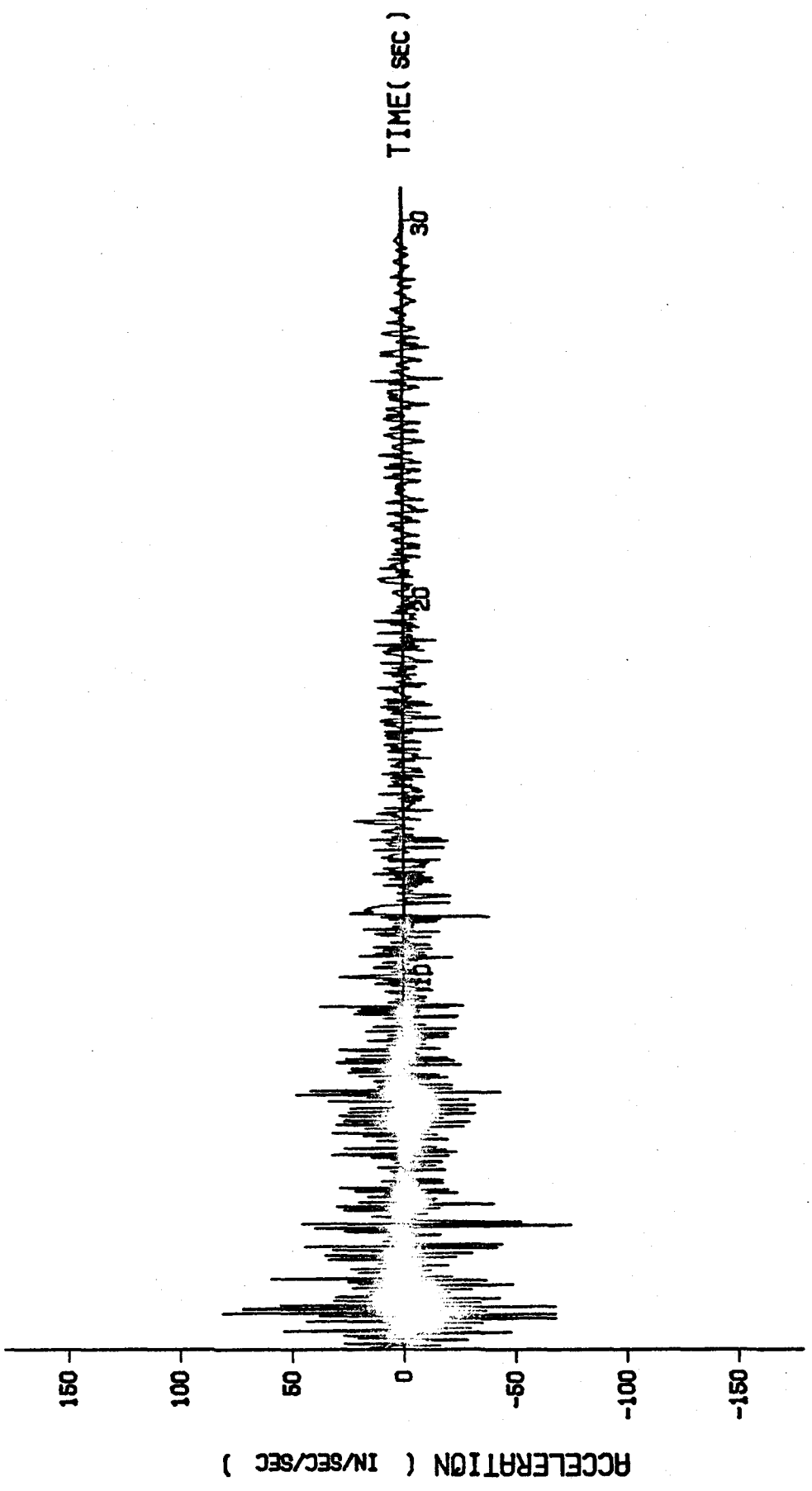

Figure 4.17 Ground acceleration, El Centro earthquake of May 18, 1940, vertical component.

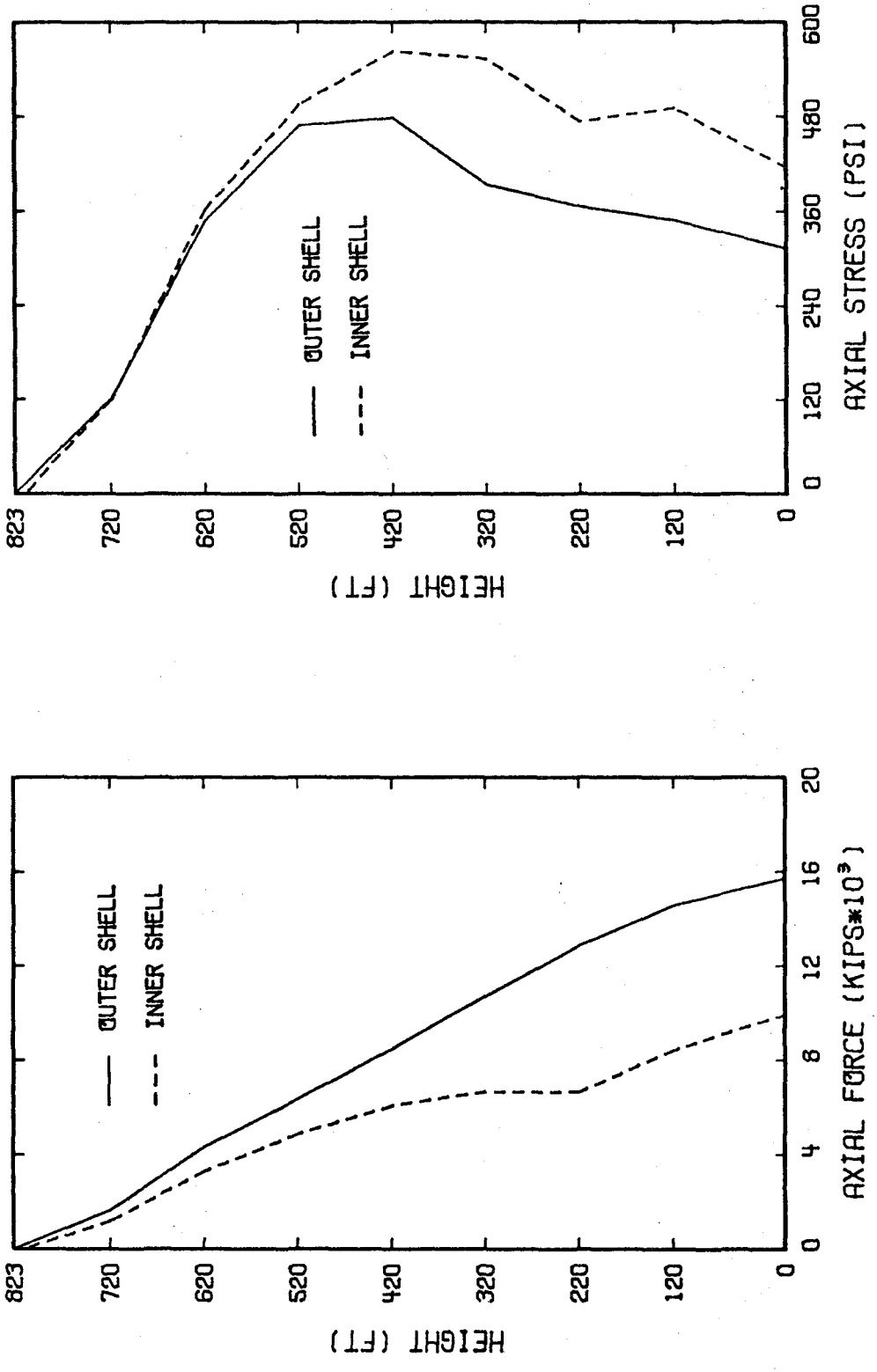

Figure 4.18 Maximum axial force and maximum axial stress versus height for both shells.

the most critical time is at 28.8 seconds when the base moment equals to 11.28 x 10^6 in-kips; the base shearing force equals to 4,557 kips; and the base axial force equals to 150.5 kips. Figures 4.19 and 4.20 show the contour plots of the resulting bending stresses in the outer surfaces of the outer shell and the inner shell, respectively. Because of symmetry, only one half of the shell segment with one opening is shown. The highest stresses due to the openings are about 2500 psi to 3000 psi for both shells. It seems that these stresses around the openings are not very high if compared to the maximum bending stresses at the base. This is due to the heavily reinforced concrete around the flue openings.

(b) Response of the chimney to horizontal component of the earthquake (with crack)

In the previous analyses, the concrete is assumed not to crack under tensile stress. This may not be true because the tensile strength of the concrete is very low (about 500 psi). Therefore, in this section, it is assumed that the concrete has no tensile capacity and all the tensile stresses are taken by the reinforced steel. Based on this assumption, the problem is simplified. As shown in Figure 4.21, the transformed section of the chimney consists of the concrete in compression on one side of the neutral axis, and the steel area on the other. The distance to the neutral axis is expressed as a fraction k of the diameter d. To determine the location of the neutral axis, the resultant compressive force on the compression side is set equal to the resultant tensile force on the tension side, that is, the resultant force of the whole section is equal to zero. It is assumed that there is no external axial force acting on this section. The total compressive force c_f is

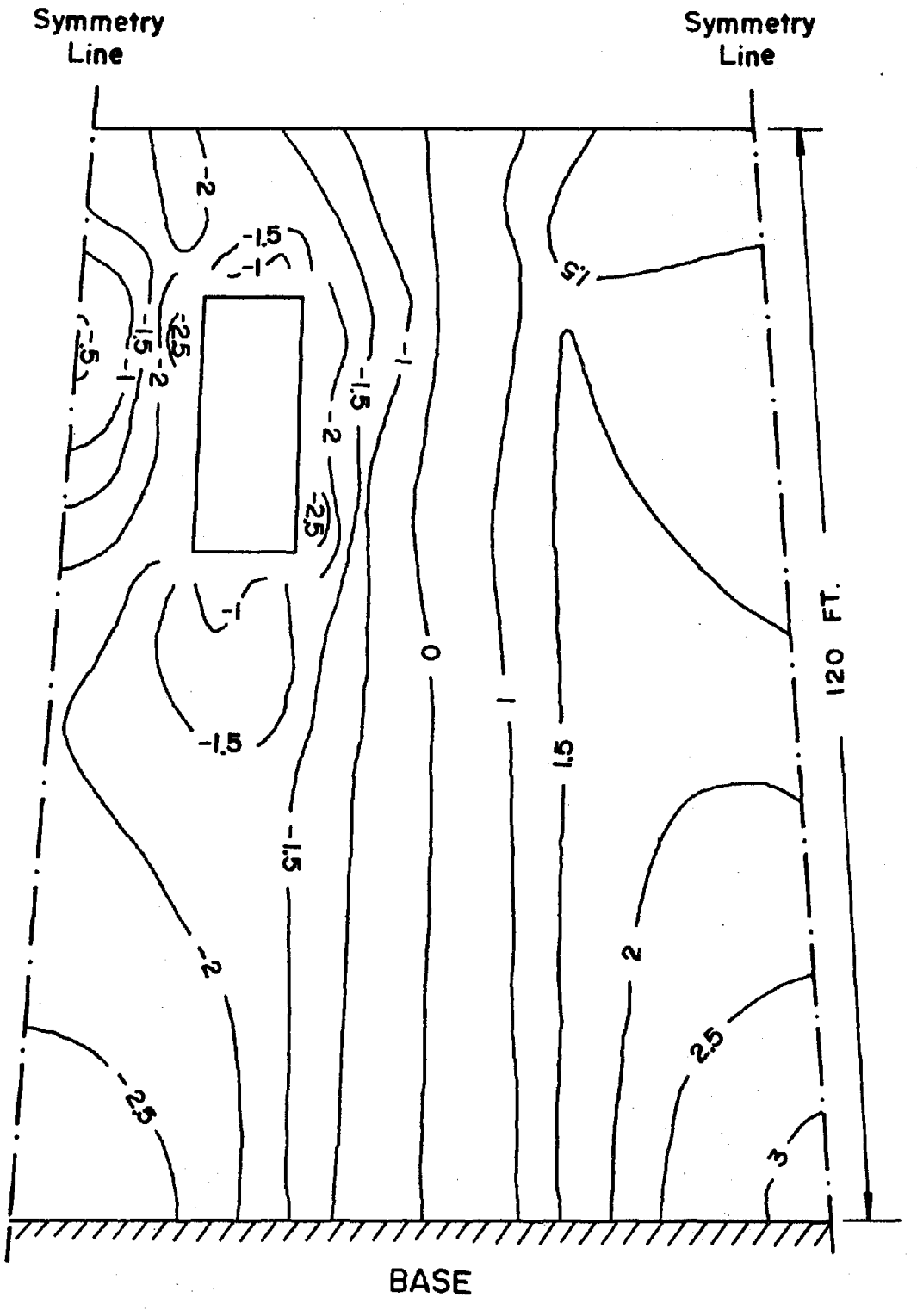

Figure 4.19 Stress distribution around the flue opening of outer shell.

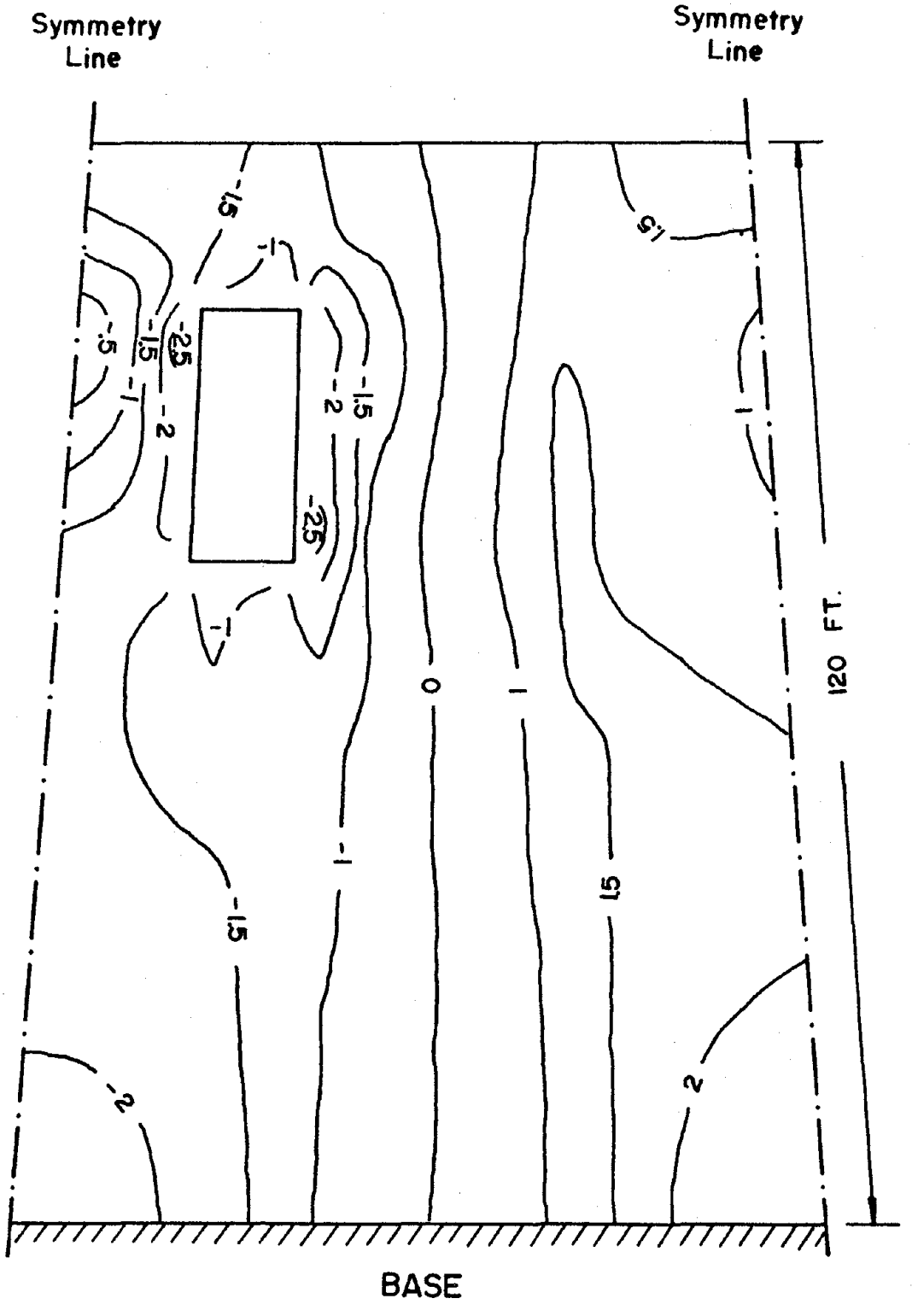

Figure 4.20 Stress distribution around the flue opening of inner shell.

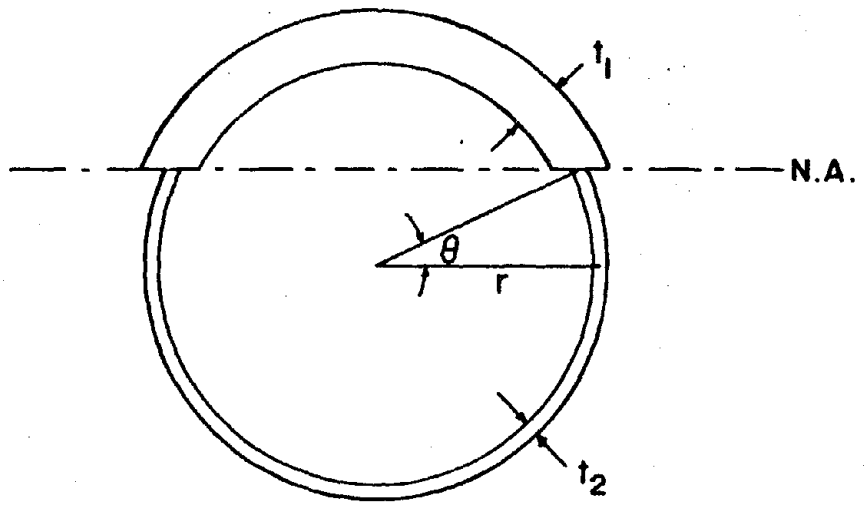

Figure 4.21 Transformed cross section of the outer shell (with cracks).

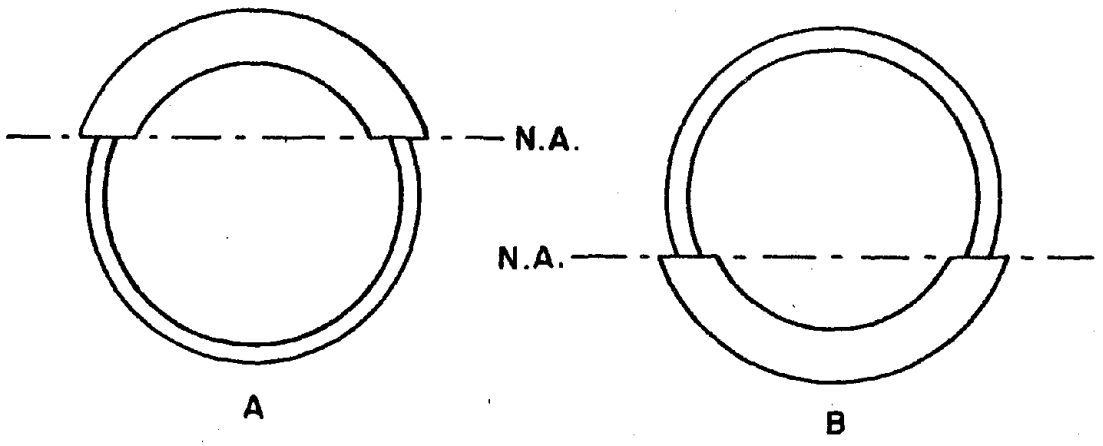

Figure 4.22 Location of the neutral axis of a cracked pipe-type section during vibration.

$$c_f = \int_0^{\frac{\pi}{2}} rt_1 f_c (r \sin\psi - r \sin\theta) d\psi/kd$$

$$= \frac{rt_1 f_c}{1 - \sin\theta} \left[\cos\theta - \left(\frac{\pi}{2} - \theta\right) \sin\theta\right]$$

and the total tensile force T_f is

$$T_f = \int_{-\theta}^{\frac{\pi}{2}} rt_2 f_c (r \sin\psi + r \sin\theta) d\psi/kd$$

$$= \frac{rt_2 f_c}{1 - \sin\theta} \left[\cos\theta + \left(\frac{\pi}{2} + \theta\right) \sin\theta\right]$$

Since $c_f = T_f$, we obtain

$$\cot\theta + \theta = \frac{\pi}{2} \frac{(t_1 + t_2)}{(t_1 - t_2)} \tag{4.8}$$

and $$kd = \frac{d}{2} (1 - \sin\theta)$$

In the above equation, the quantity kd which determines the location of the neutral axis is a function of thicknesses t_1 and t_2 only. In other words, the location of the neutral axis is not dependent on the magnitude of the bending moment. If the bending moment changes its sign from positive to negative or vice versa, the position of the neutral axis jumps from A to B as shown in Figure 4.22 and there is no gradual shift of the position of the neutral axis. Because the location of the neutral axis is not changed, the moment of inertia of the section is also kept constant during the course of vibration. In such situation, the problem is apparently simplified and only the stiffness of the chimney is decreased due to the crack.

Table IV shows the geometric data for the 8 elements of both shells when the concrete is considered to have no tensile capacity. In order to use SAP IV for the analysis, the unsymmetric cracked section as shown in Figure 4.21 will

Table IV. Geometric Quantities for the Chimney with Cracks

Element Number	Outer Shell					
	ℓ(in)*	D(in)*	t_1(in)*	t_2(in)*	t'(in)*	m/unit ℓ*
1	1440	783.0	20.5	0.507	1.320	11.28
2	1200	694.3	19.17	0.765	1.897	9.331
3	1200	624.9	17.88	1.009	2.393	7.842
4	1200	568.6	15.17	1.068	2.452	6.043
5	1200	525.7	10.92	0.912	2.034	3.999
6	1200	492.3	8.733	0.695	1.564	2.985
7	1200	468.8	8.358	0.409	0.977	2.721
8	1233	455.8	9.401	0.173	0.461	2.983
Element Number	Inner Shell					
	ℓ(in)	D(in)	t_1(in)	t_2(in)	t'(in)	m/unit ℓ
1	1400	637.2	11.94	0.268	0.705	5.188
2	1200	529.9	10.30	0.205	0.543	3.725
3	1200	467.6	9.54	0.188	0.499	3.044
4	1200	423.1	9.04	0.184	0.487	2.608
5	1200	387.4	8.86	0.263	0.673	2.340
6	1200	360.6	8.67	0.339	0.843	2.133
7	1200	343.9	8.35	0.252	0.644	1.958
8	1104	334.6	9.39	0.163	0.436	2.144

* ℓ = length of the element (inch)
D = diameter of the element (inch)
m = mass of the element (slug)
t_1 = thickness on uncracked side of the section
t_2 = thickness on cracked side of the section
t^{τ} = the equivalent thickness (inch)

be transformed to a symmetric section in which the moment of inertia is unchanged. The thicknesses of the transformed sections are shown in Table IV as t'.

Table V shows the first 12 natural frequencies and periods of the outer and the inner shells with the crack. Due to the effect of the crack, the periods shown in this table are longer than those shown in Tables II and III, that is, the chimney becomes more flexible. Because the frequencies of the cracked chimney are low, a total of nine flexural modes of each shell are used for the seismic response analysis. Figure 4.23 shows 30 seconds time-history response of the tip deflection for the outer shell due to the south-north components of the El Centro earthquake. The maximum tip deflection is found to be of 53.2 inches at 27.2 seconds. This value is greater than the maximum tip deflection of the outer shell without crack. Intuitively, this seems reasonable because the stiffness of the chimney is weakened by the crack. However, the seismic response of the chimney depends not only on the stiffness of the chimney but also mainly on the relationship between natural frequencies of the chimney and the frequencies of the ground excitation. Although the stiffness of the chimney is decreased by about 80 ~ 95% due to the crack, the deflection of the cracked chimney may not necessarily be greater than that of the uncracked chimney. In order to prove this point, a case was also studied in which the stiffnesses of the outer shell were unchanged but the mass of the outer shell is decreased by 10% at each nodal point. The results show that the tip deflection of the outer shell is 53.2 inches for the case without crack and 39.5 inches for the case with crack. The totally reversed results show that maximum deflection of the chimney with crack may not be greater than that without crack.

Table V. The Natural Frequencies and Periods for the Chimney with Crack.

Mode Number	Outer Shell		Mode Number	Inner Shell	
	Frequency (rad/sec)	Period (sec.)		Frequency (rad/sec)	Period (sec)
1	0.631	9.954	1	0.305	20.603
2	2.413	2.604	2	1.464	10.291
3	5.447	1.154	3	3.498	1.796
4	9.218	0.682	4	6.104	1.029
5*	10.141	0.620	5*	6.793	0.925
6	13.849	0.454	6	9.190	0.684
7	19.241	0.327	7	12.469	0.504
8*	21.942	0.286	8	15.808	0.397
9	25.326	0.248	9	18.205	0.345
10	31.535	0.199	10*	18.447	0.341
11*	35.138	0.179	11*	27.873	0.225
12*	45.499	0.138	12*	36.813	0.171

* Longitudinal modes

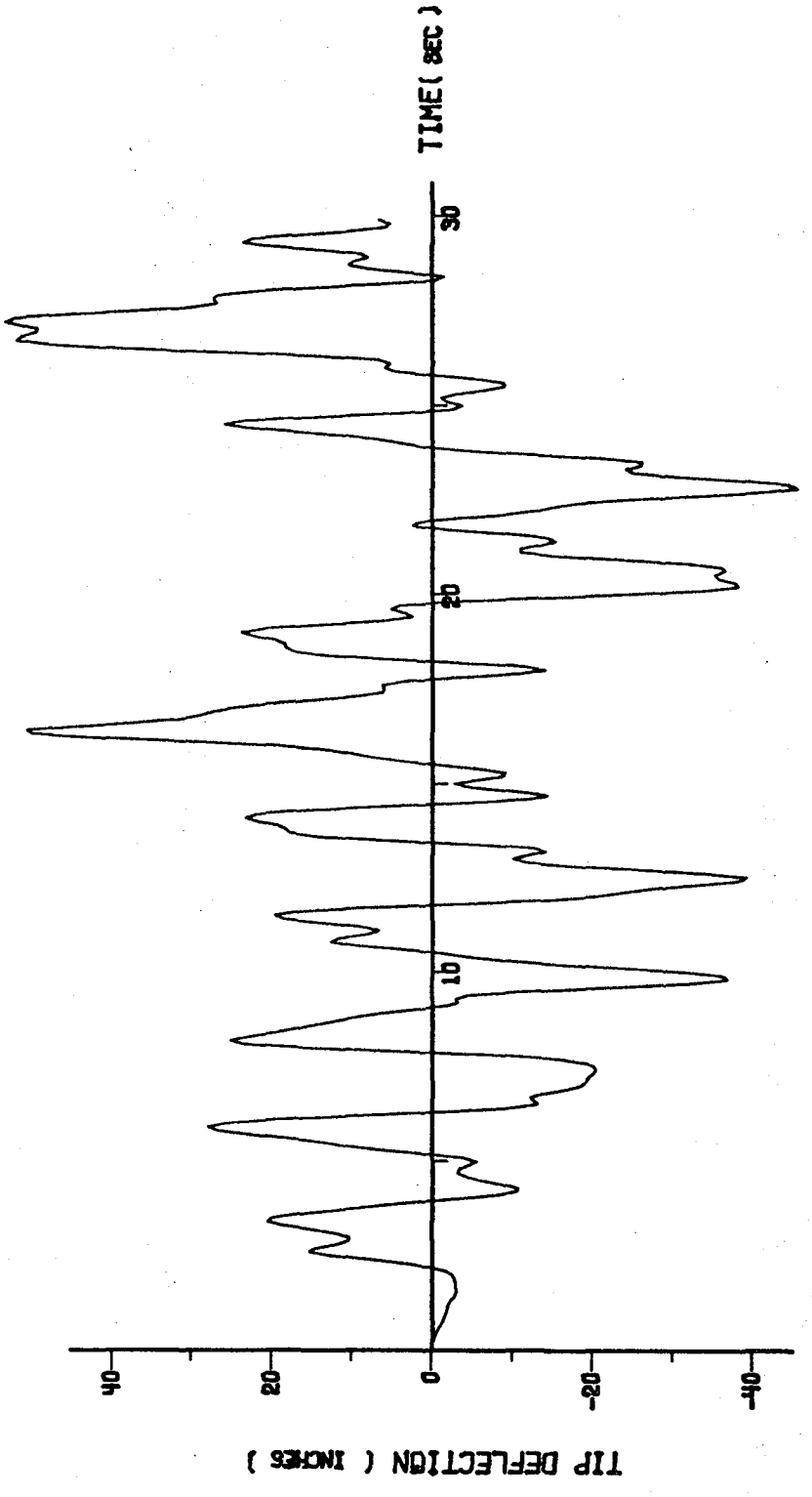

Figure 4.23 Time history response for the tip deflection of outer shell (with cracks).

Figure 4.24 shows the time history response for the tip deflection of the inner shell with crack. The maximum tip deflection is 35.4 inches at 14.3 seconds which is greater than the maximum tip deflection of the inner shell without crack. Due to the rather large magnitude of tip deflections of both the outer and the inner shells with crack, the two shells collide with each other when the net tip spacings are negative. By neglecting the nonlinearity due to collision, time history results for net tip spacings between the two shells are given in Figure 4.25.

Figure 4.26 show the maximum bending moment and the maximum shearing force distributed along the height of the outer and inner shells. Equation (3.7) indicates that the nodal forces are directly proportional to the stiffness of the chimney, therefore, the bending moments and the shearing forces shown in Figure 4.26 for the less stiff chimney with cracks are smaller than those shown in Figures 4.11. The corresponding bending stresses in the steel and in the concrete for both shells are shown in Figure 4.27. Because the tensile force is entirely taken by the reinforced steel, the tensile stresses developed in the steel due to the earthquake are very high at some sections as shown in Figure 4.27. The compressive stresses developed in the concrete are everywhere within safe limits.

(7) The effect of shear deformation on the deflection of chimney

Figure 4.28 shows cantilever having a thin pipe-type cross section bent by a force P applied at the end. The tip deflection of this beam including the effect of shear deformation is

$$\delta = \frac{P\ell^3}{3EI} + \frac{\bar{\alpha}P\ell}{GA} \qquad (4.9)$$

in which G is the modulus in shear, A is the cross sectional area, and $\bar{\alpha}$ is the shape factor with which the average shearing stress must be multiplied

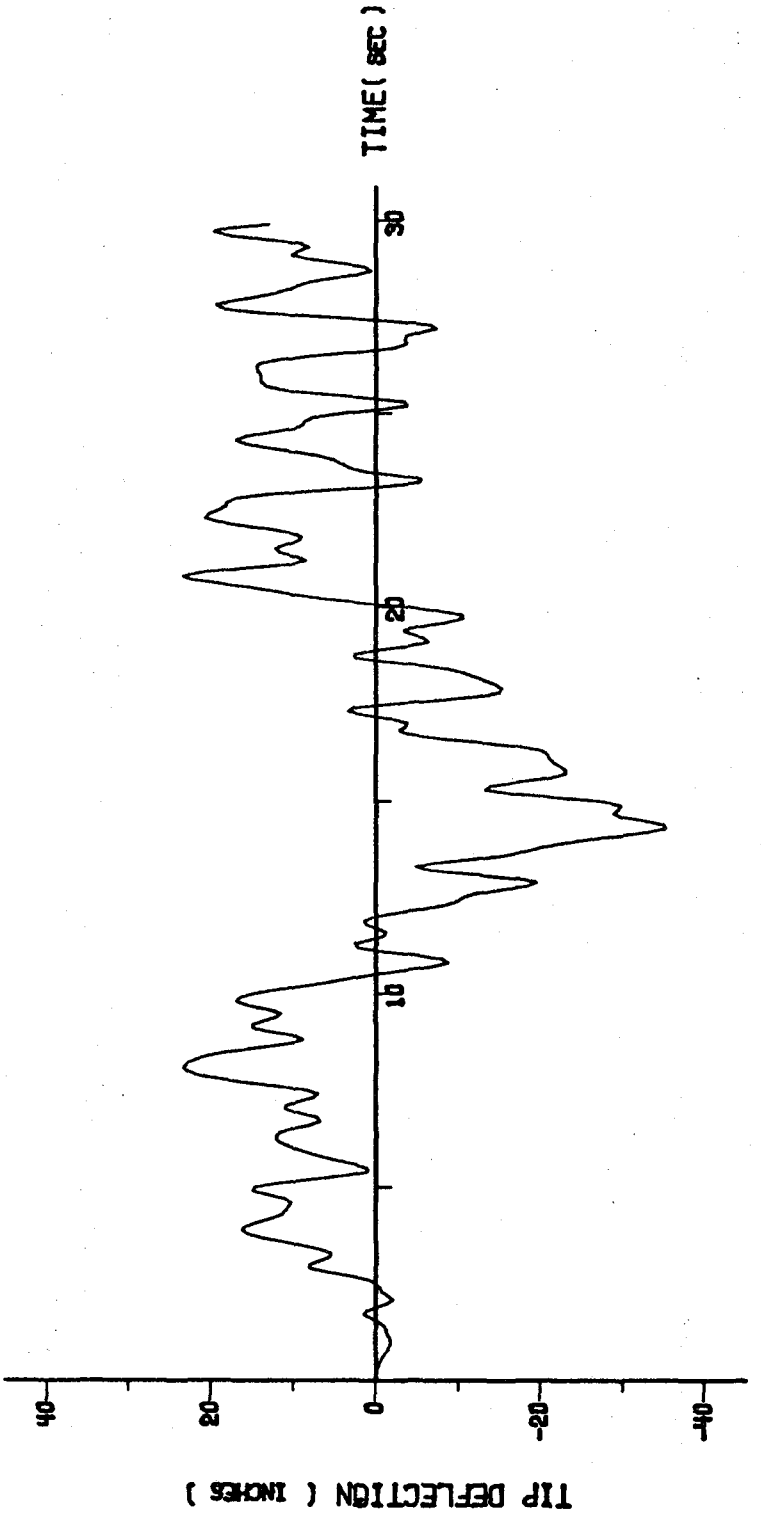

Figure 4.24 Time history response for the tip deflection of inner shell (with cracks).

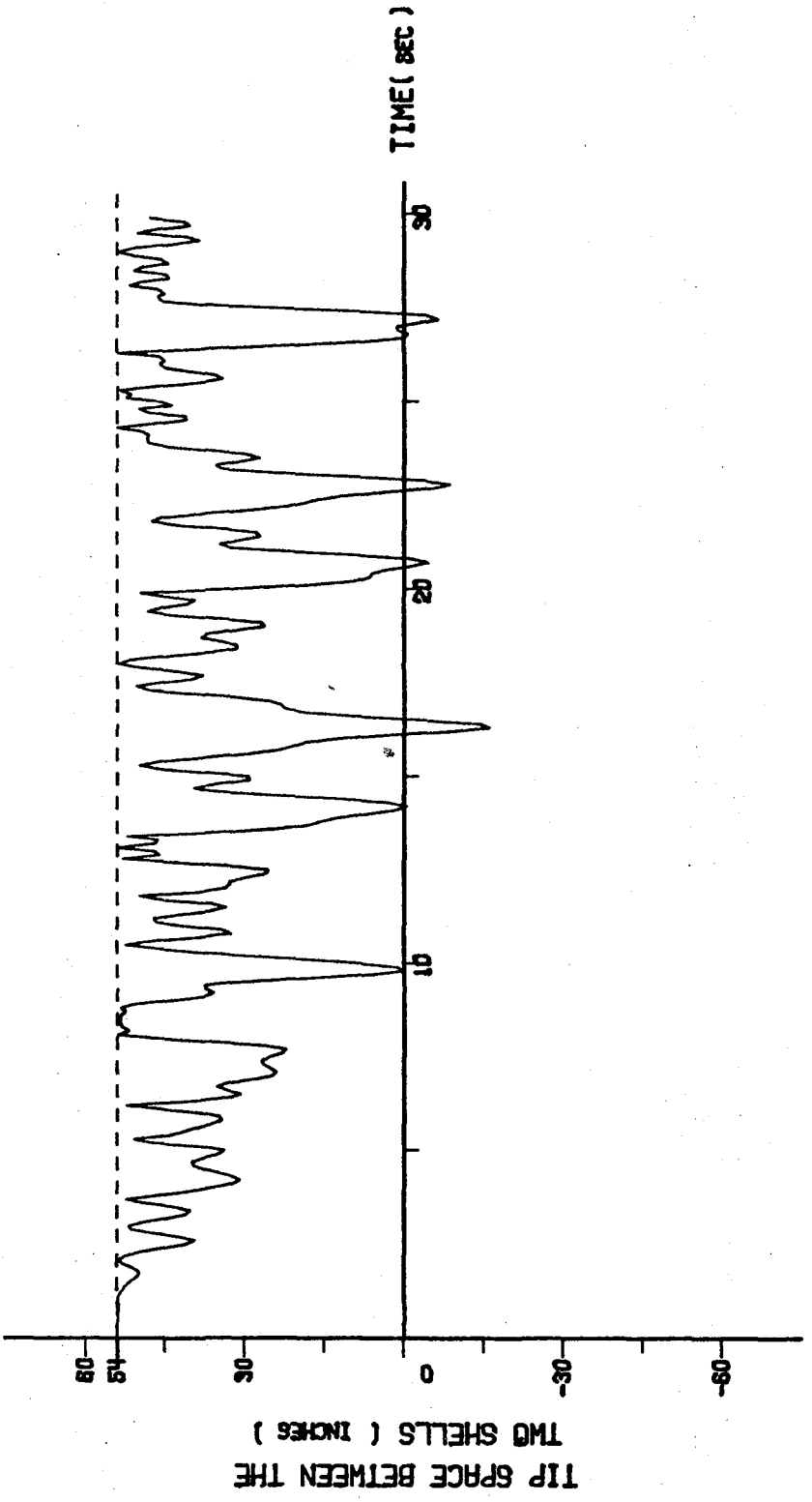

Figure 4.25 Time history curve for the spacing between tops of outer and inner shells (with cracks).

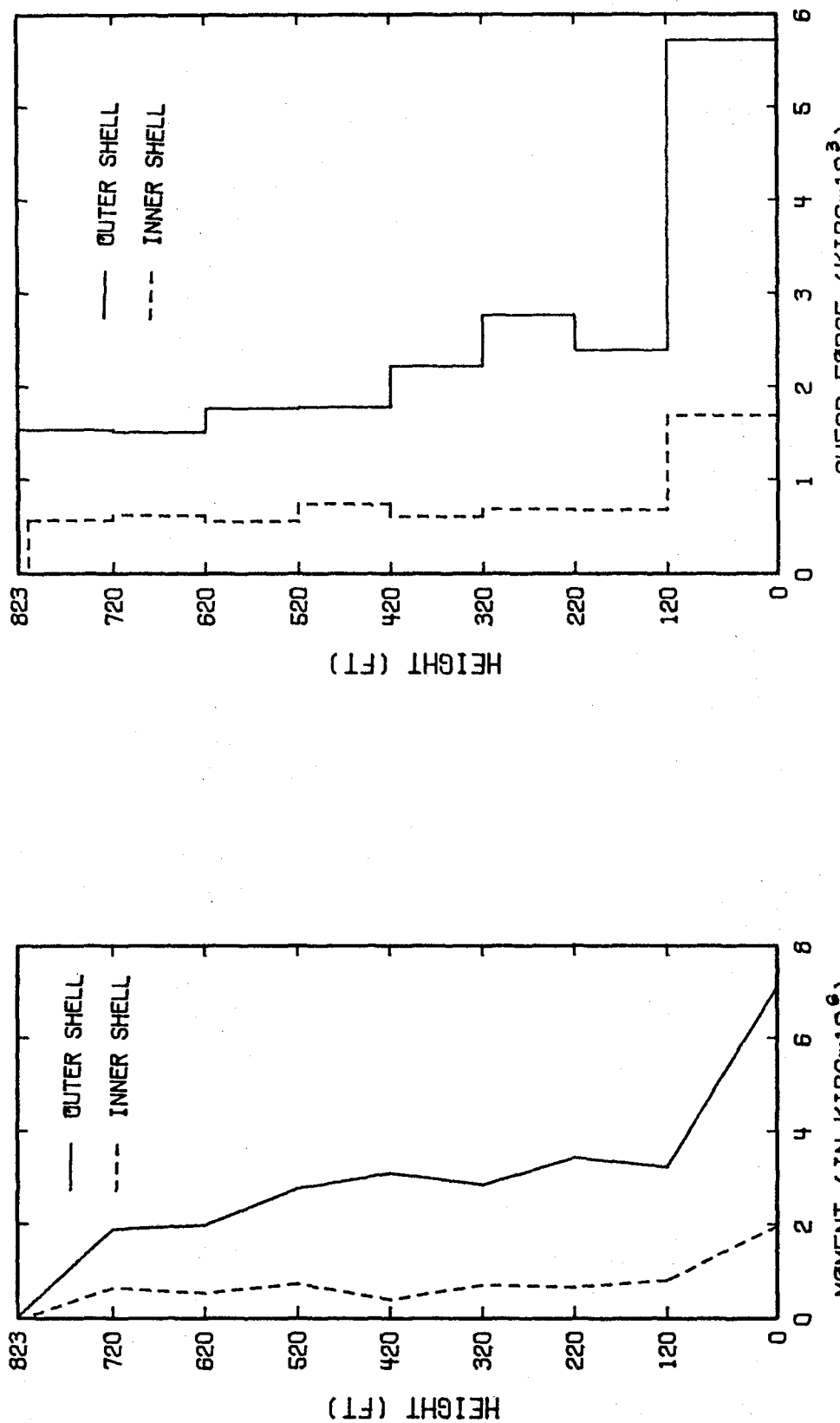

Figure 4.26 Maximum bending moment and maximum shearing force versus height for both shells (with cracks).

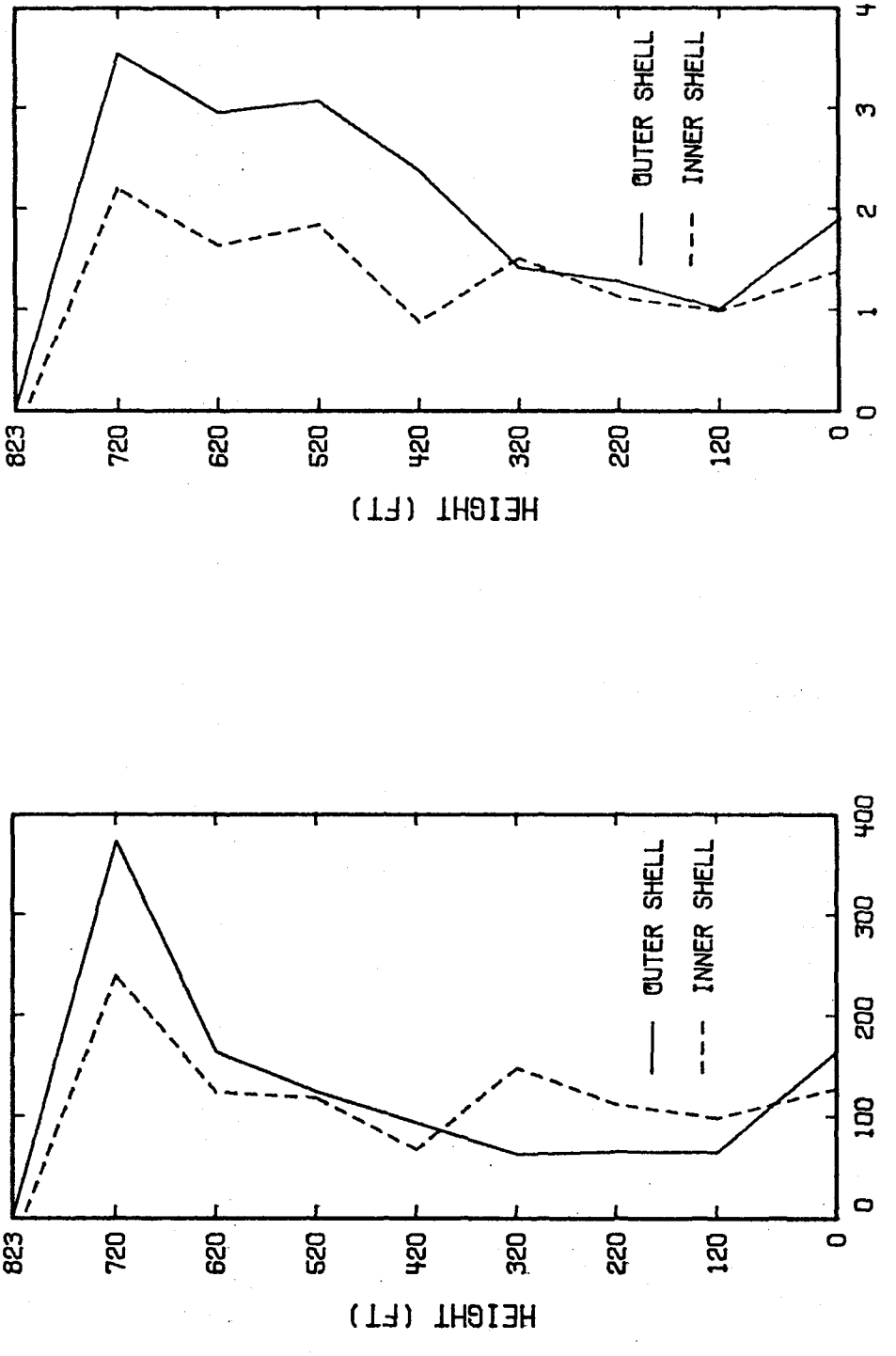

Figure 4.27 Steel and concrete stress curves for both shells (with cracks).

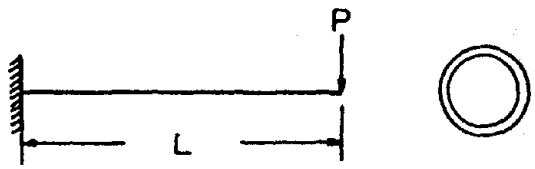

Figure 4.28 Cantilever pipe-type beam.

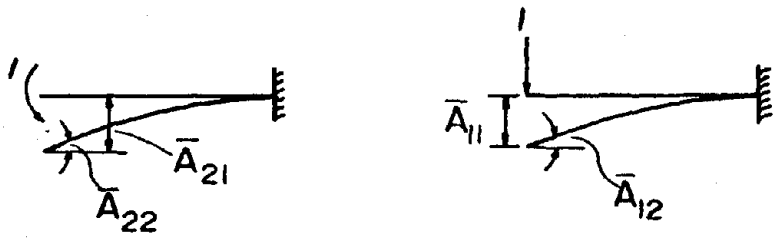

Figure 4.29 Flexibility coefficients for a cantilever beam.

in order to obtain the shearing stress at the centroid of the cross section. For a pipe, with circular cross section, $\bar{\alpha} = 2.0$. The second term on the right side of Equation (4.9) is the additional deflection due to the shear deformation.

In the present case, the Poisson's ratio is assumed as 0.1667 and the modulus in shear is defined as $G = E/2(1 + \mu)$. Equation (4.9) is reduced to

$$\delta = \frac{P\ell^3}{3EI}\left[1 + 1.75\left(\frac{d}{\ell}\right)^2\right] \tag{4.10}$$

For the chimney, the ratio of the diameter d to the length ℓ is approximately equal to 0.06 and the effect of the shear deformation on the deflection is about 0.6% for the static case.

For dynamic case, the effect of the shear deformation on the deflection can be included in the stiffness matrix [K]. One way of obtaining the stiffness matrix is to first obtain the flexibility matrix and then inverting the flexibility matrix. The flexibility matrix, for a cantilever subjected to a unit load at the free end (Figure 4.29) is given as matrix $[\bar{A}]$ in Equation (4.11) and its corresponding stiffness matrix is given as matrix $[\bar{B}]$ in Equation (4.11).

$$[\bar{A}] = \begin{bmatrix} \ell^3/3EI & -\ell^2/2EI \\ -\ell^2/2EI & \ell/EI \end{bmatrix} \qquad [\bar{B}] = \begin{bmatrix} 12EI/\ell^3 & 6EI/\ell^2 \\ 6EI/\ell^2 & 4EI/\ell \end{bmatrix} \tag{4.11}$$

In the effect of the shear deformation on the deflection (neglecting this effect on the slope) is considered, the flexibility matrix $[\bar{A}]$ in Equation (4.11) is modified as

$$[A_v] = \begin{bmatrix} \ell^3/3EI + \alpha\ell/GA & -\ell^2/2EI \\ -\ell^2/2EI & \ell/EI \end{bmatrix}$$

and the inverse of this matrix is

$$[B_v] = \begin{bmatrix} \frac{12EI}{\ell^3} Q & \frac{6EI}{\ell^2} Q \\ \frac{6EI}{\ell^2} Q & \frac{3EI}{\ell} Q + \frac{EI}{\ell} \end{bmatrix}$$

where $Q = \dfrac{A\ell^2}{A\ell^2+24\bar{\alpha}(1+\mu)I_Z}$. Following to preceding procedures, the stiffness matrix for a beam element which includes the effect of the shear deformation on the deflection can be obtained as follows.

$$[K_v] = \frac{EIQ}{\ell} \begin{bmatrix} 12/\ell^2 & 6/\ell & -12/\ell^2 & 6/\ell \\ 6/\ell & 3+1/Q & -6/\ell & 3-1/Q \\ -12/\ell^2 & -6/\ell & 12/\ell^2 & -6/\ell \\ 6/\ell & 3-1/Q & -6/\ell & 3+1/Q \end{bmatrix} \tag{4.12}$$

If the effect of the shear deformation is very small and negligible (i.e. $Q \simeq 1.0$), the stiffness matrix $[K_v]$ reduces to the normal stiffness matrix $[K]$.

Because $[K_v]$ is smaller than $[K]$, due to the effect of the shear deformation, the natural frequencies shown in Tables II and III are only slightly less than those obtained by using $[K]$ as shown in Table VI. Although the shear deformation appears to have small effect on the natural frequencies and their corresponding normal mode shapes of the chimney, its effect on the seismic response of the chimney is, however, not so small. Figure 4.30 shows the comparison between two cases, one including and one excluding the effect of shear deformation for the maximum

Table VI. The Natural Frequencies and Periods for the Chimney (excluding the effect of shear deformation).

Mode Number	Outer Shell		Mode Number	Inner Shell	
	Frequency (rad/sec)	Period (sec)		Frequency (rad/sec)	Period (sec)
1	1.986	3.164	1	1.282	4.901
2	7.241	0.868	2	5.733	1.096
3	17.877	0.351	3	14.225	0.442
4*	31.387	0.200	4	26.450	0.238
5	33.166	0.189	5*	28.034	0.224
6	53.373	0.118	6	42.159	0.149
7*	65.275	0.096	7	60.482	0.104
8	77.489	0.081	8*	70.369	0.089
9	103.53	0.061	9	78.812	0.080
10*	109.30	0.057	10	102.63	0.061
11	132.20	0.048	11*	110.86	0.057
12*	145.75	0.043	12*	148.85	0.042

* Longitudinal modes

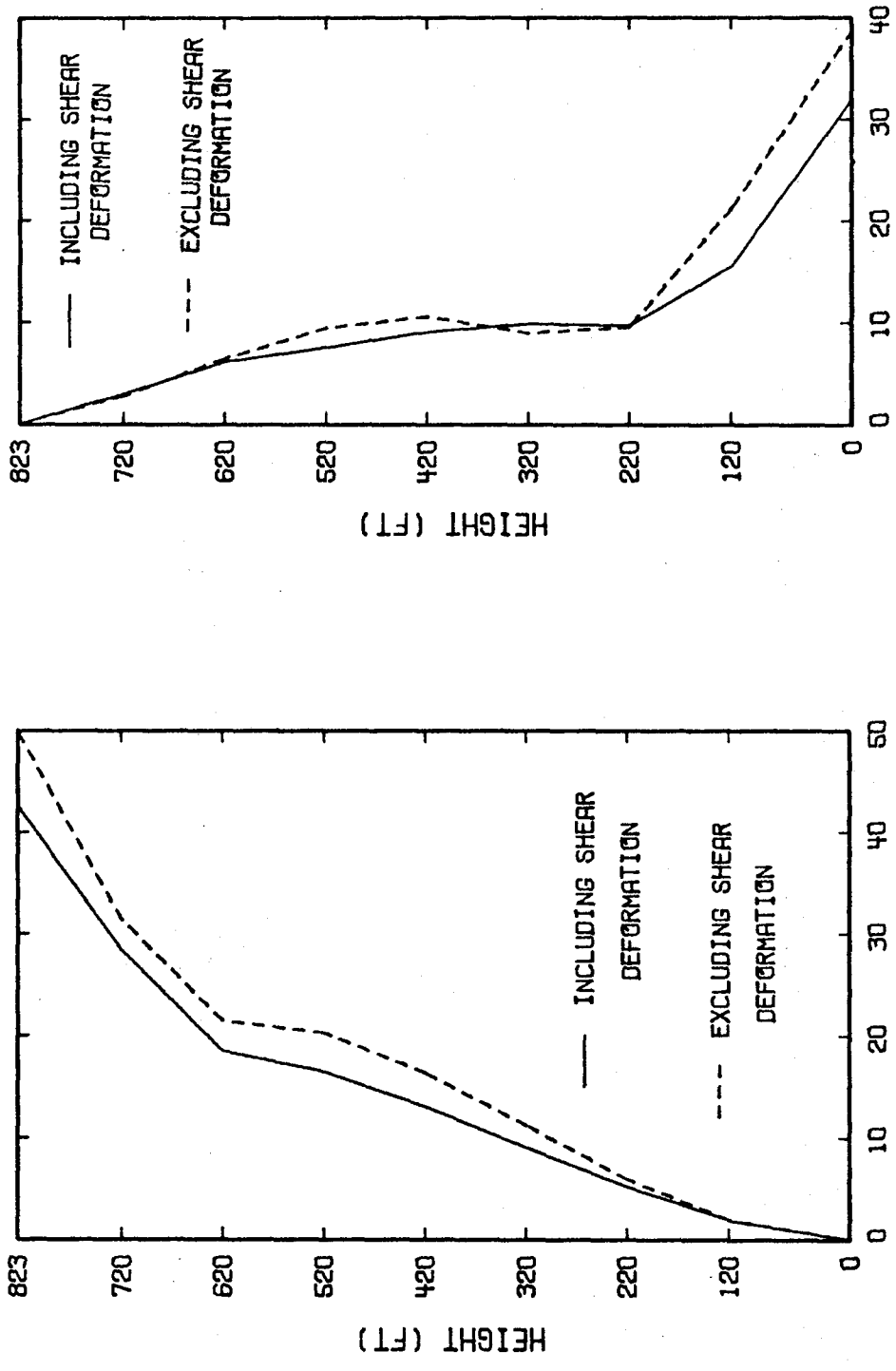

Figure 4.30 Deflections and moments versus height of outer shell for cases with and without shear deformation.

deflections and bending moments of the outer shell. As mentioned earlier, the response of the chimney to the earthquake is mainly dependent on the relationship between the natural frequencies of the chimney and the earthquake. It is possible that the maximum tip deflection of the outer shell including the effect of the shear deformation is smaller than that excluding the effect of the shear deformation although the shear deformation tends to increase the deflection of the chimney in a static case.

4.2 Spectrum Analysis of a Chimney

The time history analysis method is a time-consuming method. This method is particularly expensive for structures with high number of degrees of freedom. For analyzing complex structures, it may be beyond the capabilities of some design offices. Therefore, it would be desirable to have a simpler analytical method for practical purpose which can give reliable results. The response spectrum analysis method to be described in this section is provided for this purpose.

In Equation (4.7), the response of the n^{th} vibration mode, $Y_n(t)$, depends directly upon the magnitude of the integral

$$x_n = \int_0^t \ddot{y}_g(\tau) e^{-\zeta_n \omega_n (t-\tau)} \sin \omega_n (t-\tau) d\tau \qquad (4.13)$$

This integral is a function of the ground acceleration, damping ratio, natural frequency of the structure, and the time at which the integral is evaluated.

Several methods have been used for calculating the integration; one of these is a direct numerical integration method. However, the measured ground accelerations obtained from a strong-motion earthquake record are usually a zigzag curve as shown in Figure 4.3. The acceleration function between two consecutive record time points is assumed to be linear, i.e.,

$$\ddot{y}_g(\tau) = a_1 + b_1\tau \qquad \text{for} \quad \tau_i \leq \tau \leq \tau_{i+1}$$

Equation (4.13) can be expressed as a summation of a number of subintegrals as the following:

$$x_n = \int_0^t \ddot{y}_g(\tau)e^{-\xi_n\omega_n(t-\tau)} \sin \omega_n(t-\tau)d\tau$$

$$= \int_0^{\tau_1} \ddot{y}_g(\tau)f(\tau)d + \int_{\tau_1}^{\tau_2} \ddot{y}_g(\tau)f(\tau)d\tau + \cdots\cdots\cdots$$

$$+ \int_{\tau_i}^{\tau_{i+1}} \ddot{y}_g(\tau)f(\tau)d\tau + \cdots\cdots\cdots + \int_{\tau_n}^{t} \ddot{y}_g(\tau)f(\tau)d\tau \qquad (4.14)$$

where $\ddot{y}_g(\tau)$ is linear in each subintegral and $f(\tau) = e^{-\xi_n\omega_n(t-\tau)} \sin \omega_n(t-\tau)$

These subintegrals can be directly integrated as the following:

$$\int_{\tau_i}^{\tau_{i+1}} \ddot{y}_g(\tau)e^{-\xi_n\omega_n(t-\tau)} \sin \omega_n(t-\tau)d\tau$$

$$= \int_{\tau_i}^{\tau_{i+1}} (a_1 + b_1\tau)e^{-\xi_n\omega_n(t-\tau)} \sin \omega_n(t-\tau)d\tau$$

$$= \left[\frac{(a_1 + b_1\tau)e^{-\xi_n\omega_n(t-\tau)}}{(\xi_n^2 + 1)\omega_n} \{\xi_n \sin \omega_n(t-\tau) + \cos \omega_n(t-\tau)\}\right.$$

$$- \frac{b_1\xi_n e^{-\xi_n\omega_n(t-\tau)}}{(\xi_n^2 + 1)^2\omega_n^2} \{2 \cos \omega_n(t-\tau) + \xi_n \sin \omega_n(t-\tau)\}$$

$$\left. + \frac{b_1 e^{-\xi_n\omega_n(t-\tau)}}{(\xi_n^2 + 1)^2\omega_n^2} \sin \omega_n(t-\tau)\right]_{\tau_i}^{\tau_{i+1}}$$

$$= [g(\tau)]_{\tau_i}^{\tau_{i+1}} \tag{4.15}$$

Substituting Equation (4.15) into Equation (4.14), it becomes

$$x_n = [g(\tau)]_0^{\tau_1} + [g(\tau)]_{\tau_1}^{\tau_2} + \ldots\ldots + [g(\tau)]_{\tau_i}^{\tau_{i+1}} + \ldots\ldots + [g(\tau)]_{\tau_n}^{t} \tag{4.16}$$

The computing time required to obtain the solution of X_n by Equation (4.16) for a given earthquake acceleration history $\ddot{y}_g(\tau)$, a known damping value ξ_n, and a definite integral time t is approximately 5 percent of the computer time required by a direct numerical integration method whereas the result is apparently more accurate.

X_n has the dimension of velocity; its maximum value is called the spectral velocity of the earthquake ground acceleration and is designated as S_v, i.e.,

$$S_{v_n} = \left[\int_0^t \ddot{y}_g(\tau) e^{-\xi_n \omega_n (t-\tau)} \sin \omega_n (t-\tau) d\tau\right]_{max}$$

It is seen from this equation that for a given earthquake acceleration history, $\ddot{y}_g(\tau)$, the spectral velocity depends only upon the frequency of vibration, ω_n, and the damping ratio, ξ_n. Thus a family of spectral velocity curves can be constructed for any given earthquake, each curve representing the maximum velocity as a function of frequency for a given damping ratio.

Two other frequently used spectral response quantities which are closely related to the spectral velocity are the spectral acceleration, S_a, and the spectral displacement, S_d. These represent the maximum modal acceleration and displacement, respectively, and are defined as follows:

$$S_{a_n} = \omega_n S_{v_n} \tag{4.17}$$

$$S_{d_n} = S_{v_n}/\omega_n \tag{4.18}$$

Thus, the maximum modal response quantities can be computed directly from the following equation

$$Y_{n_{max}} = \frac{F_n}{\bar{M}_n} S_{d_n} \tag{4.19}$$

For structures having only a single degree of freedom, Equation (4.19) gives the maximum displacement of the structure. However, in multi-degree-of-freedom structures the maximum response cannot be obtained directly from the modal maxima because the maxima of the various modes do not occur simultaneously. Two approximate methods are customarily used to obtain the total response; the square root of the sum of the squares of all maximum values and the sum of the absolutes of all maximum values. They are usually named as the probable maximum response and the absolute maximum response, respectively, with the former being used most frequently.

Results and Discussion

Figure 4.31 shows the response acceleration spectra for the El Centro earthquake with various degrees of damping. It is seen that damping has a significant effect on the magnitude and shape of the spectra, especially for the small damping value. Naturally, the zero-damping spectra are not as significant as the spectra with some damping because all structures have damping.

Because of the relationship among spectral velocity, spectral acceleration, and spectral displacement in Equations (4.17) and (4.18), it is possible to draw a figure to include all these quantities. So one can read

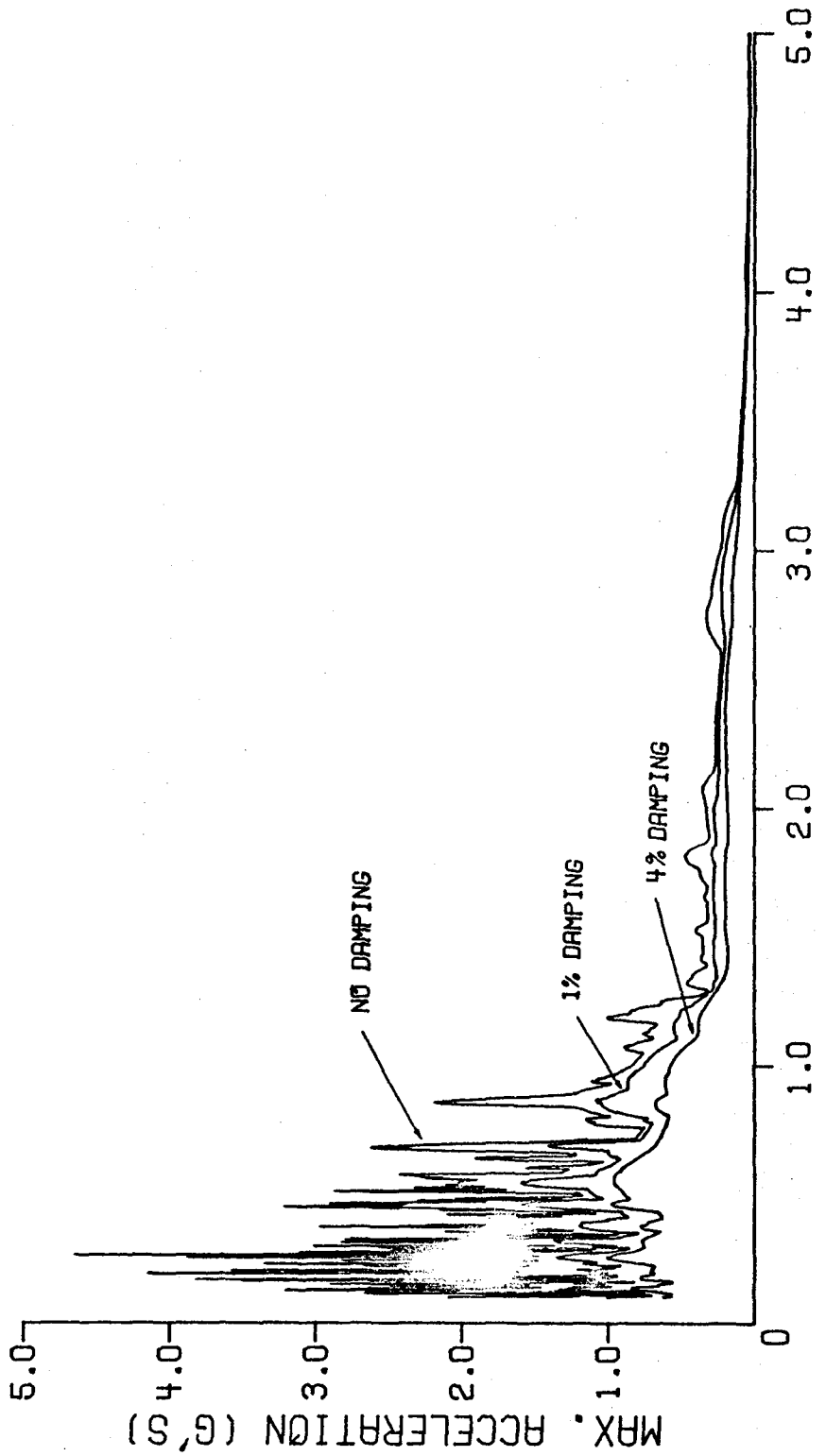

Figure 4.31 Acceleration spectra for elastic systems, 1940 El Centro earthquake (N-S component).

these three quantities from the same plot. Such plots for the outer shell based on uncracked section is shown in Figure 4.32. The polygon shown in this figure is the three bounds of ground motion: the line on the left is the maximum ground acceleration of 0.33 g, the line on the top is the maximum ground velocity of 13.7 in/sec, and the line on the right is the maximum ground displacement of 8.3 in. These lines are used for comparison of the spectrum values in Figure 4.32. For very short periods, the spectral acceleration values approach the maximum ground acceleration. For very long periods, the maximum spectral displacements approach the maximum ground displacement.

The maximum displacement, shearing force, and bending moment at each nodal point obtained by probable maximum method are shown in Figures 4.33, 4.34, and 4.35, respectively, for the outer and inner shells. The maximum deflection shape obtained from the time-history analysis and the spectral analysis (with both maximum probable values and maximum absolute values) are plotted and compared in Figure 4.36 for both outer and inner shells, respectively. It can be seen that the values obtained by the probable maximum method are slightly lower than the exact values and the absolute maximum method are slightly higher than the exact values. If the probable maximum method is used to analyze a structure, it may underestimate the response. The absolute maximum method is used to analyze a special structure, such as the containment vessel in nuclear power plant, which needs higher safety factor to resist a strong earthquake.

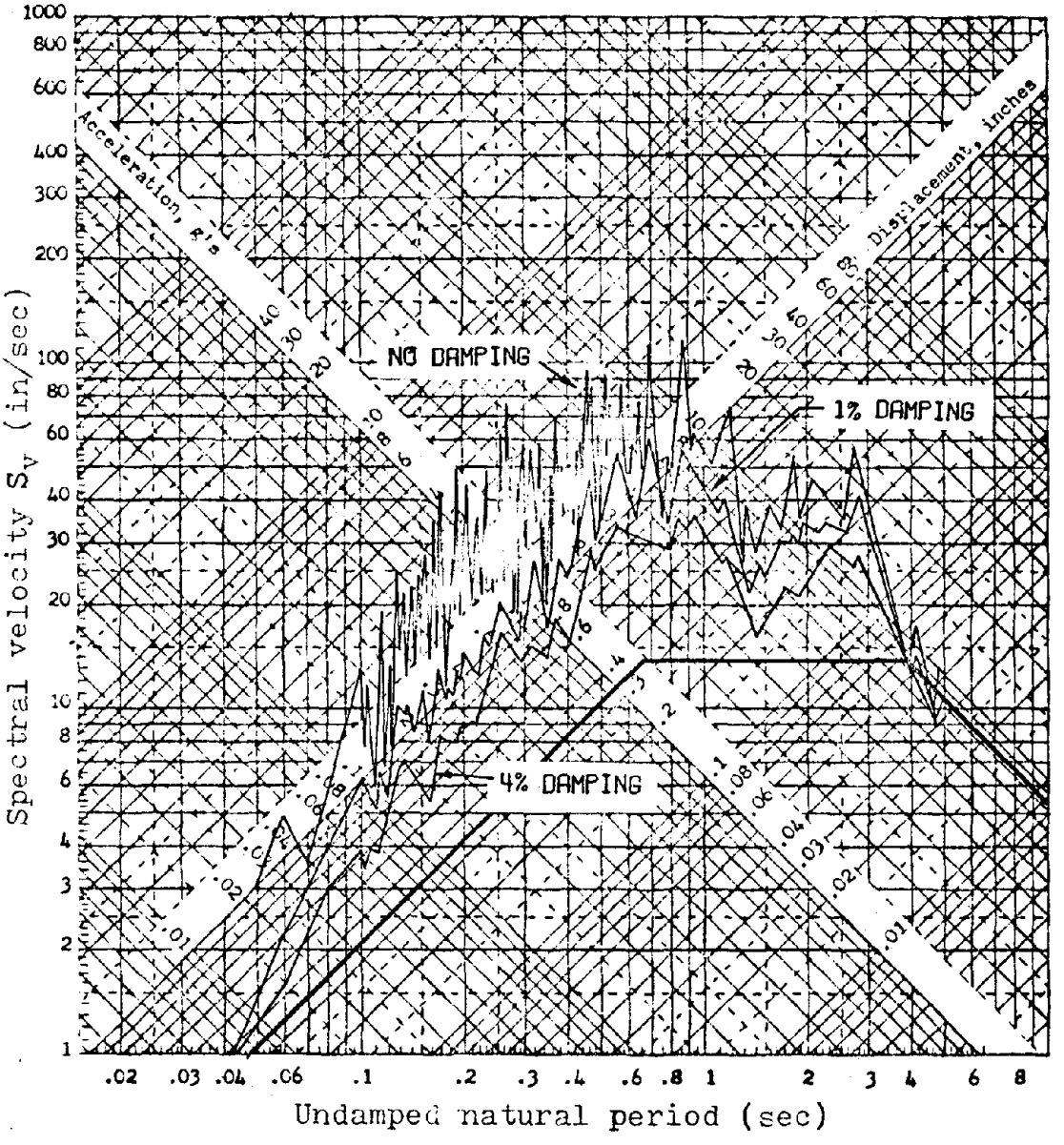

Figure 4.32 Response spectra for elastic systems, 1940 El Centro earthquake (N-S component)

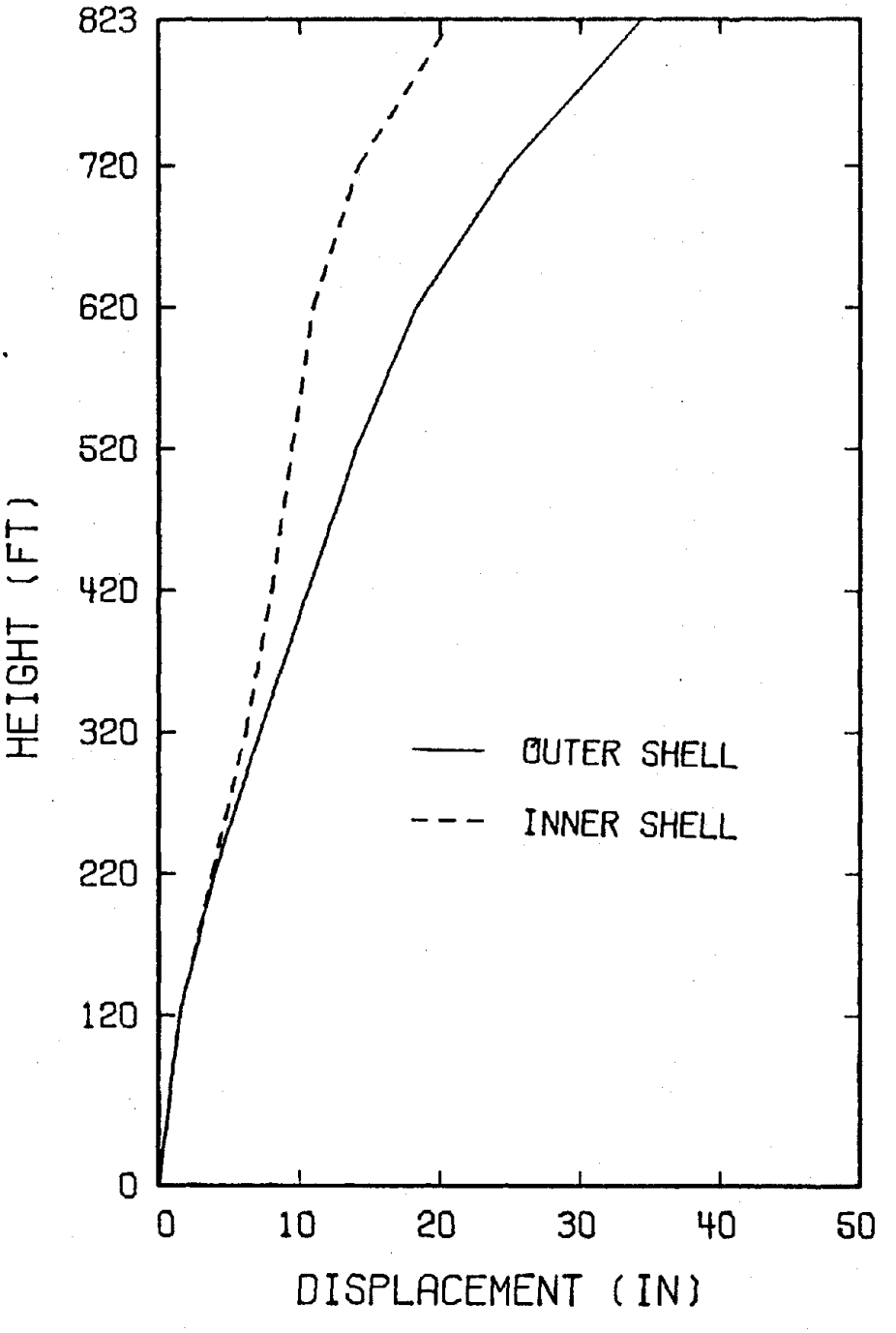

Figure 4.33 Maximum deflection versus height for both shells.

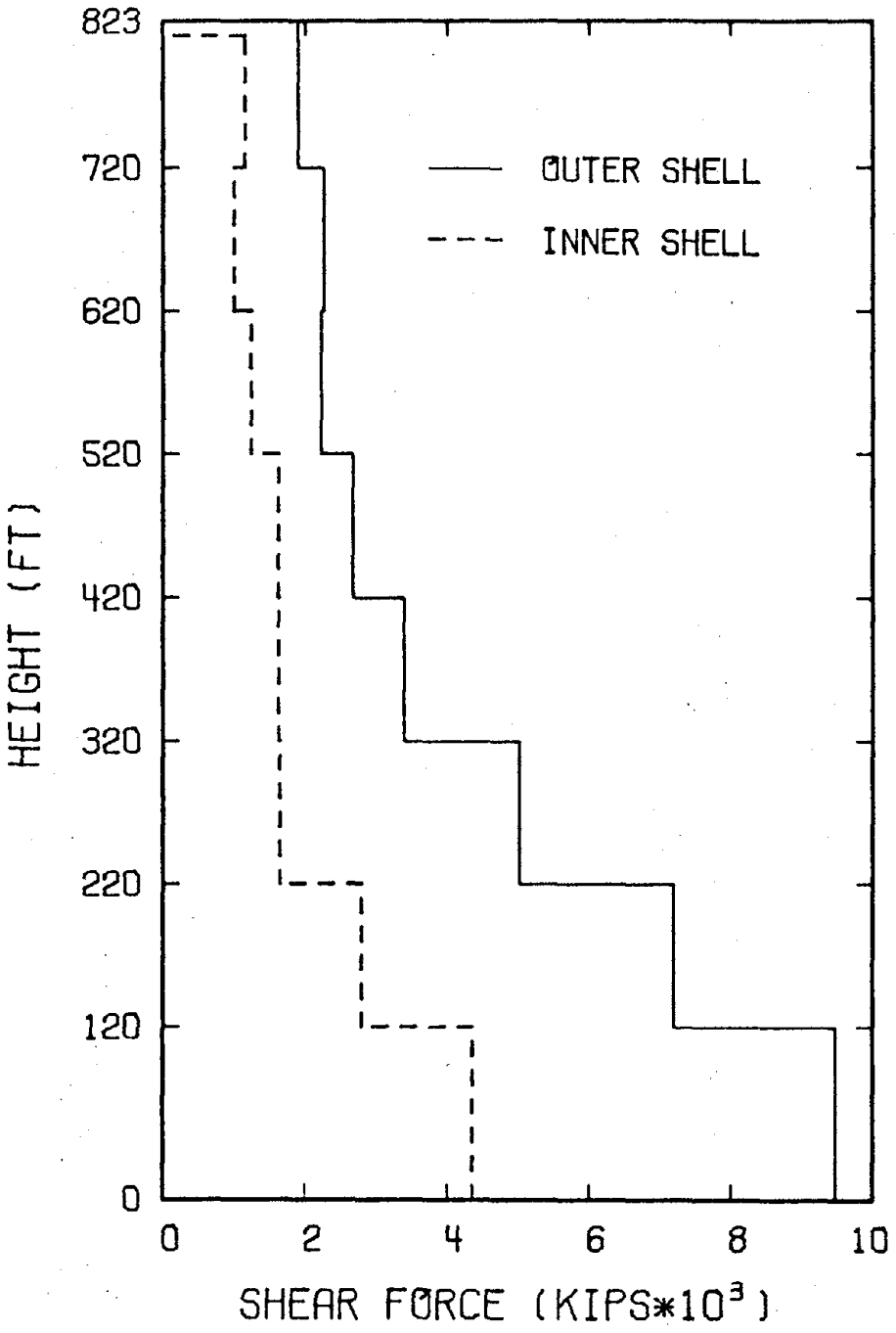

Figure 4.34 Maximum shearing force versus height for both shells.

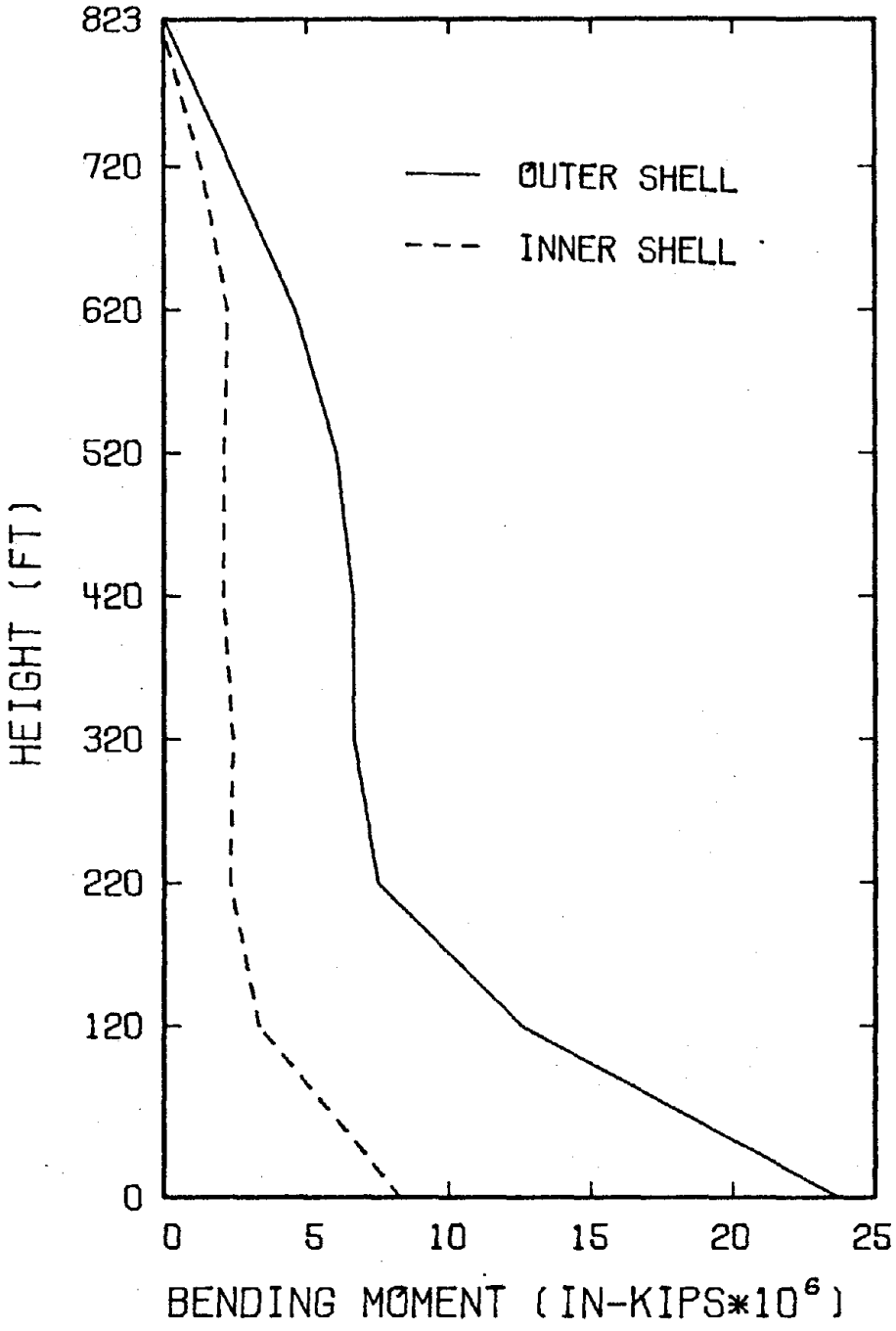

Figure 4.35 Maximum bending moment versus height for both shells.

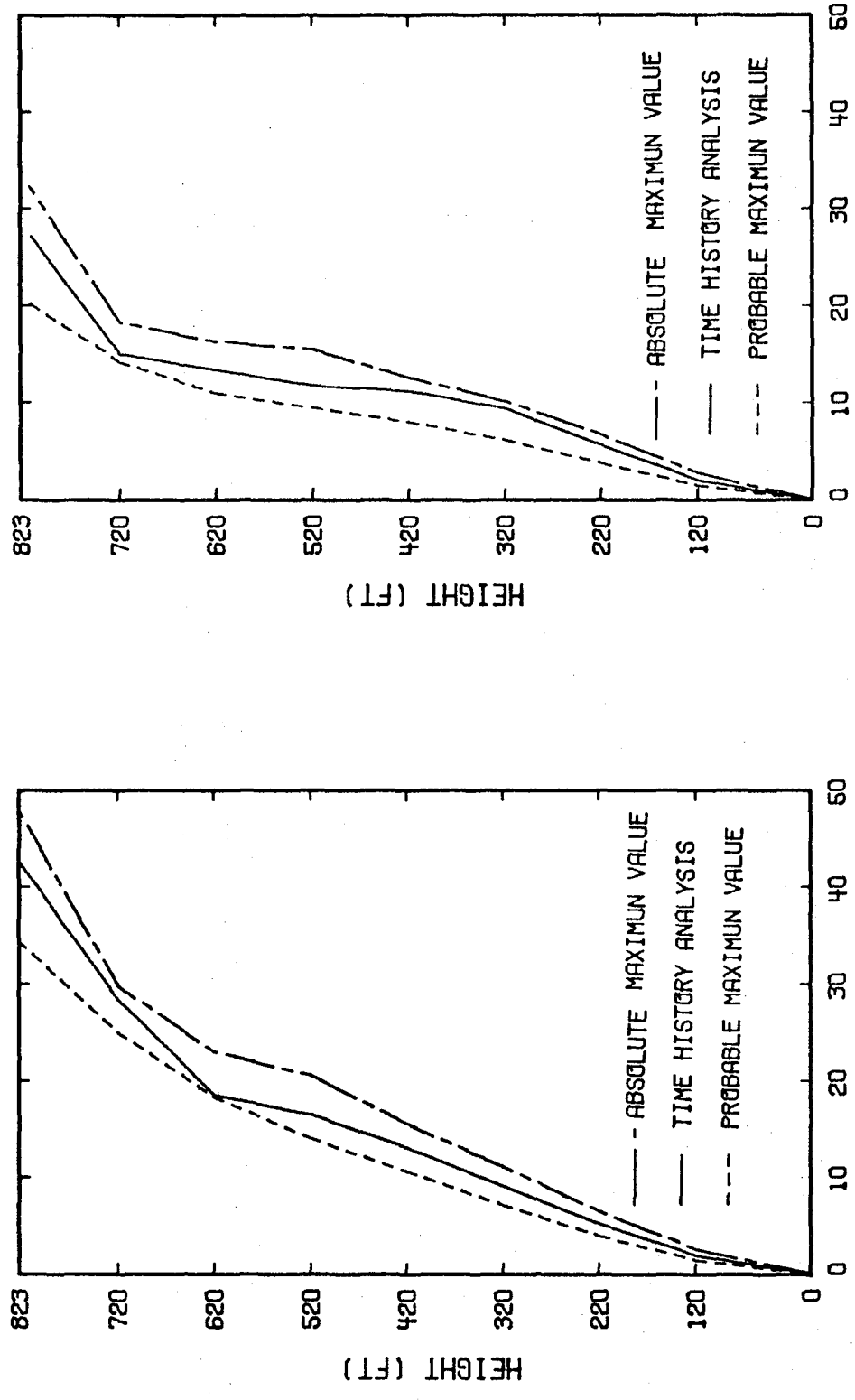

Figure 4.36 Comparison of time history and response spectrum deflections.

4.3. Summary and Conclusions

The south-north and vertical components of the El Centro earthquake are used to perform the time history response analyses of the present chimney. A thorough investigation of many aspects of the elastic dynamic responses of the chimney is carried out. Besides providing the comprehensive information about the elastic response of the chimney, the following conclusions are drawn:

(1) The maximum bending stress in the present chimney may not occur at the section where the maximum bending moment occurred. The most critical sections are at 520 feet above the base for the outer shell and at 620 feet above the base for the inner shell.

(2) With 4 percent of the critical damping, the maximum deflection, shearing force and bending moment are reduced by approximately 50 percent of the corresponding values of the undamped case, respectively. The effect due to the increase in damping beyond this value is, however, no longer pronounced.

(3) The stress distribution in the chimney is dominated by the bending action due to horizontal component of the earthquake. The effect due to vertical component of the earthquake is small.

(4) The cracks developed in the chimney decrease the bending stiffness of the chimney and increase the tensile stresses in the steel. The effect of cracks on the deflection of the chimney is dependent on the relationship between the natural frequencies of the chimney and the frequencies of the ground excitation. Hence, the deflection of the chimney with crack may not necessarily be greater than that of the chimney without

crack.

(5) If the effect of the shear deformation is neglected, the deflection and bending moment of the chimney increase by about 15 percent.

(6) The deflections of the chimney obtained by the probable maximum method are slightly lower than the exact values. The deflections obtained by the absolute maximum method are slightly higher than the exact values.

V. Inelastic Response of a Chimney to Earthquake

5.1 Plastic Bending Analysis of a Beam

In the present study, only the material nonlinearity is considered, i.e., the geometrical properties of the chimney still remain linear. As stated in the second chapter, the material is assumed to be bilinearly elasto-plastic for both tension and compression with the same yield strength as shown in Figure 2.2.

Before performing the plastic bending analysis of the chimney, the formulation and procedure will be evaluated by the example of a simple beam with rectangular cross section. In 1968, Armen et. al (2) presented a finite element formulation and method for the plastic bending analysis of structures. This development is described here and is used in the inelastic analysis of the chimney.

The same beam finite element as shown in Figure 3.1 is redrawn in Figure 5.1. Based on the assumed stress-strain relationship and the Kirchoff's hypothesis (plane sections remain plane after bending), the plastic strain varies linearly through the depth of the cross section. In order to simplify the complexity of the plastic bending analysis of a beam, the distribution of the plastic strain in a beam finite element is assumed to vary linearly along the edges of the element between two adjacent nodes. This assumed distribution can be written as

$$\varepsilon_p = \left(\frac{z-\bar{z}}{h-\bar{z}}\right)\left[\varepsilon_{pi}\left(1 - \frac{x}{\ell}\right) + \varepsilon_{pj}\left(\frac{x}{\ell}\right)\right] \qquad (5.1)$$

where ε_{pi} is the plastic strain at the upper (or lower) surface at node i and ε_{pj} is the same quantity at node j as shown in Figure 5.1. The quantity $\bar{z}$ in Equation (5.1) represents the depth of the elastic-plastic boundary and is also assumed to be a linear function of the coordinate x

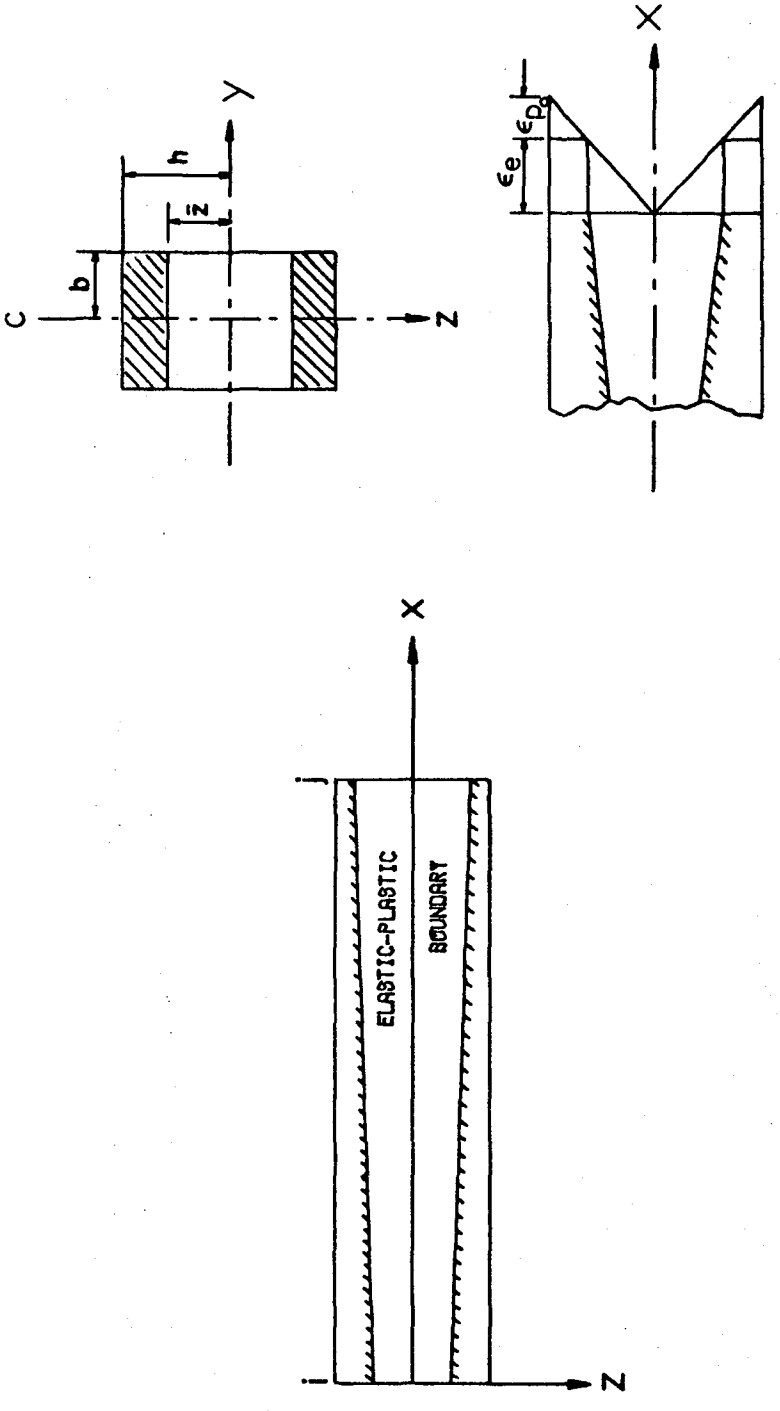

Figure 5.1 Typical elastic-plastic beam element.

$$\bar{z} = (\bar{z}_j - \bar{z}_i)(\frac{x}{\ell}) + \bar{z}_i \tag{5.2}$$

where $\bar{z}_i$ and $\bar{z}_j$ represent the depth of the elastic-plastic boundary at nodes i and j, respectively.

Equation (5.1) can be rewritten as

$$\{\varepsilon_p\} = (\frac{z-\bar{z}}{h-\bar{z}})[1 - \frac{x}{\ell} \ , \ \frac{x}{\ell}] \begin{Bmatrix} \varepsilon_{pi} \\ \varepsilon_{pj} \end{Bmatrix}$$

$$= [B_p]\{\varepsilon_{po}\} \tag{5.3}$$

Since the plastic strain does not have any contribution to the stiffness of the beam, the stiffness matrix can be obtained by substituting Equations (3.4) and (5.3) into the expression for elastic strain energy and applying the Castigliano's theorem.

The elastic strain can be written in terms of the total and plastic strains as

$$\varepsilon_e = \varepsilon - \varepsilon_p \tag{5.4}$$

Substituting Equation (5.4) into (3.5) and excluding terms that are independent of displacements yields

$$U = \frac{1}{2}\iiint_V \varepsilon^T[E]\{\varepsilon\}dv - \iiint_{V_p} \{\varepsilon\}^T[E]\{\varepsilon_p\}dv \tag{5.5}$$

where v_p is the volume of the plastic portion of the element.

Substitution of Equations (3.4) and (5.3) into (5.5) gives

$$U = \frac{1}{2}\{\delta\}^T \iiint_V [B]^T[E][B]dv\{\delta\} - \{\delta\}^T \iiint_{V_p} [B][E][B_p]dv\{\varepsilon_{po}\}$$

or

$$U = \frac{1}{2}\{\delta\}^T[K]\{\delta\} - \{\delta\}^T[K_p]\{\varepsilon_{po}\} \tag{5.6}$$

The matrix $[K_p]$ is the initial strain stiffness matrix and is a function of the depth of the elastic-plastic boundary at each nodal section and must be continuously computer during the course of loading. The initial strain stiffness matrix is given in Appendix.

Deriving Equation (5.6) with respect to nodal displacement $\{\delta\}$ yields

$$\frac{\partial U}{\partial\{\delta\}} = [K]\{\delta\} - [K_p]\{\varepsilon_{po}\} = \{R\} \tag{5.7}$$

where $\{R\}$ is the vector of generalized nodal forces.

Since an incremental solution procedure will be employed, Equation (5.7) is written in incremental form as

$$\{\Delta R\} = [K]\{\Delta\delta\} - [\bar{K}_p]\{\Delta\varepsilon_{po}\} \tag{5.8}$$

where $[\bar{K}_p]$ is the initial strain stiffness matrix for the increment of plastic strain and is different from the initial strain stiffness matrix $[K_p]$ for the total plastic strain $\{\varepsilon_{po}\}$. In the present analysis, ε_{po} is assumed to vary linearly through the thickness from the upper (or lower) surface to the elastic-plastic boundary. This implies a bilinear distribution of $\Delta\varepsilon_{po}$, hence, the initial strain stiffness matrix $[\bar{K}_p]$ obtained from this bilinear distribution may be different from $[K_p]$. In order to avoid having to determine the bilinear distribution $\Delta\varepsilon_{po}$, an incremental form may be used as follows:

$$\{\Delta R\}^i = [K]\{\delta\}^i - \{\Delta q\}^i \tag{5.9}$$

where

$$\{\Delta q\}^i = [K_p]^i \{\epsilon_p\}^i - [K_p]^{i-1} \{\epsilon_p\}^{i-1} \tag{5.10}$$

and superscripts i and i-1 refer to the current and preceding load steps, respectively. The vector $\{\Delta q\}$ is considered as an increment of fictitious load resulting from the initial strain in the element. It is seen from Equation (5.10) that the vector $\{\Delta q\}$ is determined directly from the total plastic strain and is not dependent on the increment of plastic strain.

Equation (5.9) can be written in the following form

$$[K]\{\Delta\delta\}^i = \{\Delta R\}^i + \{\Delta q\}^{i-1} \tag{5.11}$$

The reason to change the superscript of $\{\Delta q\}$ from i to i-1 is that the depth of the elastic-plastic boundary (and the current value of plastic strain) at nodal section can be determined, in general, only from the stress (or strain) distribution computed at the end of the previous load step and is assumed to reamin fixed in the current load step. The value of $\{\Delta q\}$ can only be determined from the results at the end of previous load step and remains constant during the current load step.

Equation (5.11) is formulated for each element used in the modeling of the structure. The resulting equations are then appropriately assembled to form the overall governing matrix equations.

Solution Procedure

The incremental procedures for the plastic bending analysis of a beam of any load step are as follows:

(1) Calculate the increments of generalized displacement by Equation (5.11). The increments of fictitious load in this equation are zero as yielding has not occurred.

(2) Use Equation (3.4) to calculate the increments of total strain at each nodel section.

(3) Obtain the total strain at each nodal section by adding the increments of total strain to that of the previous step.

(4) Determine the plastic strain at each nodal section.

(5) Determine the depths of the elastic-plastic boundaries at each nodal section from the relation of total strain and plastic strain at that nodal section.

(6) Form the initial strain stiffness matrix by Equation (5.6).

(7) Calculate the increments of fictitious load for each element by Equation (5.10).

(8) Repeat (1) to (7) until the end of the loading process is reached.

The above procedure can be expressed simply by the formulations summarized as follows:

$$
\begin{cases}
[K]\{\Delta\delta\}^{i} = \{\Delta R\}^{i} + \{\Delta q\}^{i-1} \\
\{\Delta\epsilon\}^{i} = [B]\{\Delta\delta\}^{i} \\
\{\epsilon\}^{i} = \{\epsilon\}^{i-1} + \{\Delta\epsilon\}^{i} \\
\{\epsilon_p\}^{i} = \{\epsilon\}^{i} - \{\epsilon_e\} \\
\{\Delta q\}^{i} = [K_p]^{i}\{\epsilon_p\}^{i} - [K_p]^{i-1}\{\epsilon_p\}^{i-1}
\end{cases}
$$

Results and Discussion

The preceding formulations and procedures are used to analyze a cantilever beam for which the exact solution is available for comparison. Because of the assumptions that the material has an elastic-ideally plastic behavior and the structure is statically determinate, the depth of the elastic-plastic boundary can be directly related to the applied load.

Figure 5.2a represents a nondimensionalized load versus tip deflection curve for a uniformly loaded cantilever beam with rectangular cross section. Twelve elements are used to model the beam. In this figure, δ_T is the tip deflection, δ^* is the tip deflection at the elastic limit and $\bar{\rho}$ represents the nondimensional load parameter defined as,

$$\bar{\rho} = \frac{P}{P_o} \left(\frac{a}{h}\right)^2$$

where P = applied load intensity

$P_o = 4b\sigma_y$

a = length of the beam element

h = half depth of the beam

b = half width of the beam

The results obtained from the finite element analysis compare quite well with the corresponding results from the exact solution (15), as shown in Figure 5.2a. The collapse load, as determined from the near vertical slope of the load-deflection curve, is approximately 2 percent higher than the exact collapse load which occurs at a value of $\bar{\rho} = 1$.

Figure 5.3 shows the nondimensionalized load versus tip deflection curve for the present chimney (both outer and inner shells) under uniformly distributed load. Eight elements are used in the chimney. For the pipe-type beam, $\bar{\rho} = \frac{P}{P_c}$ and P_c is the maximum ultimate load (or collapse load) at which a fully plastic cross section is developed in the chimney. Because the cross section of the chimney is not uniformly distributed along its height, the value of the nondimensional tip deflection for the outer sehll is higher than that for the inner shell. If the two shells have uniform cross sections, the two curves shown in Figure 5.3 for both shells should coincide. It can be seen from Figures 5.2a and 5.3 that for the present two beam examples the tip deflection near the collapse load is

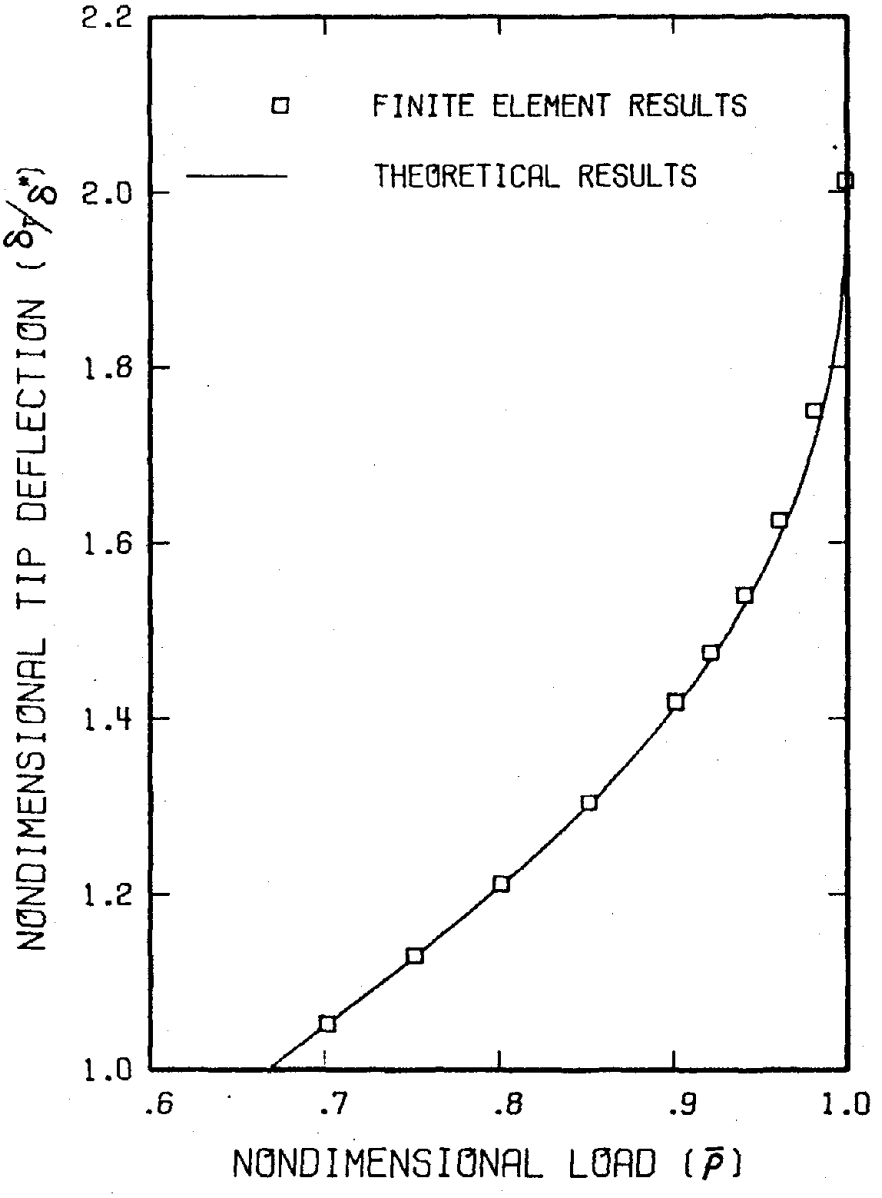

Figure 5.2a Load versus deflection of a cantilevered beam.

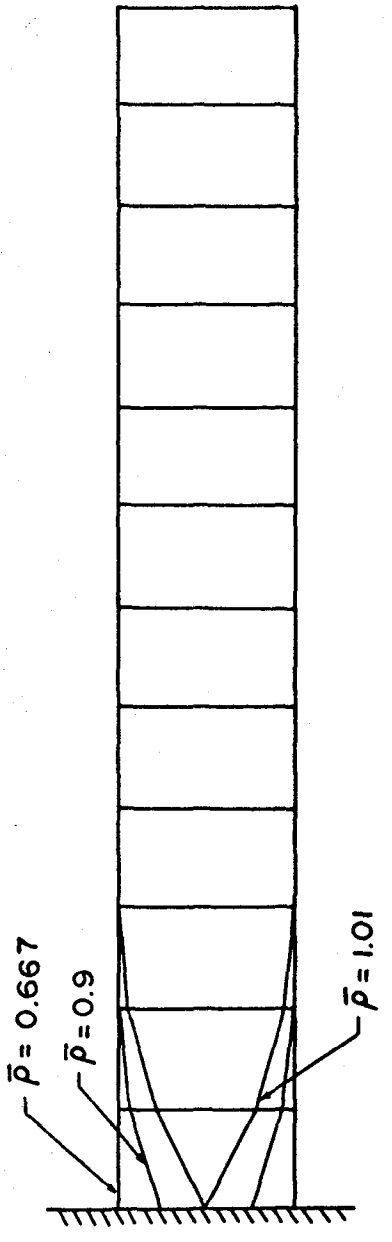

Figure 5.2b Progression of elastic-plastic boundary of a cantilever beam.

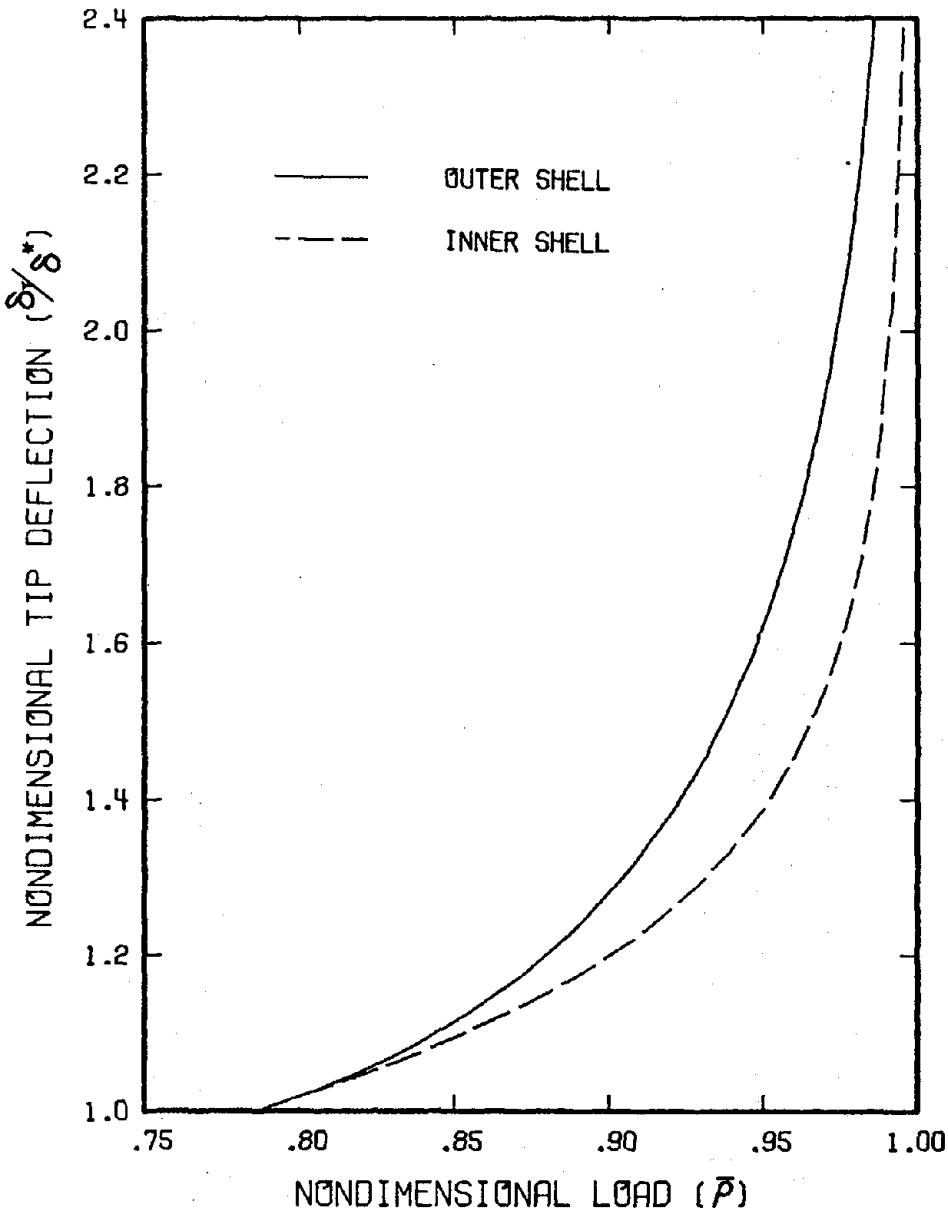

Figure 5.3 Load versus deflection of the outer and inner shells.

about twice the tip deflection at elastic limit.

The progression of the elastic-plastic boundary through the thickness for a rectangular beam is shown in Figure 5.2b. Because of the assumption associated with the plastic strain distribution in the beam element, the neighboring elastic-plastic boundaries at the common nodal section are not continuous. These discontinuities can be reduced by increasing the number of elements used in the beam.

As shown in Figure 5.2b, yielding originates at a load of $\bar{\rho} = 0.667$ at the fixed end of the beam. Plasticity first develops in the outer surface of the beam and propagates towards the neutral axis of the beam. As $\bar{\rho}$ increases from 0.667 to 1.0, the plastic region gradually spreads from the fixed end to the free end. When $\bar{\rho}$ equals to 1.0, the fixed end section of the beam becomes fully plastic and the beam can no longer carry any additional load.

5.2 Cyclic Loading Analysis of a Cantilever Beam

The simplest case, a beam with rectangular cross section subjected to cyclic loading, is studied first in detail. The same method is then applied to analyze the chimney.

(i) Moment-Curvature Relationship of a Beam with Rectangular Cross Section

Figure 5.4 indicates a beam with rectangular cross section subjected to a pure bending moment M. It is assumed that the moment is first increased from zero to a value of M' and then decreased. If M' is less than the maximum elastic moment M_e, the stresses will be everywhere elastic during loading and unloading. The moment curvature relationship for both loading and unloading processes can be easily expressed as

$$M = \frac{4}{3} EbH^3R$$

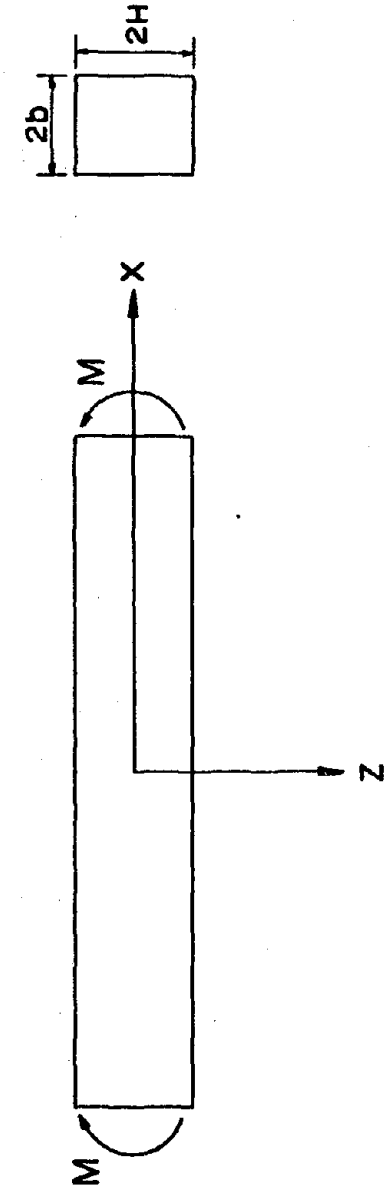

Figure 5.4 Beam under pure bending.

or in the following dimensionless form

$$\bar{m} = \frac{2}{3}\rho$$

where $\bar{m} = \frac{M}{M_p}$, $\rho = \frac{R}{R_e}$ and b = half width of the beam, H = half depth of the beam, R = curvature of the middle surface, R_e = curvature of the middle surface at elastic limit, and M_p = fully plastic moment.

When M is equal to M_e, i.e., the stresses at the extreme outer fibers of the beam just reach the elastic limit, the moment and curvature are given by

$$\bar{m}_e = \frac{2}{3} \qquad \rho_e = 1$$

(1) If M is further increased to a value M_1 which is greater than M_e, the stress distribution is shown in Figure 5.5a. In the elastic zone $(0 \le z \le \frac{1}{\rho_1})$ the dimensionless bending stress varies linearly with z,

$$s_1 = \rho z$$

In the plastic zone $(\frac{1}{\rho_1} \le z \le 1)$, the dimensionless bending stress is constant along z with magnitude equal to unity.

$$s_1 = 1$$

where z = Z/H. Integrating the stress over the cross section, the moment curvature relationship is obtained as follows:

$$\bar{m} = 2\int_A szdz = 2\int_0^{1/\rho_1} \rho_1 z^2 dz + 2\int_{1/\rho_1}^{1} zdz$$

$$= 1 - \frac{1}{3\rho_1^2}$$

The height of elastic-plastic boundary is then given by

$$\bar{z}_1 = \frac{1}{\rho_1}$$

(2) A negative moment is then superimposed on the distribution of stress given in Figure 5.5(a). All the quantities related to this negative moment are designated by a prime. The resulting net moment is defined as M_2. Based on the magnitude of M_2, the stress distribution can be divided into two cases.

(a) If the net value of the bending moment M_2 is less than M_1 but sufficiently large such that the beam is still in elasto-plastic behavior, the resultant stress distribution is shown in Figure 5.5b. The resulting dimensionless stresses are defined as,

$$s_2 = s_1 - s' = (\rho_1 - \rho')z \qquad 0 \le z \le \frac{1}{\rho_1}$$

$$s_2 = 1 - \rho' z \qquad \frac{1}{\rho_1} \le z \le \frac{2}{\rho'}$$

$$s_2 = -1 \qquad \frac{2}{\rho'} \le z \le 1$$

The moment curvature relationship corresponding to the above equation is

$$\bar{m}_2 = 2\left[\int_0^{1/\rho_1} (\rho_1 - \rho')z^2 dz + \int_{1/\rho_1}^{2/\rho'} (1 - \rho' z)z dz + \int_{2/\rho'}^{1} -z dz \right]$$

$$= -1 + \frac{8}{3\rho'^2} - \frac{1}{3\rho_1^2}$$

$$= \frac{1}{3}\left[-3 - \frac{1}{\rho_1^2} + \frac{8}{(\rho_1 - \rho_2)^2}\right]$$

The location of the elastic-plastic boundary is given by

$$\bar{z}_2 = \frac{2}{\rho'}$$

which is greater than $\bar{z}_1$.

(b) If the net value of the bending moment M_2 is greater than or equal to M_1, the stress distribution and the moment curvature relationship will return to case (1), except the signs of all quantities are changed.

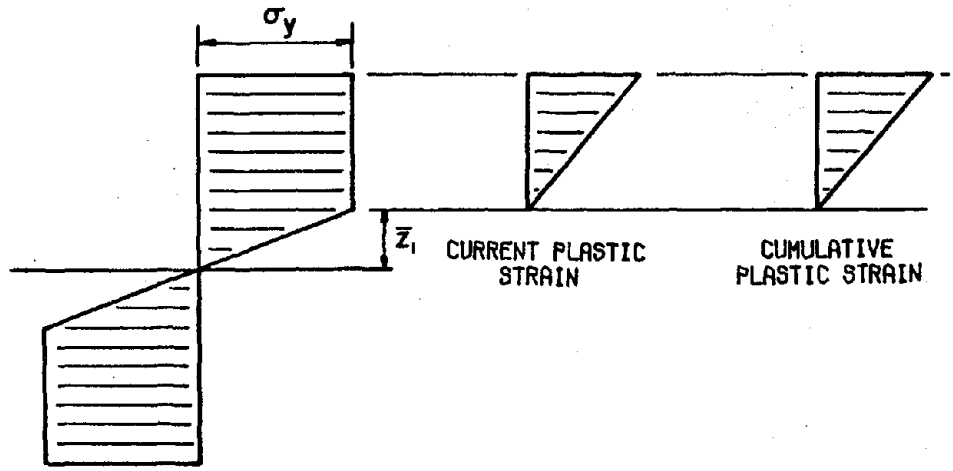

(a)

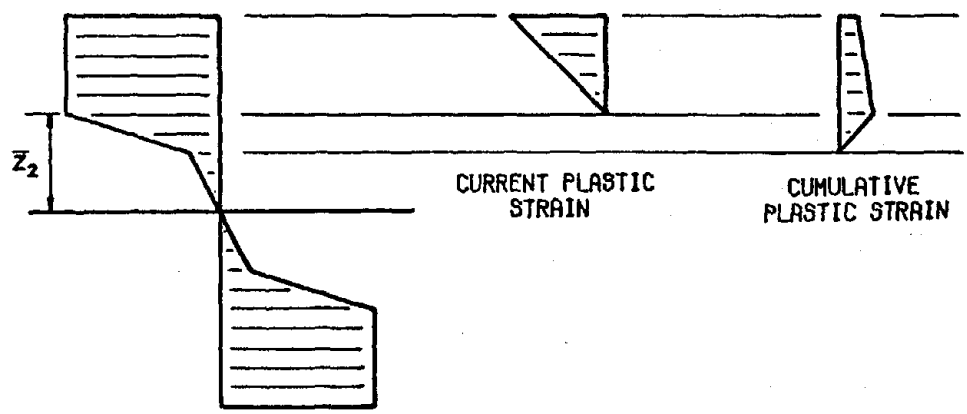

(b)

Figure 5.5 Stress and plastic strain distributions in a rectangular beam.

(3) A positive moment is subsequently superimposed on case (2)a. All the quantities related to this positive moment are designated by double primes. The resulting net moment is defined as M_3. Based on the magnitude of M_3, the stress distribution can be described in the following two cases.

(a) If the net value of the bending moment M_3 is less than M_1, either greater or not greater than M_2, the stress distribution shown in Figure 5.5c is

$$s_3 = s_1 - s' + s'' = (\rho_1 - \rho' + \rho'')z \qquad 0 \le z \le \frac{1}{\rho_1}$$

$$s_3 = 1 - \rho' z + \rho'' z \qquad \frac{1}{\rho_1} \le z \le \frac{2}{\rho'}$$

$$s_3 = -1 + \rho'' z \qquad \frac{2}{\rho'} \le z \le \frac{2}{\rho''}$$

$$s_3 = 1 \qquad \frac{2}{\rho''} \le z \le 1$$

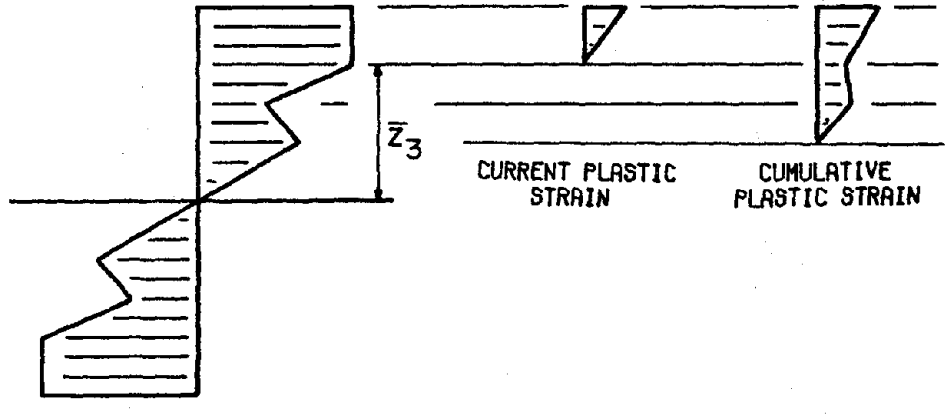

(c)

Figure 5.5 (continue)

The moment curvature relationship corresponding to the above stress distribution is

$$\bar{m}_3 = 1 - \frac{8}{3\rho''^2} + \frac{8}{3\rho'^2} - \frac{1}{3\rho^2}$$

and the location of the elastic-plastic boundary is given by

$$\bar{z}_3 = \frac{2}{\rho''}$$

which is always greater than $\bar{z}_2$.

(b) If the bending moment M_3 is greater than M_1, the stress distribution and the moment curvature relationship will again be the same as in case (1).

From above analyses the following conclusion can be made. The beam is subjected to a sequence of cyclic moments with the following conditions,

1. $M_1 > 0$, is first applied to the beam
2. $|M_2| < |M_1|$
3. $M_1 > M_3 > \cdots > M_i$
4. $|M_2| > |M_4| > \cdots > |M_{i+1}|$
5. the sign of the ith moment is $(-1)^{i-1}$, i.e., this sequence of moments are alternatively in sign.

The stress distribution at the instant of ith bending moment can be obtained as follows

$$s_i = (\rho_1 - \rho' + \rho'' - \rho''' + \cdots + (-1)^{i-1}\rho^{(i-1)})z \qquad 0 \le z \le \frac{1}{\rho_1}$$

$$s_i = 1 - \rho' z + \rho'' z - \rho''' z + \cdots + (-1)^{i-1}\rho^{(i-1)}z \qquad \frac{1}{\rho_1} \le z \le \frac{2}{\rho'}$$

$$\vdots$$

$$s_i = (-1)^i + (-1)^{i-1}\rho^{(i-1)}z \qquad \frac{2}{\rho^{(i-2)}} \le z \le \frac{2}{\rho^{(i-1)}}$$

$$s_i = (-1)^{i-1} \qquad \frac{2}{\rho^{(i-1)}} \le z \le 1$$

where the quantity $\rho^{(i-1)}$ denotes the superimposed curvature at current case. The moment curvature relationship corresponding to the above stress distribution is given by

$$\bar{m}_i = \int_A s_i z dz$$

$$= 1 + \frac{(-1)^i}{3\rho_i^2} + \frac{8}{3} \sum_{n=1}^{i-1} \frac{(-1)^n}{(\rho^{(n)})^2}$$

and the location of the elastic-plastic boundary at ith bending moment is

$$\bar{z}_i = \frac{2}{\rho^{(i-1)}}$$

(ii) Plastic Strain Distribution

The current plastic and cumulative plastic strains corresponding to the stress distribution at each stage are shown in the same figures of the stress distribution, Figure 5.5 a - c. In Figure 5.5a, for the first half-cycle, both current plastic and cumulative plastic strains are linear and have the same distribution across the thickness. For the following cycles, as shown in Figures 5.5b - 5.5c, the cumulative plastic strain at each stage is obtained by superimposing the current plastic strain to the preceding cumulative plastic strain. Therefore, the cumulative plastic strains at these stages are no longer linearly distributed and the plastic strains at the elastic-plastic boundary are no longer zero. In the plastic bending analysis it has been assumed that the plastic strain distribution varies linearly through the thickness from some value at the extreme outer fibers to zero at the elastic-plastic boundary. This assumption is used in the formation of the initial strain stiffness matrix. The same method used in the plastic bending analysis is also employed for the present cyclic loading analysis.

Therefore, the same assumption for plastic strain distribution must hold for the cyclic loading case. Fortunately, for cyclic loading analysis, the plastic strain which is always linear at each stage. The reasons for using the current plastic strain instead of using the cumulative plastic strain are described as follows.

Let the unloading and reloading process from case (1) to case (2) be reconsidered. From the process of Figures 5.6a to 5.6b, the beam is assumed to unload elastically and the total decreased strain is considered as elastic strain. That is, the current plastic strain is not produced or it equals to zero. In this case, the second term in Equation (5.8) vanishes although the cumulative plastic strain still exists at this stage. In Figure 5.6c, the area above the elastic-plastic boundary is in the plastic range and can not take any additional stress. However, the area below the elastic-plastic boundary is still in the elastic range and any additional load increment is taken by this portion. From the stage of Figure 5.5b to Figure 5.5c, the current strain and stress increments for the entire cross section are shown in Figure 5.6d. The shaded area for the strain in Figure 5.6d represents the current plastic strain which is the same as that shown in Figure 5.6c. The remaining area for the strain in Figure 5.6d represents the elastic strain increment which is proportional to the elastic stress increment as shown in the same figure. Hence, in Equation (5.10), the plastic strain for the (i-1)th step is zero (as shown in Figure 5.6b) and for the ith step is the current plastic strain (as shown in Figure 5.6c).

(iii) Moment Curvature Relationship of a Pipe-type Beam

The stress distribution over the cross section at any stage for a pipe-type beam is the same as that for a rectangular beam. The current plastic and the cumulative plastic strain distributions for a pipe-type beam are

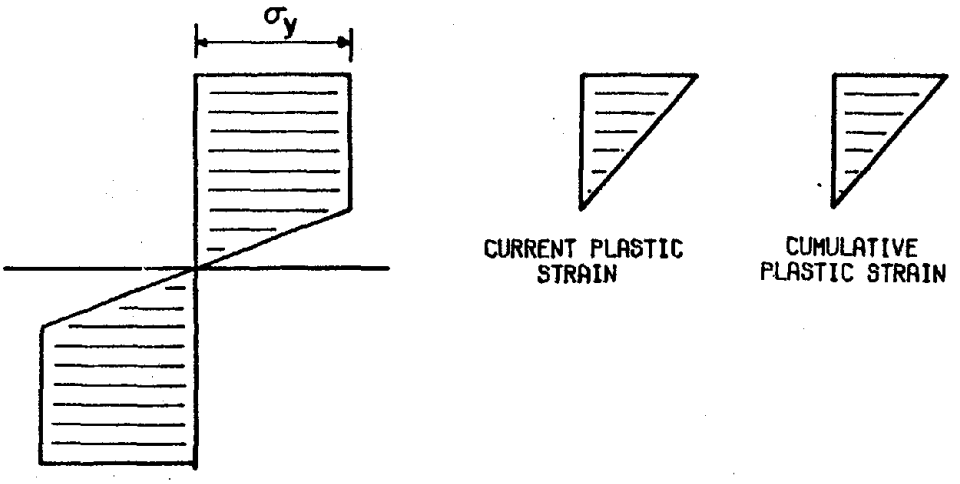

(a)

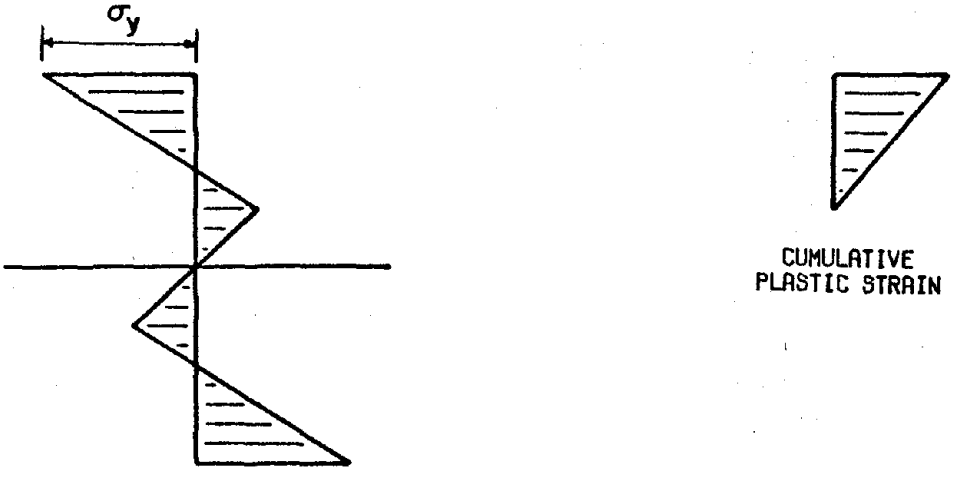

(b)

Figure 5.6 Stress and plastic strain distributions in a rectangular beam.

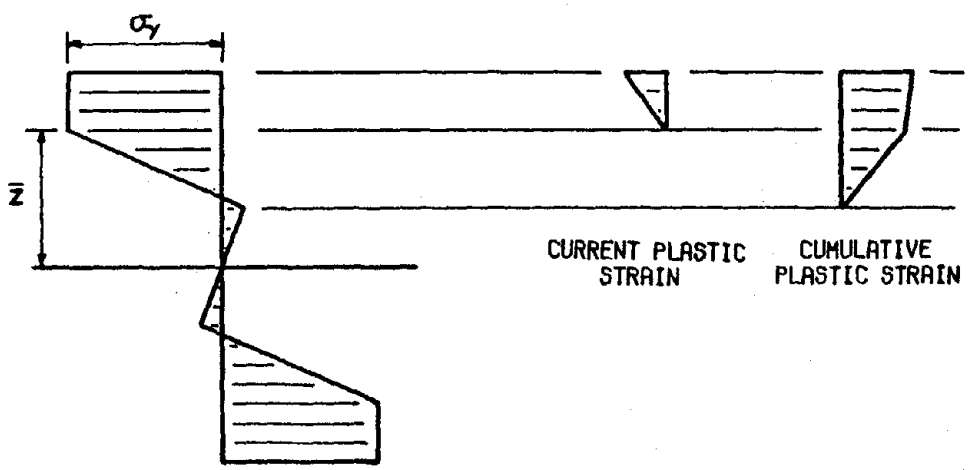

(c)

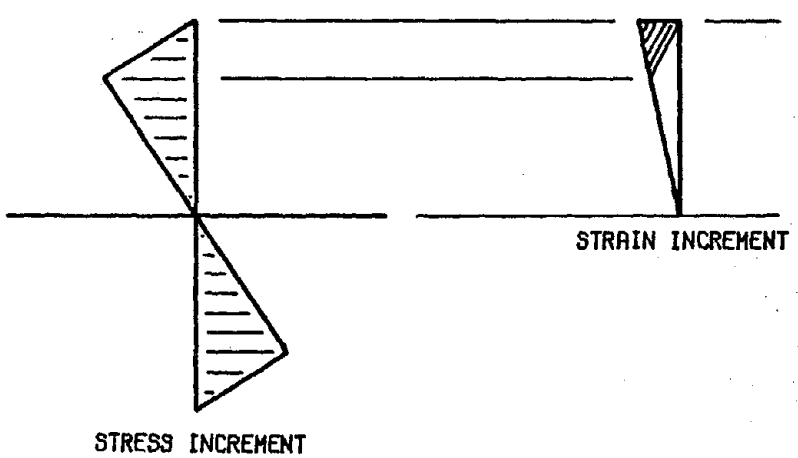

(d)

Figure 5.6 (continue)

also the same as that for a rectangular beam. The only difference between the two kinds of cross section lies in the formula for the moment and curvature relationship.

Figure 5.7 shows a pipe-type beam cross section with outer and inner radius r_o and r_i, respectively. In the present study, the ratio of the thickness $\bar{t}$ to the mean radius r is very small (about 0.02), hence, it is reasonable to assume that the plastic zone (shaded area in Figure 5.7) is bounded by the radius and not by a line parallel to the neutral axis, i.e., the plastic zone is increased circumferentially.

For the stress distribution shown in Figure 5.7. the corresponding moment can be obtained as

$$M_1 = 4 \int_0^{\phi_1} \bar{t} r^2 \sigma_y \frac{\sin^2 \theta}{\sin \phi_1} d\theta + 4 \int_{\phi_1}^{\frac{\pi}{2}} \bar{t} r^2 \sigma_y \sin \theta \, d\theta$$

$$= 4\bar{t} r^2 \sigma_y \left[\frac{\cos \phi_1}{2} + \frac{\phi_1}{2 \sin \phi_1}\right]$$

The location of the elastic-plastic boundary is given by

$$\bar{z}_1 = r \sin \phi_1$$

For the pipe-type beam subjected to a sequence of moments with the same conditions as described in the previous section for the rectangular beam, the relationship between the moment and the angle , which defines the elastic-plastic boundary, can be expressed in general form as

$$M_i = 4\bar{t} r^2 \sigma_y \left[\frac{\phi_1}{2 \sin \phi_1} + \frac{\cos \phi_1}{2} - \sum_{n=2}^{i} (-1)^n \left(\frac{\phi_n}{\sin \phi_n} + \cos \phi_n\right)\right] \quad (5.12)$$

where the integer i denotes the cyclic loading step number. The location of the elastic-plastic boundary is given by

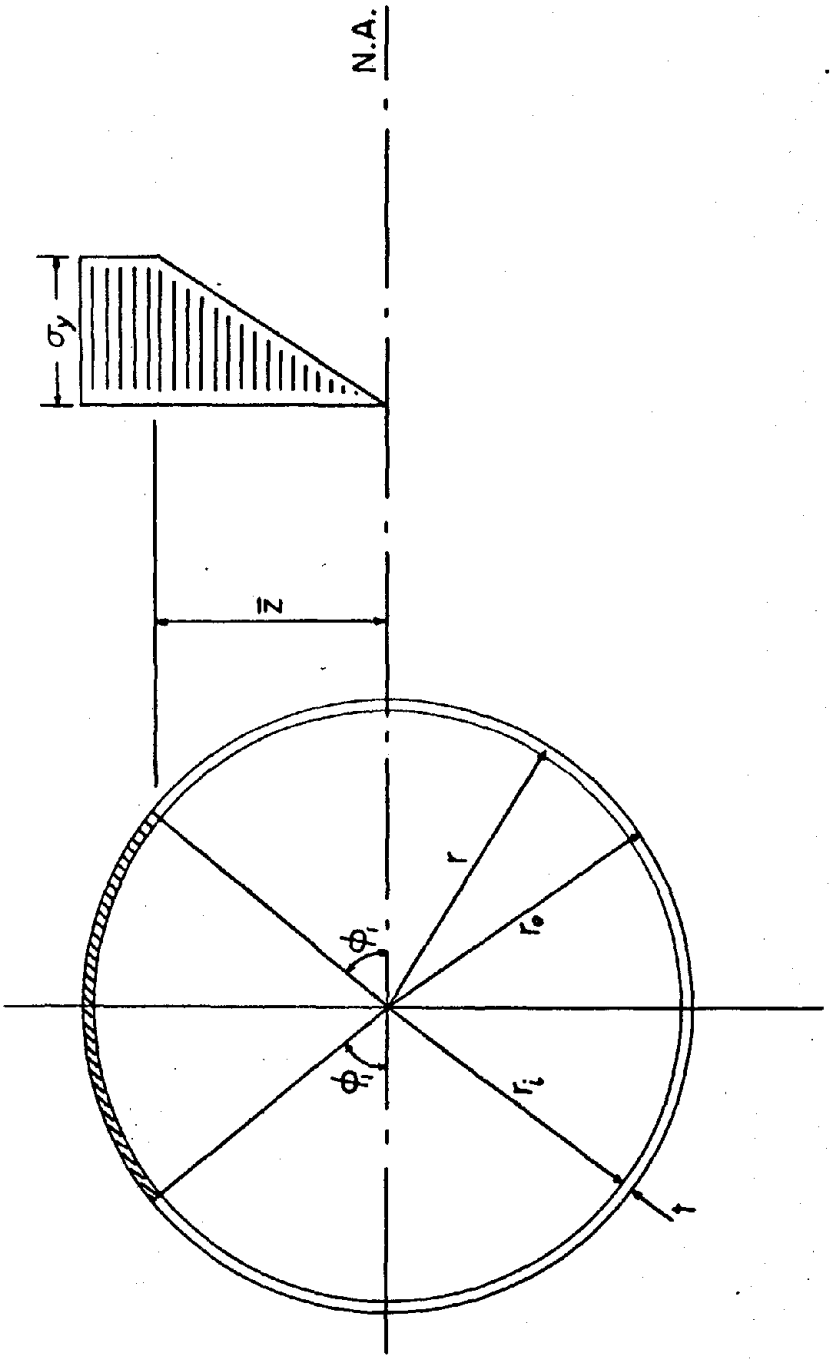

Figure 5.7 Stress distributions in a pipe-type beam.

$$\bar{z}_i = r \sin \phi_i \tag{5.13}$$

The corresponding curvature is given by

$$cur_i = \frac{\varepsilon_e}{r} \left[\frac{1}{\sin \phi_1} - z \sum_{n=2}^{i} \frac{(-1)^n}{\sin \phi_n} \right] \tag{5.14}$$

Figure 5.8 shows a moment curvature diagram for a pipe-type cross section. The circled numbers 1, 2, 3, 4, 5, and 6 in this figure correspond to the loading step number i as defined in equations (5.12) and (5.14). The sequence of moments applied to this beam matches the conditions mentioned earlier. When M_6 reaches point A as shown in the figure, it is equal to M_4. If the moment further decreases, the stress distributions and the curvatures are then obtained by using equations corresponding to M_4.

For a pipe-type section, the maximum elastic moment is equal to $\pi/4$ of the fully plastic moment, so that the elastic range for unloading is equal to $\pi/2$ of the fully plastic moment. The moment curvature curve for the rectangular section or other symmetric section will be similar to Figure 5.8 and the elastic range for unloading is always equal to twice the maximum elastic moment.

5.3 Inelastic Response of the Chimney to Earthquake by Direct Integration Method

In the elastic-plastic dynamic response analysis of a beam structure, the sectional properties change with time. The matrix equations of motion can be solved by a step-by-step numerical integration procedure. Since the stiffness matrix has to be reformed and computed at every time step, such procedure is extremely time-consuming.

In this study, the procedure is simplified such that the stiffness

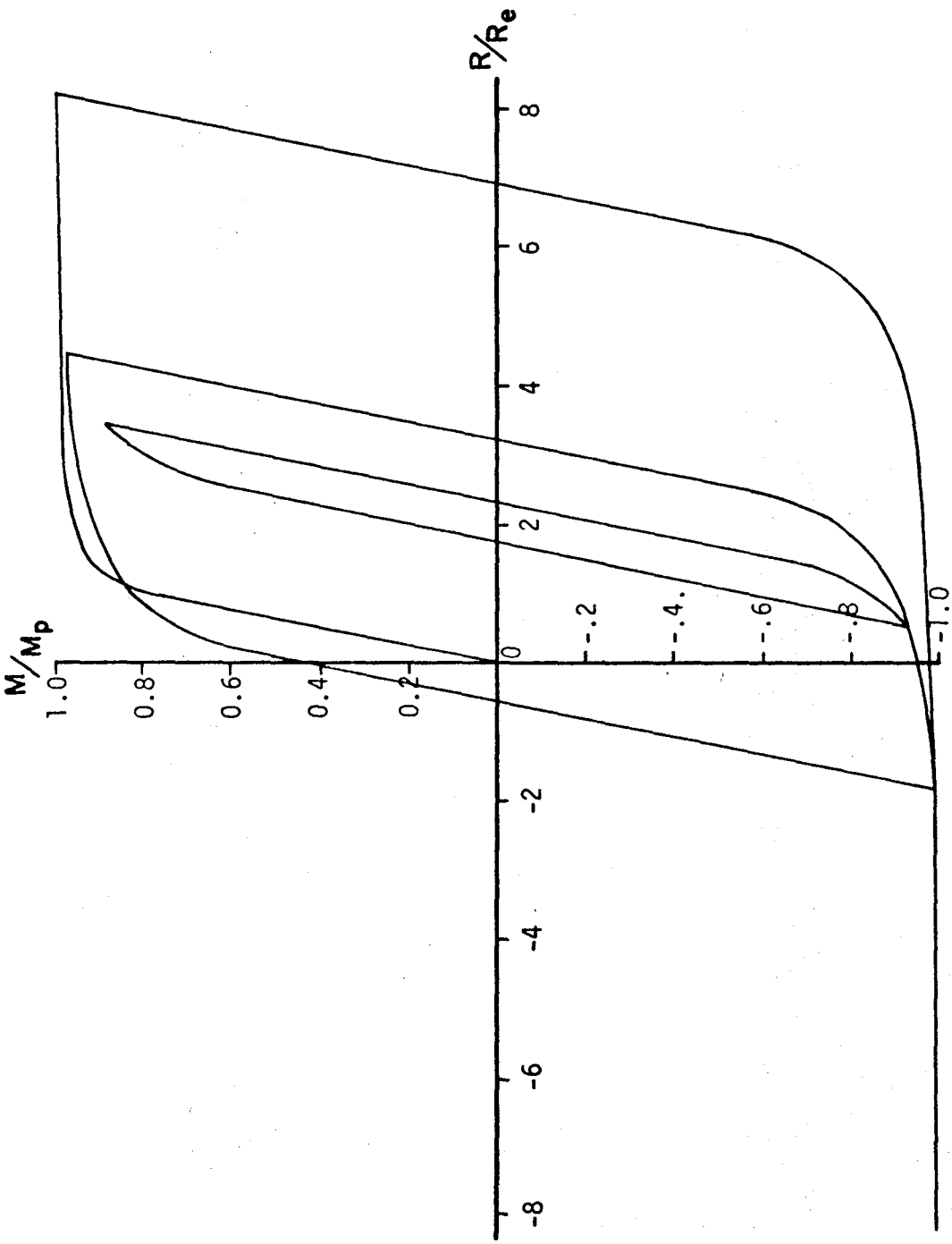

Figure 5.8 Moment-curvature relation for unloading and reloading of a pipe-type beam.

matrix is composed of two parts at every time step. One part is the basic stiffness matrix which accounts for the elastic portion of the structure whereas the other part is formulated as a vector of fictitious loads which accounts for the plastic portion of the structure.

Incremental Form of Equations of Motion

The equilibrium equation for the dynamic forces at the nodal sections of a finite element system at a time t can be written as

$$\{F\}_t^i + \{F\}_t^d + \{F\}_t^e = \{R\}_t \tag{5.15}$$

where

$\{F\}_t^i$ = inertia force vector

$\{F\}_t^d$ = damping force vector

$\{F\}_t^e$ = internal resisting force vector

$\{R\}_t$ = vector of externally applied forces

At time $t+\Delta t$, Equation (5.15) can be written in incremental form as

$$(\{F\}_t^i + \{\Delta F\}_t^i) + (\{F\}_t^d + \{\Delta F\}_t^d) + (\{F\}_t^e + \{\Delta F\}_t^e) = \{R\}_{t+\Delta t} \tag{5.16}$$

The force changes over the time interval Δt are assumed to be given by

$$\{\Delta F\}_t^i = [M]_t\{\Delta\ddot{y}\}_t \qquad \{\Delta F\}_t^d = [C]_t\{\Delta\dot{y}\}_t$$

$$\{\Delta F\}_t^e = [K_t]_t\{\Delta y\} \tag{5.17}$$

where $[M]_t$, $[C]_t$, and $[K_t]_t$ are the mass, damping and tangent stiffness

matrices at time t; $\{\Delta\ddot{y}\}_t$, $\{\Delta\dot{y}\}_t$ and $\{\Delta y\}_t$ are the vectors of changes in the accelerations, velocities and displacements during the time increment. In the present case, the mass and damping are constant. Only the stiffness is nonlinear. Equation (5.13) can thus be written as

$$[M]\{\Delta\ddot{y}\}_t + [C]\{\Delta\dot{y}\}_t + [K_t]_t\{\Delta y\}_t =$$

$$\{R\}_{t+\Delta t} - [M]\{\ddot{y}\}_t - [C]\{\dot{y}\}_t - [K_t]_t\{y\}_t \qquad (5.18)$$

where the force vectors $[M]\{\ddot{y}\}_t$, $[C]\{\dot{y}\}_t$, and $[K_t]_t\{y\}_t$ are evaluated at time t and become the known values for the time step to $t+\Delta t$. Therefore, Equation (5.18) can be solved for $\{\Delta y\}_t$ which in turn gives $\{\Delta\dot{y}\}_t$ and $\{\Delta\ddot{y}\}_t$.

The difference between the elastic stiffness matrix and the tangent stiffness matrix is denoted as $[\Delta K]$ and can be expressed as

$$[K_e] - [K_t] = [\Delta K]$$

Hence, the internal resisting force at time t can be divided into the terms as

$$[K_t]\{y\}_t = ([K_e] - [\Delta K]_t)\{y\}_t = [K_e]\{y\}_t - [\Delta K]_t\{y\}_t \qquad (5.19)$$

or in incremental form

$$[K_t]\{\Delta y\}_t = [K_e]\{\Delta y\}_t - [\Delta K]_t\{\Delta y\}_t \qquad (5.20)$$

The terms $[\Delta K]_t\{y\}_t$ and $[\Delta K]\{\Delta y\}_t$ in the above equations are referred to as fictitious loads and denoted by $\{q\}$ and $\{\Delta q\}$, respectively.

Substituting Equations (5.19) and (5.20) into Equation (5.18), it becomes

$$[M]\{\Delta\ddot{y}\}_t + [C]\{\Delta\dot{y}\}_t + [K_e]\{\Delta y\}_t = \{R\}_{t+\Delta t}$$

$$[M]\{\ddot{y}\}_t - [C]\{\dot{y}\}_t - [K_e]\{y\}_t + \{q\}_t + \{\Delta q\}_{t+\Delta t} \tag{5.21}$$

It should be noted that the relations in Equation (5.17) are only approximations. But the residual force $\{R\}^r_{t+\Delta t}$, given by

$$\{R\}^r_{t+\Delta t} = \{R\}_{t+\Delta t} - [M]\{\ddot{y}\}_{t+\Delta t} - [C]\{\dot{y}\}_{t+\Delta t} - [K_t]\{y\}_{t+\Delta t}$$

is a measure of how well equilibrium is satisfied at time $t+\Delta t$. In order to satisfy equilibrium to a certain limit at the end of each time step, it may be necessary to use iteration.

Solution Procedures of Equations

In this section the Wilson θ-method (3,21,22) is employed for solving the equations of motion. Let $\{\ddot{y}\}_t$, $\{\dot{y}\}_t$ and $\{y\}_t$ be known vectors. To obtain the solution at time $t+\Delta t$, it is assumed that the acceleration is linear over the time interval $\tau = \theta\Delta t$, where $\theta \geq 1.0$. Hence, the quantities at time $t+\tau$ will be

$$\{\dot{y}\}_{t+\tau} = \{\dot{y}\}_t + \frac{\tau}{2}(\{\ddot{y}\}_{t+\tau} + \{\ddot{y}\}_t)$$

$$\{y\}_{t+\tau} = \{y\}_t + \tau\{\dot{y}\}_t + \frac{\tau^2}{6}(\{\ddot{y}\}_{t+\tau} + 2\{\ddot{y}\}_t)$$

which gives

$$\{\ddot{y}\}_{t+\tau} = \frac{6}{\tau}(\{y\}_{t+\tau} - \{y\}_t) - \frac{6}{\tau}\{y\}_t - 2\{\ddot{y}\}_t$$

and (5.22)

$$\{\dot{y}\}_{t+\tau} = \frac{3}{\tau}(\{y\}_{t+\tau} - \{y\}_t) - 2\{y\}_t - \frac{\tau}{2}\{\ddot{y}\}_t$$

The equations of motion, Equation (5.21), shall be satisfied at time $t+\tau$; therefore

$$[M]\{\Delta\ddot{y}\}_t + [C]\{\Delta\dot{y}\}_t + [K_e]\{\Delta y\}_t =$$

$$\{\tilde{R}\}_{t+\tau} - [M]\{\ddot{y}\}_t - [C]\{\dot{y}\}_t - [K_e]\{y\}_t + \{q\}_t + \{\Delta q\}_{t+\Delta t}$$

where $\{\tilde{R}\}_{t+\tau}$ is a projected load equal to $\{R\}_t + \theta(\{R\}_{t+\Delta t} - \{R\}_t)$ and

$$\{\Delta\ddot{y}\}_t = \{\ddot{y}\}_{t+\tau} - \{\ddot{y}\}_t$$

$$\{\Delta\dot{y}\}_t = \{\dot{y}\}_{t+\tau} - \{\dot{y}\}_t$$

$$\{\Delta y\}_t = \{y\}_{t+\tau} - \{y\}_t$$

With $\{y\}_{t+\tau}$ known the accelerations and velocities at time $t+\tau$ are obtained using Equation (5.22).

At time $t+\Delta t$, the desired accelerations, velocities and displacements are given by the linear acceleration assumption:

$$\{\ddot{y}\}_{t+\Delta t} = (1 - \frac{1}{\theta})\{\ddot{y}\}_t + \frac{1}{\theta}\{\ddot{y}\}_{t+\tau}$$

$$\{\dot{y}\}_{t+\Delta t} = \{\dot{y}\}_t + \frac{\Delta t}{2}(\{\ddot{y}\}_t + \{\ddot{y}\}_{t+\Delta t})$$

$$\{y\}_{t+\Delta t} = \{y\}_t + \Delta t\{\dot{y}\}_t + \frac{\Delta t^2}{6}(\{\ddot{y}\}_{t+\Delta t} + 2\{\ddot{y}\}_t)$$

The solution procedures are summarized in Table VII.

Results and Discussion

In this chapter, the effect of the shear deformation is not considered. The results of elasto-plastic case are compared to the results of elastic case without the effect of the shear deformation. A computer program is developed for the elasto-plastic dynamic analysis. As mentioned before, for inelastic analysis, the direct integration method is usually employed. When using this method, the selection of time step is crucial. Wilson (22)

Table VII. Summary of step-by-step algorithm for nonlinear structural systems.

Initial calculations

1. Form stiffness matrix [K] and mass matrix [M].
2. Calculate the following constants (assume $[C] = \alpha[M] + \beta[K]$):

$\tau = \theta\Delta t \quad , \quad \theta \geq 1.37$

$b_0 = 1 + \frac{3}{\tau}\beta$

$b_1 = \frac{6}{\tau^2} + \frac{3}{\tau}\alpha$

$b_2 = \frac{b_1}{b_0}$

$b_3 = \alpha - \beta b_2$

$b_4 = \frac{6}{\tau^2} + \frac{3}{\tau} b_3$

$b_5 = \frac{6}{\tau} + 2b_3$

$b_6 = 2 + \frac{\tau}{2} b_3$

$b_7 = \frac{6}{\theta\tau^2 b_0}$

$b_8 = \frac{3}{\tau}\beta b_7 - \frac{6}{\theta\tau^2}$

$b_9 = 2\beta b_7 - \frac{6}{\theta\tau^2}$

$b_{10} = 1 - \frac{3}{\theta} + \frac{\tau}{2}\beta b_7$

$b_{11} = \frac{\Delta t}{2}$

$b_{12} = \frac{\Delta t^2}{6}$

3. Form effective stiffness matrix $[K]^* = [K] + b_2[M]$
4. Triangularize $[K]^*$

For each time increment

1. Form effective load vector $[R]^*$

$$[R]_t^* = [R]_t + \theta([R]_{t+\Delta t} - [R]_t) + [M](b_4\{y\}_t + b_5\{\dot{y}\}_t + b_6\{\ddot{y}\}_t) + \{q\}_t + \theta\{\Delta q\}_{t+\Delta t}$$

2. Solve for effective displacement vector $\{y\}_t^*$

$$[K]^*\{y\}_t^* = [R]_t^*$$

3. Calculate new acceleration, velocity and displacement vectors,

$$\{\ddot{y}\}_{t+\Delta t} = b_7\{y\}_t^* + b_8\{y\}_t + b_9\{\dot{y}\}_t + b_{10}\{\ddot{y}\}_t$$

$$\{\dot{y}\}_{t+\Delta t} = \{\dot{y}\}_t + b_{11}(\{\ddot{y}\}_{t+\Delta t} + \{\ddot{y}\}_t)$$

Table VII. (Cont.)

$$\{y\}_{t+\Delta t} = \{y\}_t + \Delta t\{\dot{y}\}_t + b_{12}(\{\ddot{y}\}_{t+\Delta t} + 2\{\ddot{y}\}_t)$$

4. Calculate the fictitious load increment $\{\Delta q\}_{t+\Delta t}$

$$\{\Delta q\}_{t+\Delta t} = [K_p]_{t+\Delta t}\{\varepsilon_{po}\}_{t+\Delta t}$$

5. Repeat steps 1 to 4 until $\{\Delta q\}^i_{t+\Delta t} - \{\Delta q\}^i_{t+\Delta t} \leq \varepsilon$.

6. Calculate $\{q\}_{t+\Delta t}$.

7. Repeat for next time increment.

suggested that the time increment Δt should be about 1/10 of the smallest natural period of the structure which is to be included in the response calculation. In the present study, the time step is chosen as 0.02 second whereas the fourth mode period is 0.217 seconds.

In the previous elastic dynamic seismic response analysis, the bending stress exceeds the elastic limits of the concrete ($0.85\ f_c'$) in the case of outer shell. In the case where damping coefficient was assumed as zero, the bending stress also exceeds the elastic limit of the concrete in the outer shell. These are, however, not the case for the inner shell. Therefore, only the outer shell is considered in the present elasto-plastic seismic response analysis. Again, the south-north components of acceleration of the 1940 El Centro earthquake are considered.

The time history response for the deflections at the tip of the outer shell are compared in Figure 5.9 with the response obtained assuming elastic behavior. Yielding starts at 11.94 seconds at the sixth node of the outer shell. Before this time, the response of the outer shell is in the elastic limit and the curve for the elasto-plastic response coincides with that for the elastic response. Beyond this time, the characteristic of the elasto-plastic response is quite similar to that of the elastic response. At the beginning period of the yielding (from 11.94 to 12.82 seconds), the stiffness of the outer shell is decreased due to the plastic strain. The tip deflections in this period for the elasto-plastic case are slightly greater than those for the elastic case. After this period, the outer shell is subjected to unloading and returns to the elastic range. Because the permanent strain produced in the preceding yielding period tends to prevent the reverse motion, the deflections of the outer shell for the elasto-plastic case are

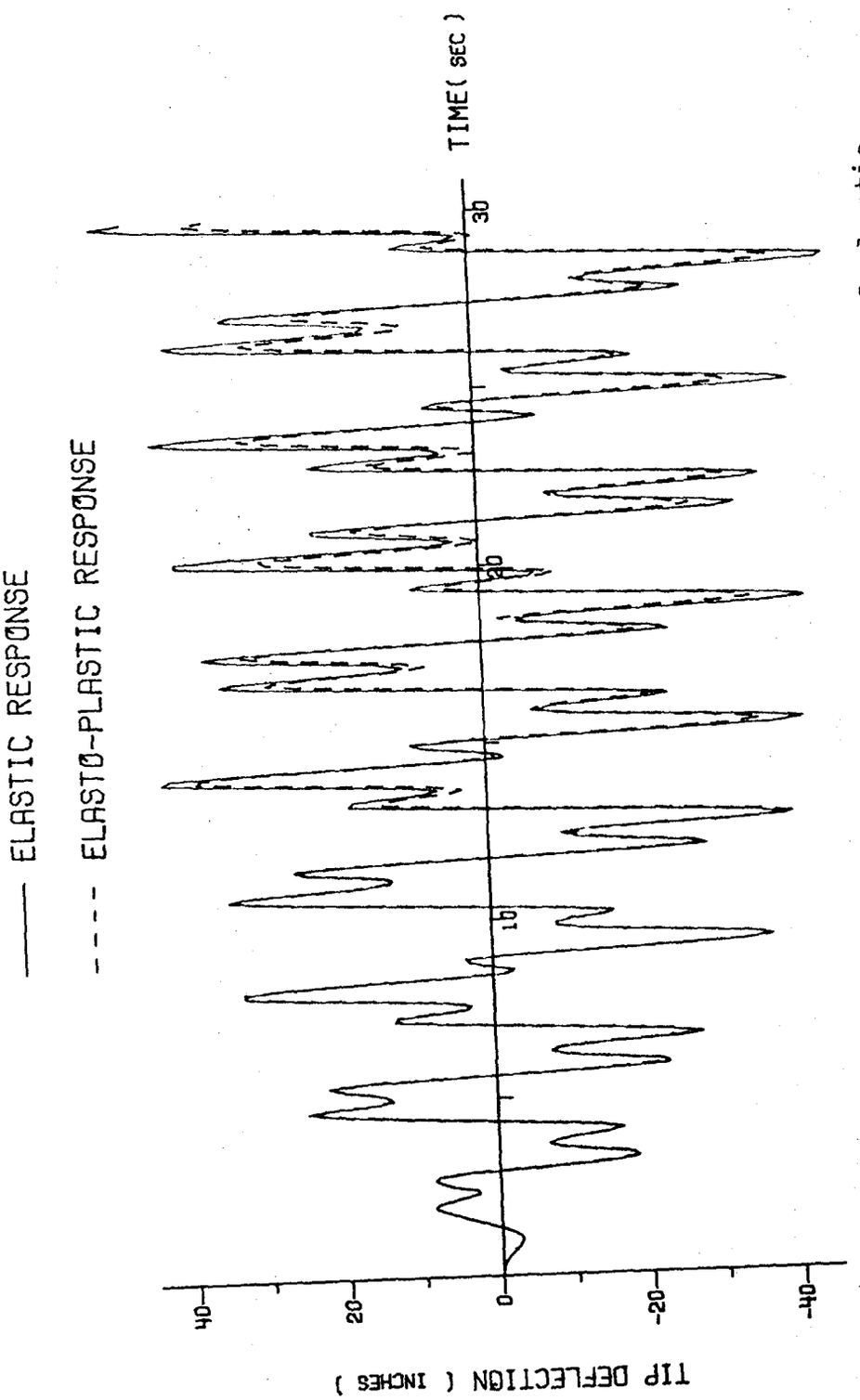

Figure 5.9 Comparison of time history responses of elastic and elasto-plastic cases for the tip deflection of outer shell.

smaller than those for the elastic case. When the reverse motion is further increased, the outer shell goes into another yielding period (from 13.2 to 14.2 seconds). The new plastic strain is produced and the deflection is also increased. However, the magnitudes of the deflection can never be greater than those for the elastic case except when the new plastic strain overcomes the preceding permanent (residual) strain. At the end of the response, the magnitude of the tip deflection for the elasto-plastic case is about 3/4 of the value for the elastic case. The maximum tip deflection is 40.99 inches at 12.8 seconds for the elasto-plastic case versus 39.78 inches at 12.8 seconds for the elastic case.

Figures 5.10 and 5.11 show the comparisons of the time history responses for the base bending moment and base shearing force of the outer shell for the elastic and the elasto-plastic cases. Because of the yielding and the existing residual strains, the magnitudes of the base bending moment and the base shearing force for the elasto-plastic case are smaller than those for the elastic case except in the first yielding period (11.94 to 12.82 seconds).

During the entire course of the response, only the sixth and the seventh nodal section of the outer shell have been developed into plastic ranges. The sixth nodal section has more unloading and reloading cycles than the seventh nodal section. Figure 5.12 shows the moment curvature rela relation curve for the sixth nodal section.

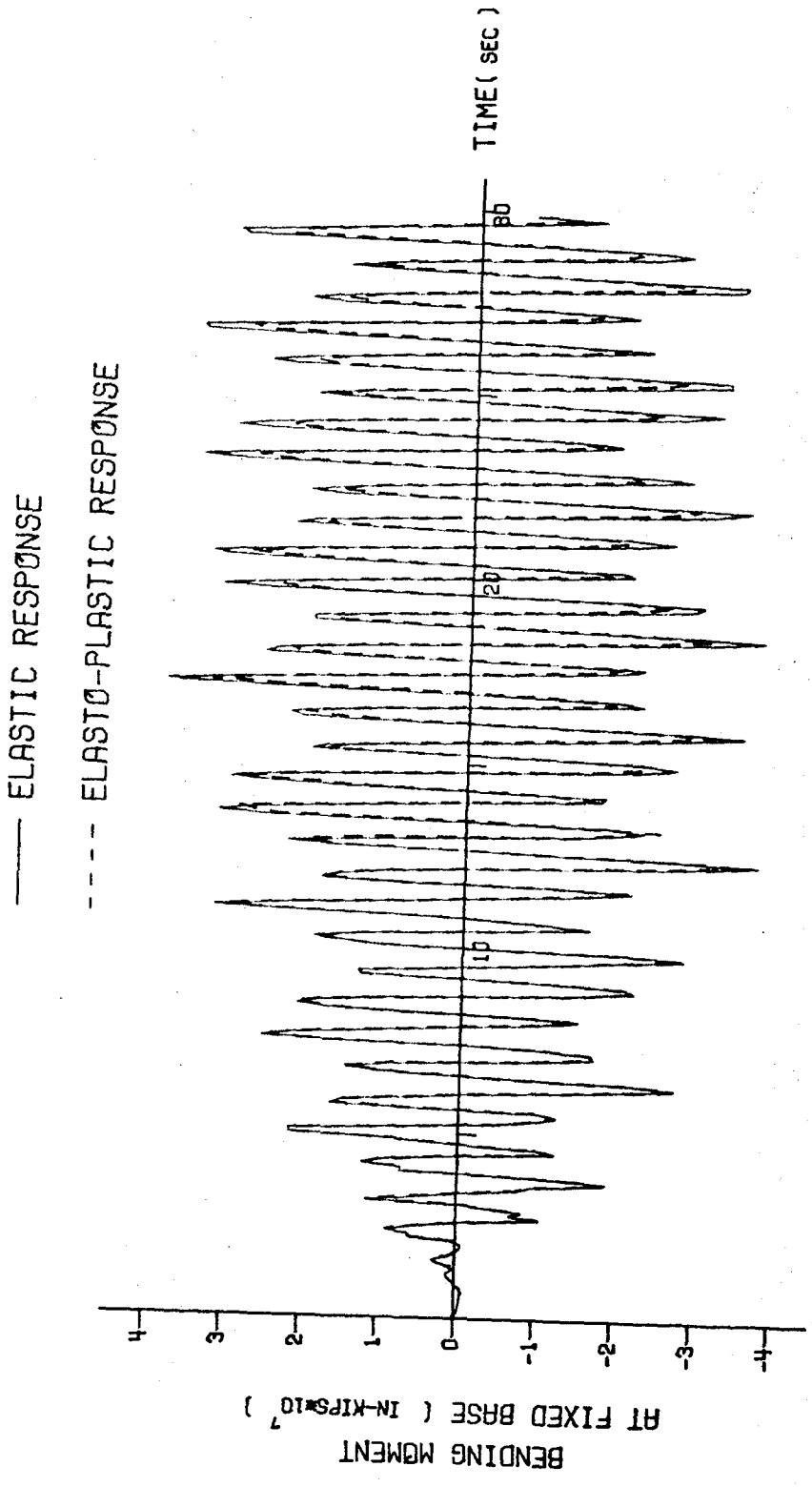

Figure 5.10 Comparison of time history responses of elastic and elasto-plastic cases for the base bending moment of outer shell.

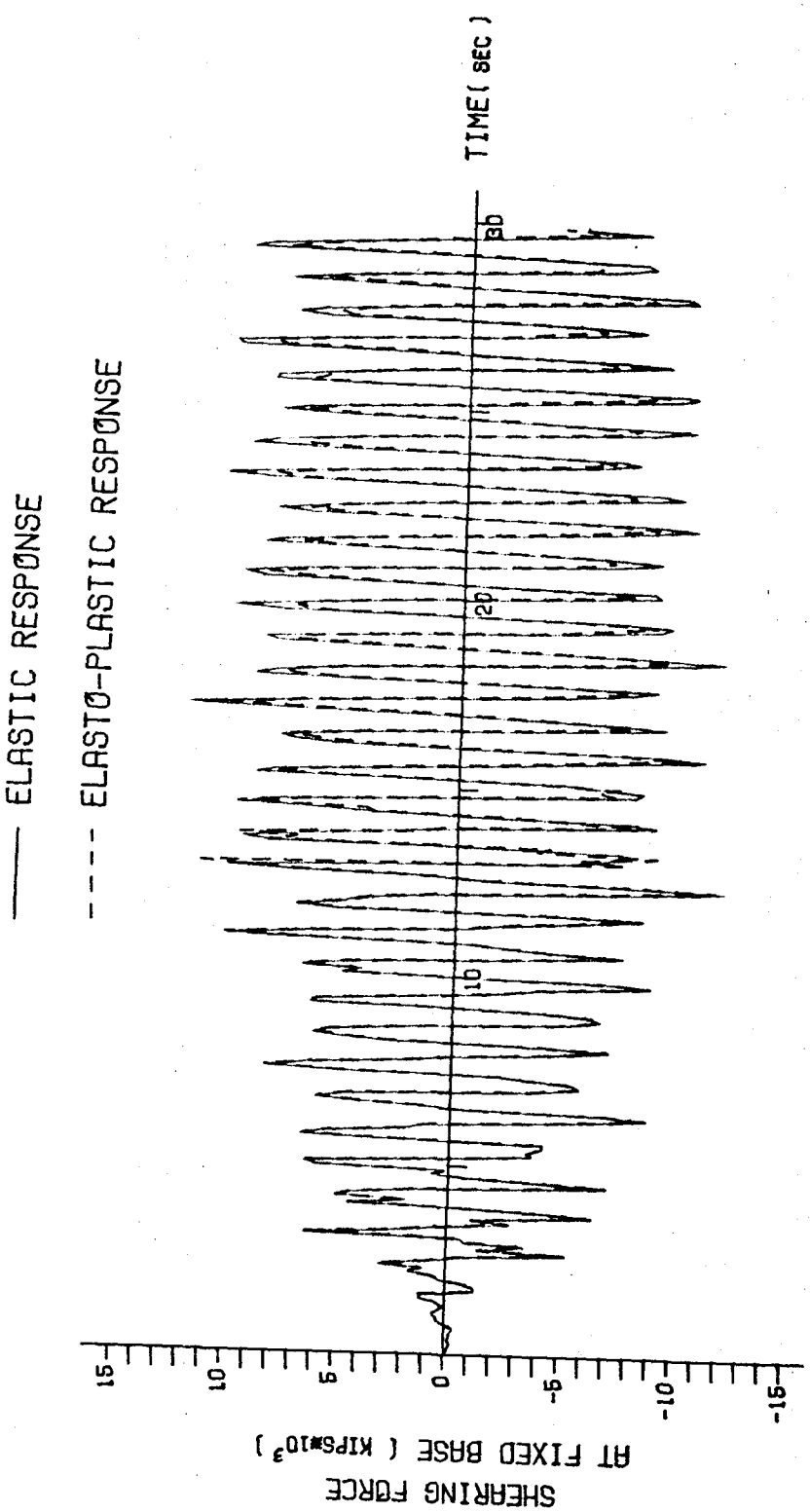

Figure 5.11 Comparison of time history responses of elastic and elasto-plastic cases for the base shearing force of outer shell.

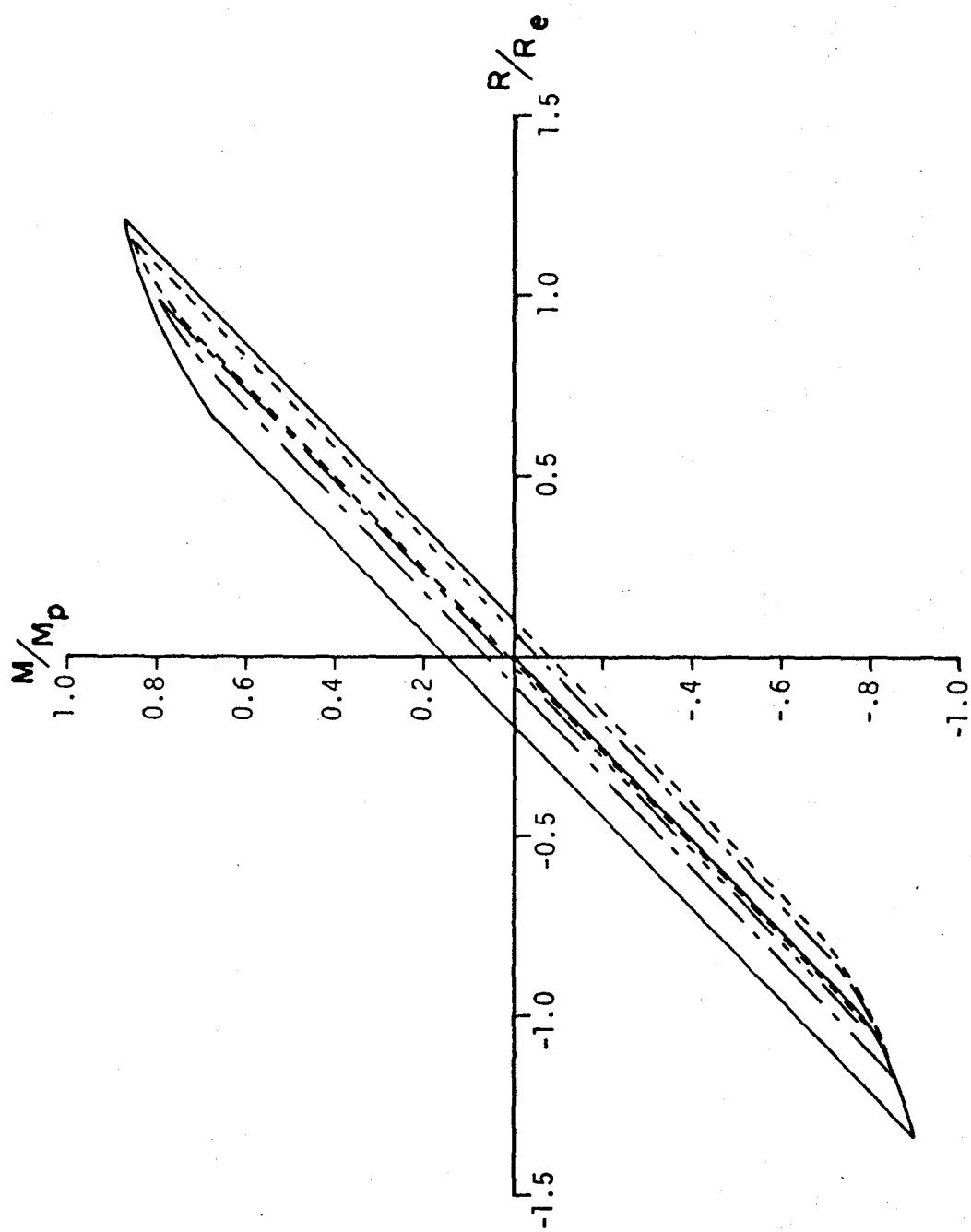

Figure 5.12 Moment-curvature relation for unloading and reloading of the outer shell at sixth nodal section.

5.4 Summary and Conclusions

The finite-element formulations and procedures presented in this chapter have been shown to be applicable for the computation of the inelastic dynamic response of tall slender beam structures. The use of initial strain concept for interpreting the effect of plastic strain enables one to use linear matrix equations of motion to analyze the inelastic dynamic behavior of structures.

The results obtained in this chapter show that the plastic strains produced in the chimney tend to prevent the motion of the outer shell. Hence, the resultant nodal displacements and nodal forces for the inelastic case are smaller than those for the elastic case.

In the present study, the material is assumed to have elastic-perfectly plastic behavior. If the strain hardening of the material is to be considered, only the initial strain stiffness matrix and the moment-curvature equations need to be derived. The procedures for the analysis still remain the same.

References

1. Abu-Saba, E.G., "Vibration of Chimney Supported on Elevated Concrete Slab," Journal of the Structural Division, ASCE, ST2, February 1971, p. 219.

2. Armen, H., Jr., Pifko, A. and Levine, H.S., "A Finite Element Method for the Plastic Bending Analysis of Structures," Grumman Research Department Report RE-347J, October 1968.

3. Bathe, K.J. and Wilson, E.L., "Stability and Accuracy Analysis of Direct Integration Methods," Earthquake Engineering and Structural Dynamics, Vol. 1, 1973, p. 283.

4. Busby, H.R. and Weingarten, V.I., "Response of Nonlinear Beam to Random Excitation," Journal of the Engineering Mechanics Division, ASCE, EM1, February 1973, p. 55.

5. Clough, R.W., "Earthquake Forces in a Tall Building," Civil Engineering, January 1956, p. 54.

6. Clough, R.W., "The Finite Element in Plane Stress Analysis," Proceedings of the 2nd ASCE Conference on Electronic Computation, Pittsburgh, Pa., September 1960.

7. Clough, R.W. and Tocher, J.L., "Finite Element Stiffness Matrices for the Analysis of Plate Bending," Proceedings of the First Conference on Matrix Methods in Structural Mechanics, Air Force Flight Dynamics Lab., TR-66-80, Dayton, Ohio, 1965.

8. Clough, R.W. and Benuska, K.L., "Nonlinear Earthquake Behavior of Tall Buildings," Journal of the Engineering Mechanics Division, ASCE, EM3, June 1967, p. 129.

9. Heidebrecht, A.C., Fleming, J.F. and Lee, S.L., "Dynamic Analysis of Inelastic Multi-degree Systems," Journal of the Engineering Mechanics Division, ASCE, EM6, December 1963, p. 193.

10. Heidebrecht, A.C., "Vibration of Nonuniform Simply Supported Beams," Journal of the Engineering Mechanics Division, ASCE, EM2, April 1967, p. 1.

11. Karasudhi, P., Tsai, Y.C. and Chan, K.P., "Earthquake Response of a Tall Multi-flue Stack," International Symposium on Earthquake Structural Engineering, St. Louis, Missouri, August 1976, p. 699.

12. Meyer, C., "Inelastic Dynamic Analysis of Tall Buildings," Earthquake Engineering and Structural Dynamics, Vol. 2, 1974, p. 325.

13. Paramesivaran, M.A. and Sukumaran, K., "A Lumped Mass Vibration Model of a Slender Latticed Cantilever," Computer & Structures, Vol. 6, 1976, p. 107.

14. Pecknold, D.A., "Inelastic Structural Response to 2D Ground Motion," Journal of the Engineering Mechanics Division, ASCE, EM5, October 1974, p. 949.

15. Prager, W. and Hodge, P.G., Theory of Perfectly Plastic Solids, John Wiley & Sons, New York, 1961.

16. Ramesh, C.K. and Fadnis, P.V., "Response of Reinforced Concrete Chimneys to Earthquake Forces," International Symposium on Earthquake Structural Engineering, St. Louis, Missouri, August 1976, p. 1293.

17. Rumman, W.S. "Earthquake Forces in Reinforced Concrete Chimneys," Journal of the Structural Division, ASCE, Proceeding Paper 5650, December 1967.

18. Veletses, A.S. and Vann, W.P., "Response of Ground Excited Elasto-plastic Systems," Journal of the Structural Division, ASCE, ST4, April 1971, p. 1257.

19. Walpole, W.R. and Shepherd, R., "Elasto-plastic Seismic Response of Reinforced Concrete Frame," Journal of the Structural Division, ASCE, ST10, October 1969, p. 2031.

20. Wang, P.C., Wang, W. and Drenick, R., "Critical Excitation and Response of Free Standing Chimneys," International Symposium on Earthquake Structural Engineering, St. Louis, Missouri, August 1976, p. 269.

21. Wilson, E.L. and Clough, R.W., "Dynamic Response by Step-by-Step Matrix," Symposium on the case of Computers in Civil Engineering, Lisbon, Portugal, October 1962, p. 451.

22. Wilson, E.L., Frahoomand, I. and Bathe, K.J., "Nonlinear Dynamic Analysis of Complex Structures," Earthquake Engineering and Structural Dynimics, Vol. 1, 1973, p. 241.

Appendix

Initial Strain Stiffness Matrix for Beam Finite Elements

The initial strain stiffness matrix for a beam element in pure bending is given in integral form in Equation (5.6). The matrix equation defining the fictitious nodal restoring forces in terms of the initial strain stiffness matrix is shown below for the pure bending of a beam with a rectangular cross section.

$$\begin{Bmatrix} F_i \\ M_i \\ F_j \\ M_j \end{Bmatrix} = \frac{EI}{h^3} \begin{bmatrix} C_1/\ell & C_2/\ell \\ C_3 & C_4 \\ -C_1/\ell & -C_2/\ell \\ C_5 & C_6 \end{bmatrix} \begin{Bmatrix} \varepsilon_{pi} \\ \varepsilon_{pj} \end{Bmatrix} = [K_p]\{\varepsilon_{po}\}$$

where

$$C_1 = \frac{(\bar{z}_j-\bar{z}_i)^2}{20} + h^2 - \frac{\bar{z}_i(h+\bar{z}_i)}{2}$$

$$C_2 = \frac{9(\bar{z}_j-\bar{z}_i)^2}{20} + \frac{(\bar{z}_j-\bar{z}_i)(2\bar{z}_i+h)}{2} - h^2 + \frac{\bar{z}_i(h+\bar{z}_i)}{2}$$

$$C_3 = -\frac{(\bar{z}_j-\bar{z}_i)^2}{60} - \frac{(\bar{z}_j-\bar{z}_i)(2\bar{z}_i+h)}{12} + h^2 - \frac{\bar{z}_i(h+\bar{z}_i)}{2}$$

$$C_4 = \frac{(\bar{z}_j-\bar{z}_i)^2}{10} + \frac{(\bar{z}_j-\bar{z}_j)(2\bar{z}_i+h)}{12}$$

$$C_5 = \frac{(\bar{z}_j-\bar{z}_i)^2}{15} + \frac{(\bar{z}_j-\bar{z}_i)(2\bar{z}_i+h)}{12}$$

$$C_6 = \frac{7(\bar{z}_j-\bar{z}_i)^2}{20} + \frac{5(\bar{z}_j-\bar{z}_i)(2\bar{z}_i+h)}{12} - h^2 + \frac{\bar{z}_i(h+\bar{z}_i)}{2}$$

Part II

Vibrations of Two Cyclinders in Tandem in Line of Wind

I. Introduction

Recently, because the size of tall slender structures used in power plants or other installations has been greatly increased, their resistance to dynamic forces such as earthquakes and winds becomes extremely important. Such structures, if flexible and lightly damped, may exhibit large deflections or unstable oscillations due to wind loadings. The resulting oscillating phenomenon induced by vortices in the wake is an important engineering problem.

Early studies were concentrated on the determination of the fluctuating lift force on a single circular cylinder, either stationary or vibratory. However, when two cylinders are put in tandem in the flow direction, the rear one may vibrate with either larger or smaller deflection than a single cylinder. The question can be asked how important a factor is the position of a cylinder in the wake of another cylinder on the vibrating behavior of the rear cylinder.

The purpose of this research is to perform analytical studies of the vortex-induced vibration of two tall slender structures in tandem in a flowing fluid. A mathematical model is proposed to study the interaction of lift forces and the vibrating behavior of the rear cylinder.

II. Literature Survey

(a) A Single Stationary Cylinder

Attempts to measure the lift force acting on a stationary cylinder, due to vortices in its wake, and to correlate the results of measurements were made by a great number of authors. Sallet (1) employed the fluid momentum equation, integrated over an appropriate control volume, to determine the fluctuating lift force on a bluff body. It is the same method that was introduced by von Karman for the calculation of the steady drag force. The equation for the maximum lift coefficient obtained by Sallet is

$$C_L = \sqrt{2}\,\frac{\ell}{D}\left(1 - \frac{S\ell}{D}\right)\left(3\,\frac{S\ell}{D} - 2\right) \qquad (1)$$

in which C_L = lift coefficient

ℓ = longitudinal vortex spacing

D = cylinder diameter

S = Strouhal number

In his previous paper (2), Sallet derived an equation relating S, C_D and $\frac{\ell}{D}$ as following

$$S^2\left(\frac{\ell}{D}\right)^3 + 0.529S\left(\frac{\ell}{D}\right)^2 - 1.529\frac{\ell}{D} + 1.593\,C_D = 0 \qquad (2)$$

where C_D is the drag coefficient. If the Strouhal number and the drag coefficient of the cylinder at the Reynolds number of interest are known, the lift coefficient of any stationary cylinder can be determined from Equations (1) and (2).

(b) A Single Vibrating Cylinder

In 1969, Mei and Currie (3) found, in their experiment on a vibrating cylinder excited by its own vortices in the wake, the position of the separation point of the boundary layer on the

cylinder surface varies during the vibration of the cylinder. The phase angle ϕ of the lift force F and the phase angle ψ of the movement of the separation point during the cylinder vibration, both measured with respect to the cylinder motion X_r are plotted in Figure 1. Those data will be used in the present investigation to calculate the distance between a cylinder and the nearest shedding vortex from it when this cylinder is in its equilibrium position.

The cylinder motion of a vibrating cylinder can strongly affect the lift force. Bishop/Hassen (4) found from their tests that the lift force is increased with the amplitude of cylinder motion. They also concluded from such tests that the fluctuating lift force acting on the cylinder is indicative of a self-excited oscillatory mechanism in the flow field. Recently, several mathematical models which attempt to duplicate the experimental observations have been postulated. The most successful of these models is that of Hartlen and Currie (5) who assume that the oscillating lift force on the cylinder can be represented by an equation in the form of the van der Pol equation. The oscillator equation in dimensionless form is as following:

$$\ddot{C}_L - \alpha\omega_o\dot{C}_L + \frac{\gamma}{\omega_o}(\dot{C}_L)^3 + \omega_o^2 C_L = b\dot{X}_r$$

in which α and b are independent constants while γ and α are related by the equation $\gamma = \frac{4\alpha}{3C_{L_o}^2}$ where C_{L_o} is the amplitude of lift coefficient of a stationary cylinder and can be determined from Equation (1). When this equation is coupled to the equation of

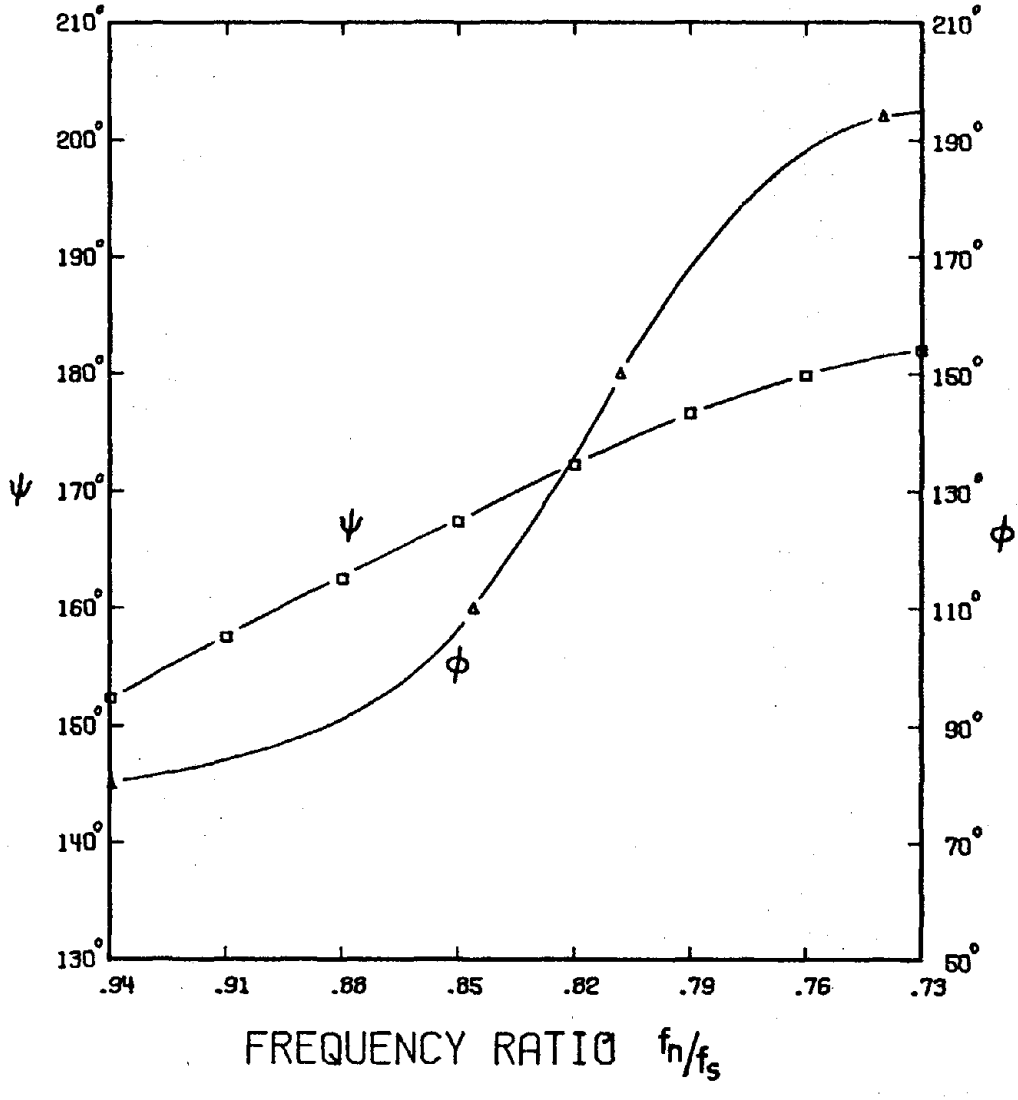

Figure 1. Phase angles ψ and ϕ versus frequency ratio f_n/f_s.

motion for a cylinder and the parameters appearing in the model are appropriately chosen, the observed behavior is qualitatively reproduced. This model will be used by this author in his study of the dynamic behavior of two cylinders in tandem in the wind direction.

(c) Two Cylinders in Tandem

When two cylinders are put in line in the flow direction, the rear one was subjected to two kinds of forces, one is due to its own vortex street and another is the buffeting force from the wake of the upstream cylinder. The phase angle between those two forces is dependent on the position of the rear cylinder related to the front cylinder. Therefore, the amplitude of the rear cylinder motion is also largely dependent on the distance between those two cylinders.

The water-tunnel studies of Vickery (6) have shown that the amplitude of vibration of the rear cylinder increases with the spacing between two cylinders. But his results only appear for spacing ratio from 2.8D to 4.3D as shown in Figure 2. Below the spacing ratio of 2.8D or above 4.3D, the rear cylinder may be excited to higher or lower amplitudes.

As mentioned in Mair and Maull's paper (7), the experimental results of Whitbread and Wootton on oscillation of two aeroelastic models of octagonal section, placed in line with the wind direction, are shown in Figure 3. The position of minimum amplitude of vibration of the rear cylinder seems to be around the spacing ratio of 3.5D. Above a spacing ratio of 4D the rear cylinder is excited to very high amplitudes.

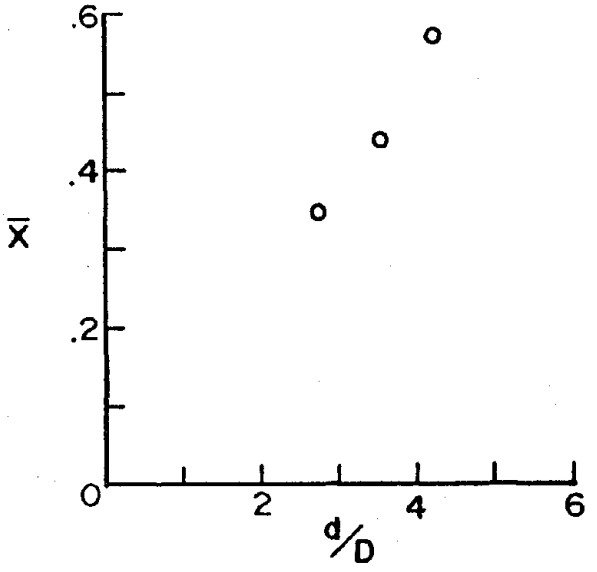

Figure 2. Max. amplitude of vibration of the downstream member of a pair of cylinder.

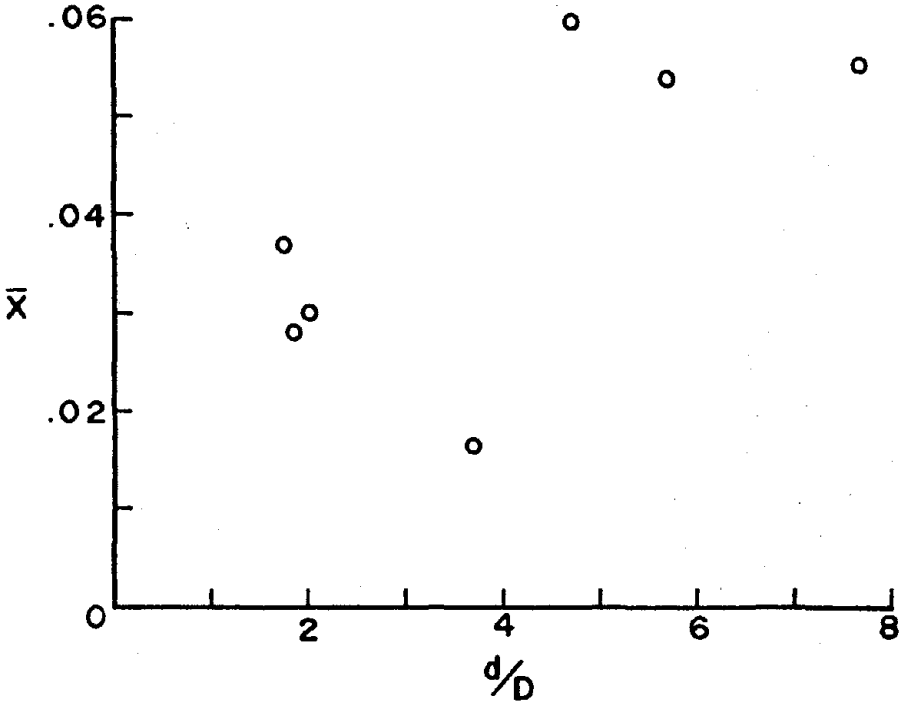

Figure 3. The maximum amplitude of oscillation of one body behind another.

The predictions of the mathematical model as proposed by the author in this investigation will be compared later with results of these experimental studies.

III. Formulation of a Two-dimensional Mathematical Model

(a) The Model

The physical systems shown in Figures 4 and 5 are considered.

In Figure 4, a rigid cylinder of mass M, diameter D and length L is exposed to a flow of uniform velocity V. The cylinder is mounted elastically on springs of total stiffness K and on viscous dampers of total damping coefficient R. The origin of coordinates is at the stationary cylinder center with displacements perpendicular to the free stream denoted by X_r. The external lift force acting on the cylinder is F.

In Figure 5 two cylinders, both having the same physical properties as described in Figure 4, are put in tandem in the wind direction. The distance from center to center of two cylinders is d. Where d' is the distance between cylinder 1 and the nearest shedding vortex from it when cylinder 1 is in its equilibrium position.

(b) Mathematical Formulation for a Single Cylinder

(1) The Structural Equation

The equation of motion of a rigid cylinder mounted on springs and dampers, such as shown in Figure 4, is given by

$$M\ddot{X}_r + R\dot{X}_r + KX_r = F$$

where the lift force F can be expressed by the term

$$F = \frac{1}{2}\rho V^2 DLC_L$$

in which C_L = lift coefficient

ρ = density of the fluid

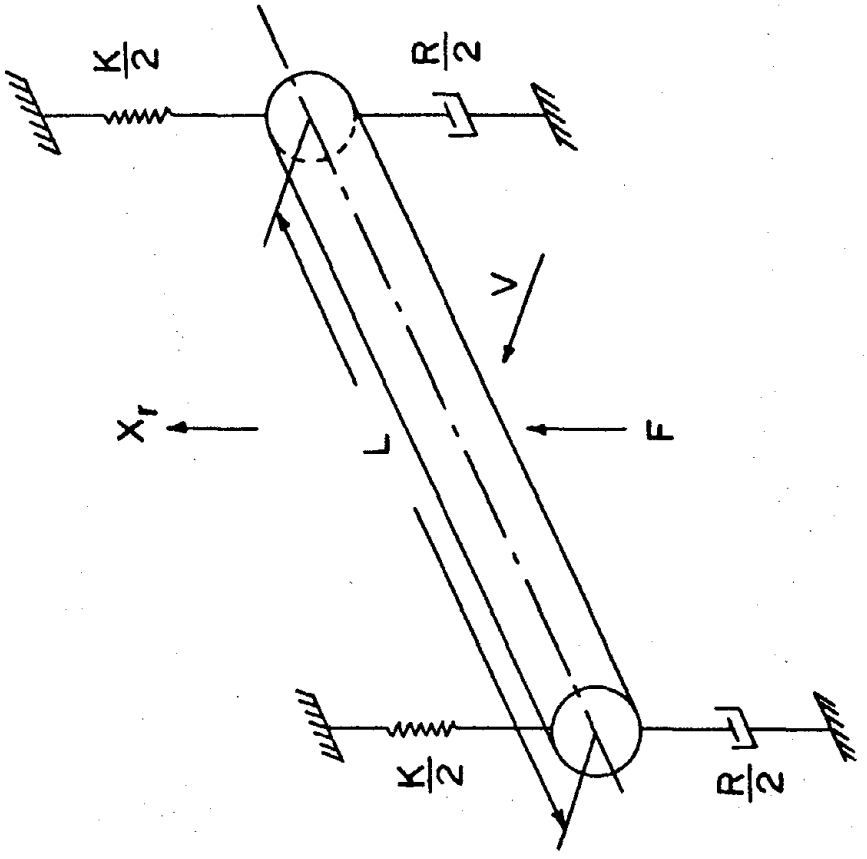

Figure 4. Model structure for analysis.

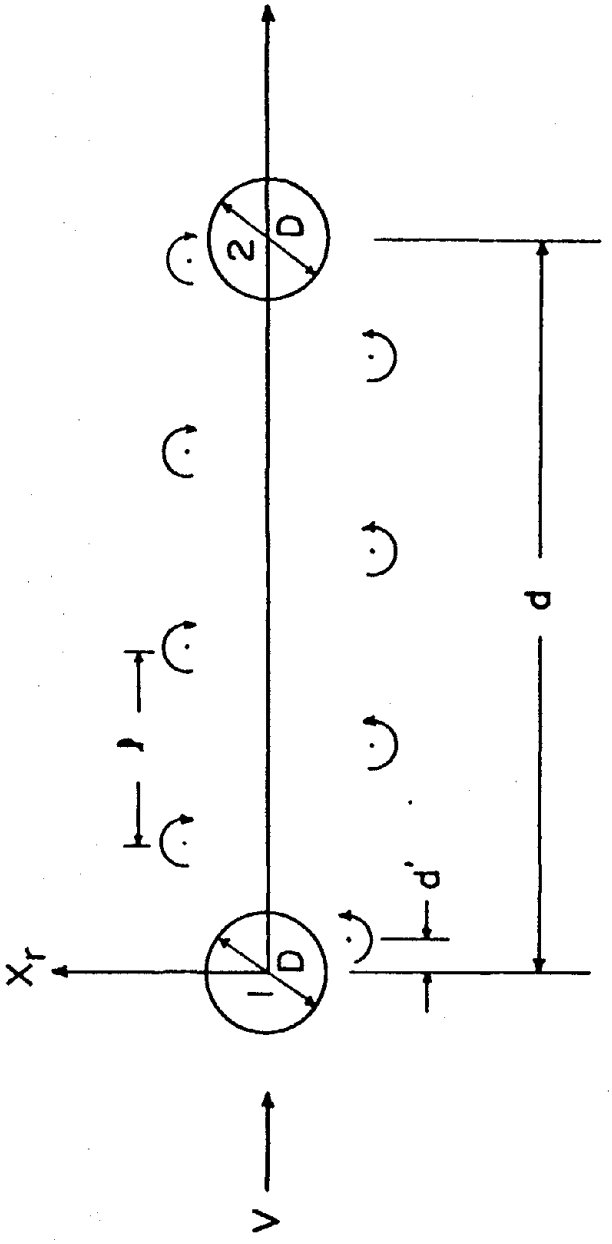

Figure 5. Model for two cylinders in tandem.

The above equation becomes

$$M\ddot{X}_r + R\dot{X}_r + KX_r = \frac{1}{2}\rho V^2 DLC_L \qquad (3)$$

Introducing dimensionless variables X and τ defined by

$$X = \frac{X_r}{D}, \quad \tau = t\sqrt{\frac{K}{M}} = \omega_n t \qquad (4)$$

and dimensionless parameters defined by

$$\zeta = \frac{R}{2M\omega_n}, \qquad a = \frac{\rho D^2 L}{8\pi^2 S^2 M}$$

$$\omega_o = \frac{f_s}{f_n} = \frac{SV}{f_n D} \qquad (5)$$

where S = Strouhal number

f_s = vortex shedding frequency

$\omega_n = 2\pi f_n$ = natural frequency of the cylinder

one has the following nondimensional equation of motion of the cylinder

$$\ddot{X} + 2\zeta\dot{X} + \dot{X} = a\omega_o^2 C_L \qquad (6)$$

(2) The Aerodynamic Equation

In 1970, Hartlen and Currie (5) introduced a nonlinear oscillator model which contains a nonlinear negative damping term. This model makes it possible for the system to be self-excited and self-limiting in amplitude. This oscillator is coupled with the vibrating cylinder by a force proportional to the vibrating velocity of the cylinder. The oscillator equation in dimensionless form is as following:

$$\ddot{C}_L - \alpha\omega_o\dot{C}_L + \frac{\gamma}{\omega_o}(\dot{C}_L)^3 + \omega_o^2 C_L = b\ddot{X} \qquad (7)$$

in which α and b are independent constants while γ and α are related by the equation $\gamma = \frac{4\alpha}{3C_{L_o}^2}$ where C_{L_o} is the amplitude of lift coefficient of a stationary cylinder and can be determined from Equation (1).

For a single cylinder, one has to solve Equations (6) and (7) together for the two unknown X and C_L, for prescribed values of ζ, a, ω_o, α, γ, and b. Of these six parameters, the choice of α and b are most difficult because of the lack of experimental data.

(c) Mathematical Formulation for Two-Cylinder in Tandem

For two cylinders in tandem in line with the wind direction, the following simplifying assumptions are made in the present investigation:

(1) The investigation is limited to cases where the two cylinders are at a fair distance apart, say $d > 2D$.

(2) For $d > 2D$, it is reasonable to neglect the effect of rear cylinder motion on the front cylinder. The motion of the front cylinder and the corresponding vortices created by it will definitely affect the rear cylinder as a buffeting force.

(3) The vortices created by the motion of the front cylinder, after it reaches the second cylinder and acts on the rear cylinder as a buffeting force, loses its effect as far as the wake behind the rear cylinder is concerned.

(4) The rear cylinder is therefore considered to be acted upon by two forces: the buffeting force from the front cylinder, F_1, and the lifting force F_2 due to the wake of the rear cylinder alone.

Based on the above assumptions, the system in Figure 5 can be treated as following:

(i) The cylinder motion equation and the aerodynamic equation for cylinder 1 are given by Equations (6) and (7) or

$$\ddot{X}_1 + 2\zeta\dot{X}_1 + X_1 = a\omega_o^2 C_{L_1} \tag{8}$$

$$\ddot{C}_{L_1} - \alpha\omega_o\dot{C}_{L_1} + \frac{\gamma}{\omega_o}(\dot{C}_{L_1})^3 + \omega_o^2 C_{L_1} = b\ddot{X}_1 \tag{9}$$

(ii) The second cylinder, in the absence of cylinder 1, will have a motion x_2 of its own, and corresponding lift coefficient C_{L_2}. The two variables x_2 and C_{L_2} are governed by the same Equations (6) and (7) or

$$\ddot{x}_2 + 2\zeta\dot{x}_2 + x_2 = a\omega_o^2 C_{L_2} \tag{8}a$$

$$\ddot{C}_{L_2} - \alpha\omega_o\dot{C}_{L_2} + \frac{\gamma}{\omega_o}(\dot{C}_{L_2})^3 + \omega_o^2 C_{L_2} = b\ddot{X}_2 \tag{8}b$$

(iii) With the presence of cylinder 1, cylinder 2 is subject to two forces, one from its own vortex street as if cylinder 1 is not there, and another from the wake of cylinder 1. The first is represented by $C_{L_2}(\tau)$ which can be obtained by solving Equations (8)a and (9)a. The second is represented by $C_{L_1}(\tau+\tau_1)$, where $C_{L_1}(\tau)$ can be solved from Equations (8) and (9) and τ_1 is a time delay depending on the time required for the vortices created by the motion of cylinder 1 to reach cylinder 2.

The motion of cylinder 2, to be represented by X_2^*, under both forces, is governed by the following

$$\ddot{x}_2^* + 2\zeta\dot{x}_2^* + x_2^* = a\omega_o^2 \left[C_{L_2}(\tau) + C_{L_1}(\tau+\tau_1)\right] \qquad (10)$$

The mathematical model is then represented by 5 equations, (8), (9), (8)a, (9)a and (10). These equations are nonlinear in nature with a time-delay term in it.

IV. Solutions

(a) Dynamic Response by Direct Integration

The 5 equations (8) through (10) can be integrated directly with the aid of a computer. The integration can be divided into 3 steps:

(1) Equations (8) and (9) are integrated first to obtain $C_{L_1}(\tau)$. This can be accomplished by standard numerical integration process such as Runge-Kutta's method with built-in error correction procedure. The initial conditions must be prescribed.

To make use of existing program in numerical integration, Equations (8) and (9) are rewritten into the following simultaneous equations of first order:

$$\begin{aligned} \dot{y}_1 &= y_2 \\ \dot{y}_2 &= a\omega_o^2 y_3 - 2\zeta y_2 - y_1 \\ \dot{y}_3 &= y_4 \\ \dot{y}_4 &= by_2 + \alpha\omega_o y_4 - \frac{\gamma}{\omega_o} y_4^3 - \omega_o^2 y_3 \end{aligned} \tag{11}$$

where $y_1 = x_1$ $\quad y_2 = \dot{x}_1 = \dot{y}_1$

$y_3 = C_{L_1}$ $\quad y_4 = \dot{C}_{L_1} = \dot{y}_3$

(2) Equations (8)a and (9)a can be integrated in exactly the same manner to obtain $C_{L_2}(\tau)$.

(3) One now proceeds to integrate Equation (10) to obtain the motion $x_2^*(\tau)$ of the rear cylinder under both forces represented by $C_{L_1}(\tau+\tau_i)$ and $C_{L_2}(\tau)$.

Note that $C_{L_2}(\tau)$ as obtained from step (2) can be fed into the right side of Equation (10) directly. But $C_{L_1}(\tau)$ obtained from step (1) must be corrected for the time delay before it can be used in Equation (10).

The direct integration was carried out for several examples. One example is shown in Figure 6. It shows that the dynamic responses of both cylinders (and lifting force on them) approach steady state oscillations after a certain time interval. In this case, it takes about 40000 integration steps in τ.

It is observed experimentally that when f_s is near f_n (locked-in region or synchronization), both cylinder motions and lift forces are approximately sinusoidal at a frequency very close to f_n, the natural frequency of the cylinder. Therefore, it is of interest to investigate the steady state solution.

(b) Steady State Solution

Because the direct integration method needs a lot of computer time to arrive at the steady state solution, it is desirable to seek the solutions of Equations (8) to (10) in the form of sinusoidal function.

(1) Cylinder 1

Assume the solutions of equations (8) and (9) in the following form:

$$x_1 = \bar{X}_1 \sin \omega_1 \tau \qquad (12)$$

$$C_{L_1} = \bar{C}_{L_1} \sin (\omega_1 \tau + \phi_1)$$

Substituting Equation (12) into Equations (8) and (9) and equating coefficients of sin $\omega\tau$ and cos $\tau\omega$ separately gives

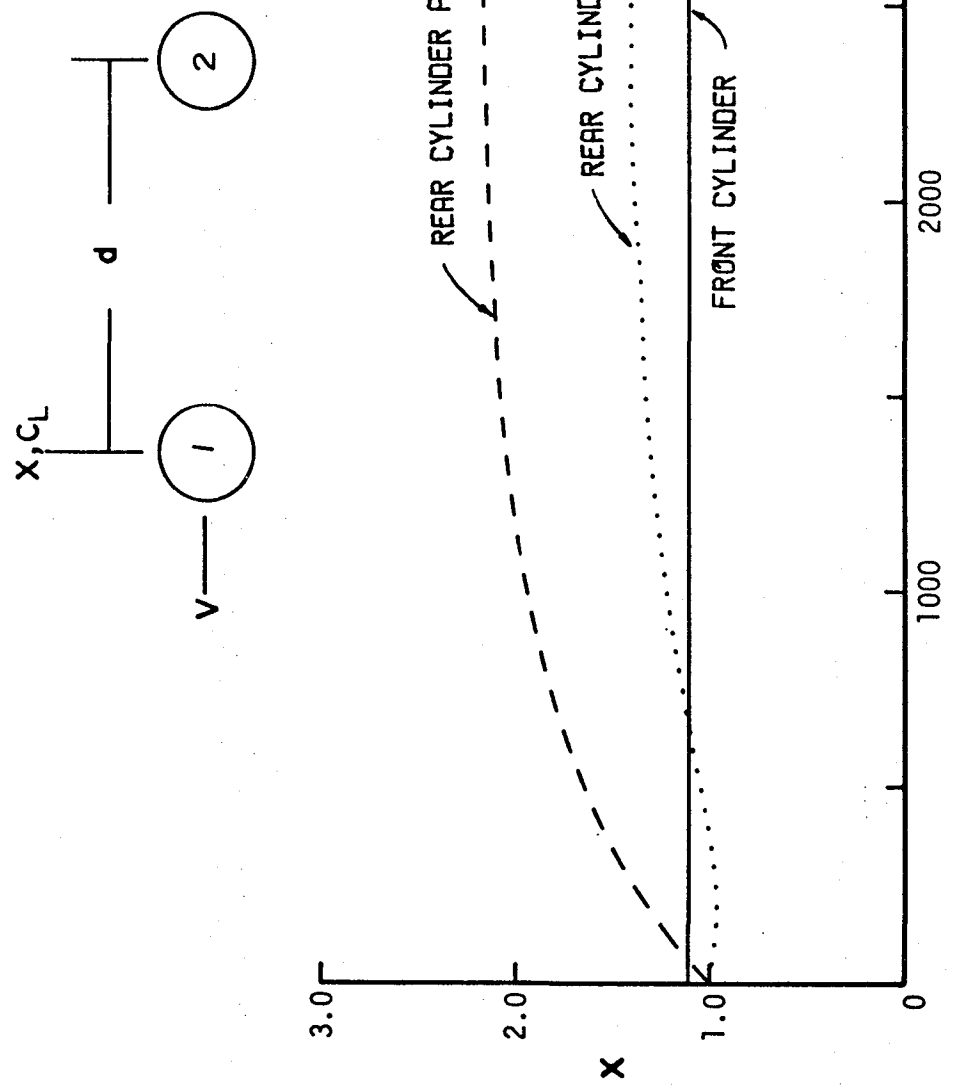

Figure 6. Cylinder amplitude versus time.

$$\bar{C}_{L_1} \cos \phi_1 = \frac{(1-\omega_1^2)\bar{X}_1}{a\omega_o^2} \tag{13)a}$$

$$\bar{C}_{L_1} \sin \phi_1 = \frac{2\zeta\omega_1\bar{X}_1}{a\omega_o^2} \tag{13)b}$$

$$[2\zeta\omega_1(\omega_o^2 - \omega_1^2) - \alpha\omega_o\omega_1(1-\omega_1^2) - ab\omega_1\omega_o^2]$$
$$+ \frac{3\gamma\omega_1^3\bar{X}_1^2}{4a^2\omega_o^5}[(1-\omega_1^2)^3 + 4\zeta^2\omega_1^2(1-\omega_1^2)] = 0 \tag{13)c}$$

$$[(1-\omega_1^2)(\omega_o^2 - \omega_1^2) + 2\alpha\zeta\omega_o\omega_1^2]$$
$$- \frac{3\gamma\omega_1^3\bar{X}_1^2}{4a^2\omega_o^5}[8\zeta^3\omega_1^3 + 2\zeta\omega_1(1-\omega_1^2)^2] = 0 \tag{13)d}$$

Eliminating $\bar{X}_1$ from Equations (13)c and (13)d gives, after some rearranging, the following frequency equation

$$(\omega_o^2 - \omega_1^2)[(1-\omega_1^2) + 4\zeta^2\omega_1] - 2ab\zeta\omega_o^2\omega_1^2 = 0 \tag{14}$$

After solve Equation (14) to obtain ω_1 and substitute back into Equations (13)d, (13)b and (13)a, the unknowns $\bar{X}_1$, $\bar{C}_{L_1}$ and ϕ_1 can be found.

(2) Cylinder 2 (with cylinder 1 absent)

Assume the solutions of Equations (8)a and (9)a as

$$X_2 = \bar{X}_2 \sin \omega_2\tau$$
$$C_{L_2} = \bar{C}_{L_2} \sin (\omega_2\tau + \phi_2) \tag{15}$$

Substituting Equation (15) into Equations (8)a and (9)a and using the same methods in the previous paragraph, the solutions of $\bar{X}_2$, $\bar{C}_{L_2}$, ϕ_2 and ω_2 can be solved. Those solutions

are for the second cylinder when cylinder 1 is absent.

(3) Cylinder 2 (when cylinder 1 is present)

When cylinder 1 is present, the motion of cylinder 2 is governed by Equation (10). Assume the solution of this equation as

$$X_2^* = \bar{X}_2^* \sin(\omega_2\tau + \theta)$$

$$C_{L_2} = \bar{C}_{L_2} \sin(\omega_2\tau + \phi_2) \qquad (16)$$

$$C_{L_1} = \bar{C}_{L_1} \sin(\omega_1\tau + \omega_1\tau_1)$$

where θ is the phase angle between two cylinders. Substituting Equation (16) into Equation (10) gives

$$[(1-\omega_2^2)\bar{X}_2^* \cos\theta - 2\zeta\omega_2\bar{X}_2^* \sin\theta] \sin\omega_2\tau +$$

$$[(1-\omega_2^2)\bar{X}_2^* \sin\theta + 2\zeta\omega_2\bar{X}_2^* \cos\theta] \cos\omega_2\tau =$$

$$a\omega_o^2[\bar{C}_{L_2} \cos\phi_2 \sin\omega_2\tau + \bar{C}_{L_2} \sin\phi_2 \cos\omega_2\tau +$$

$$\bar{C}_{L_1} \cos\omega_1\tau_1 \sin\omega_1\tau + \bar{C}_{L_1} \sin\omega_1\tau_1 \cos\omega_1\tau] \qquad (17)$$

If two cylinders are identical, then $\omega_1 = \omega_2 = \omega$. By equating coefficients of sin $\omega\tau$ and cos $\omega\tau$, Equation (17) can be divided into two equations as follows

$$(1-\omega^2)\bar{X}_2^* \cos\theta - 2\zeta\omega\bar{X}_2^* \sin\theta = a\omega_o^2(C_{L_2} \cos\phi_2 + C_{L_1} \cos\omega\tau_1)$$

$$(1-\omega^2)\bar{X}_2^* \sin\theta + 2\zeta\omega\bar{X}_2^* \cos\theta = a\omega_o^2(\bar{C}_{L_2} \sin\phi_2 + \bar{C}_{L_1} \sin\omega\tau_1)$$

Because ω, $\bar{C}_{L_1}$, $\bar{C}_{L_2}$, ϕ_2 and τ_1 are known, $\bar{X}_2^*$ and θ can be determined from these two equations.

V. Results and Discussions

The variations of $\bar{X}_2^*$ and $\bar{C}_{L_2}$ with spacing d/D are shown in Figure 7. The curves in this figure are periodic and the distance between two peaks of $\bar{X}_2^*$ or $\bar{C}_{L_2}$ is equal to longitudinal vortex space ℓ of the vortex street. The maximum value of $\bar{X}_2^*$ is about three times of $\bar{X}_1$ and the minimum value is about half of $\bar{X}_1$.

The periodical nature of these curves will be destroyed if the energy dissipation of vortices is considered. The maximum and minimum values which appear periodically along spacing ratio will be decayed. Therefore, the first two peaks, minimum $\bar{X}_2^*$ at 3.1D and maximum $\bar{X}_2^*$ at 5.7D, become very important.

The curves shown in Figure 8 represent the ranges of locked-in or synchronization that an oscillation can be generated. The maximum amplitude of $\bar{X}_1$ occurs at $\omega_o = 1.14$ and the maximum or monimum value of $\bar{X}_2^*$ occurs at $\omega_o = 1.15$. For various a, ζ, α or b the maximum value of $\bar{X}$ will be occurred at different ω_o.

In Figure 9, the value of $\bar{\omega}_o$ at which the amplitude of cylinder motion is maximum is plotted vs. the ratio of damping coefficient ζ to mass parameter a. For $\frac{2\zeta}{a} < 1.0$, $\bar{\omega}_o$ is far away from 1.0 and the maximum amplitude of $\bar{X}$ is too large (see Figure 10), it means that the structural damping is not large enough and the structure will fail.

Comparing Figures 7 and 9 with the experimental data shown in Figures 2 and 3, one finds that the proposed mathematical model gives results in good agreement with experimental data, i.e., the location of rear cylinder at which the amplitude of vibration is minimum is at approximately 3.1D away from the front cylinder.

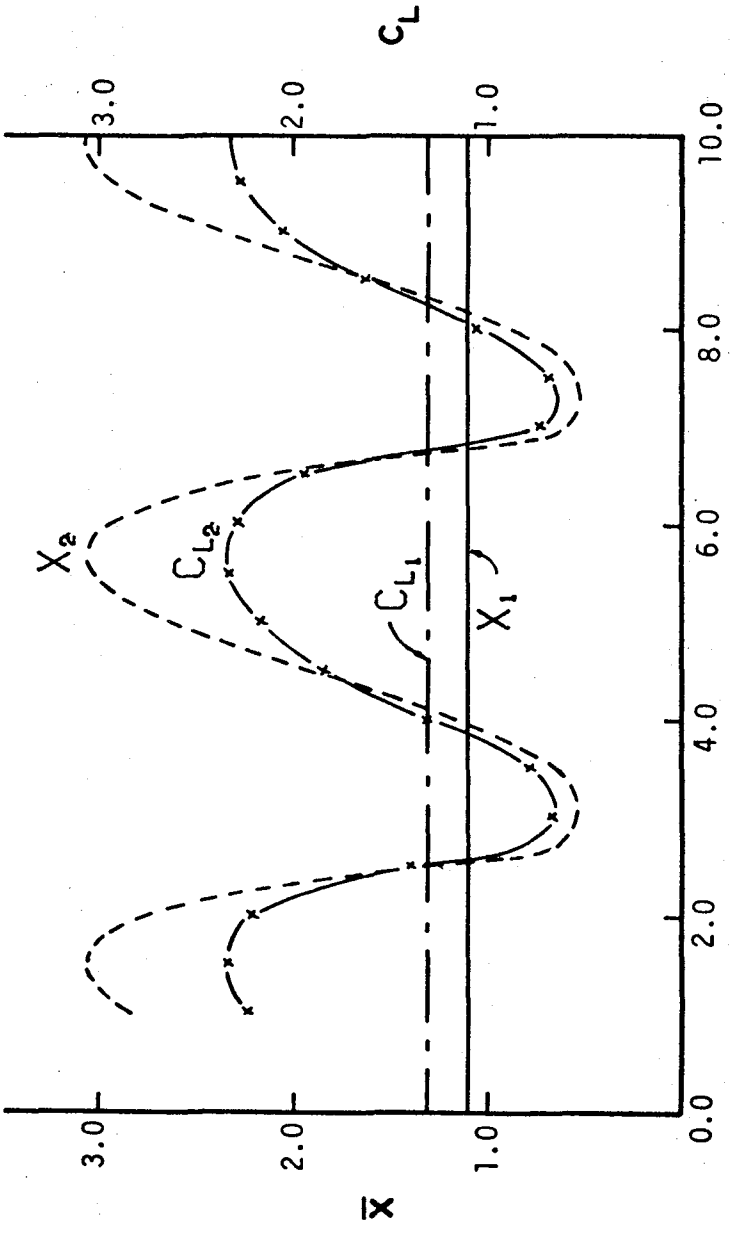

Figure 7. Cylinder amplitude versus spacing ratio.

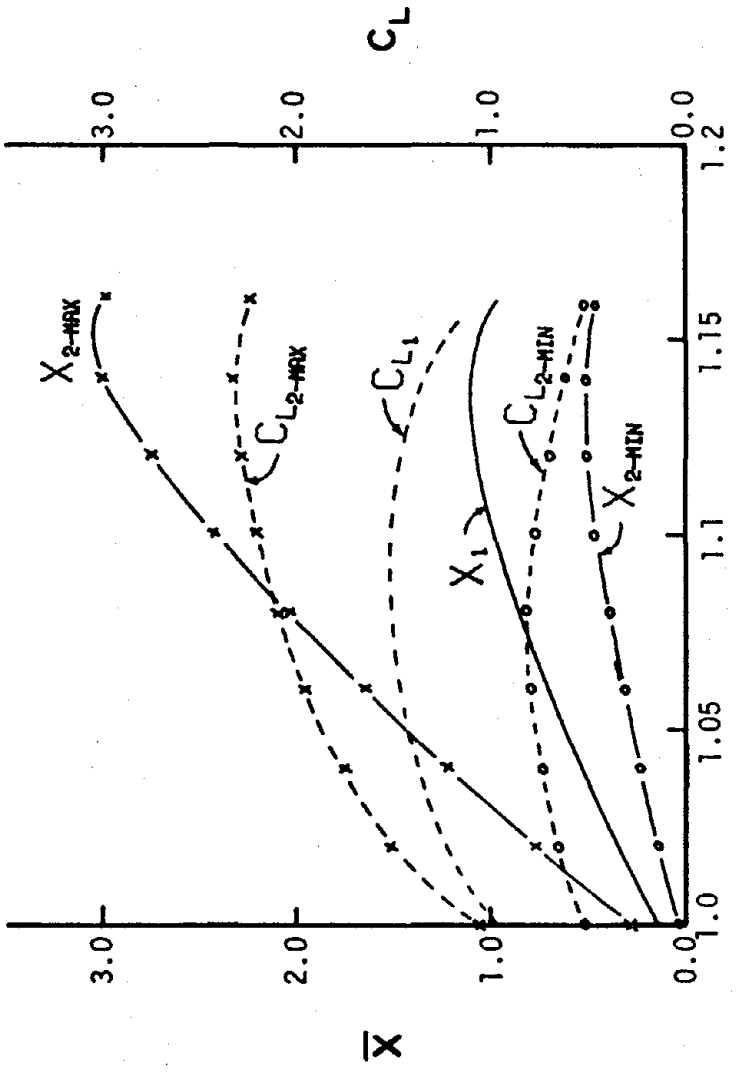

Figure 8. Cylinder amplitude versus wind speed.

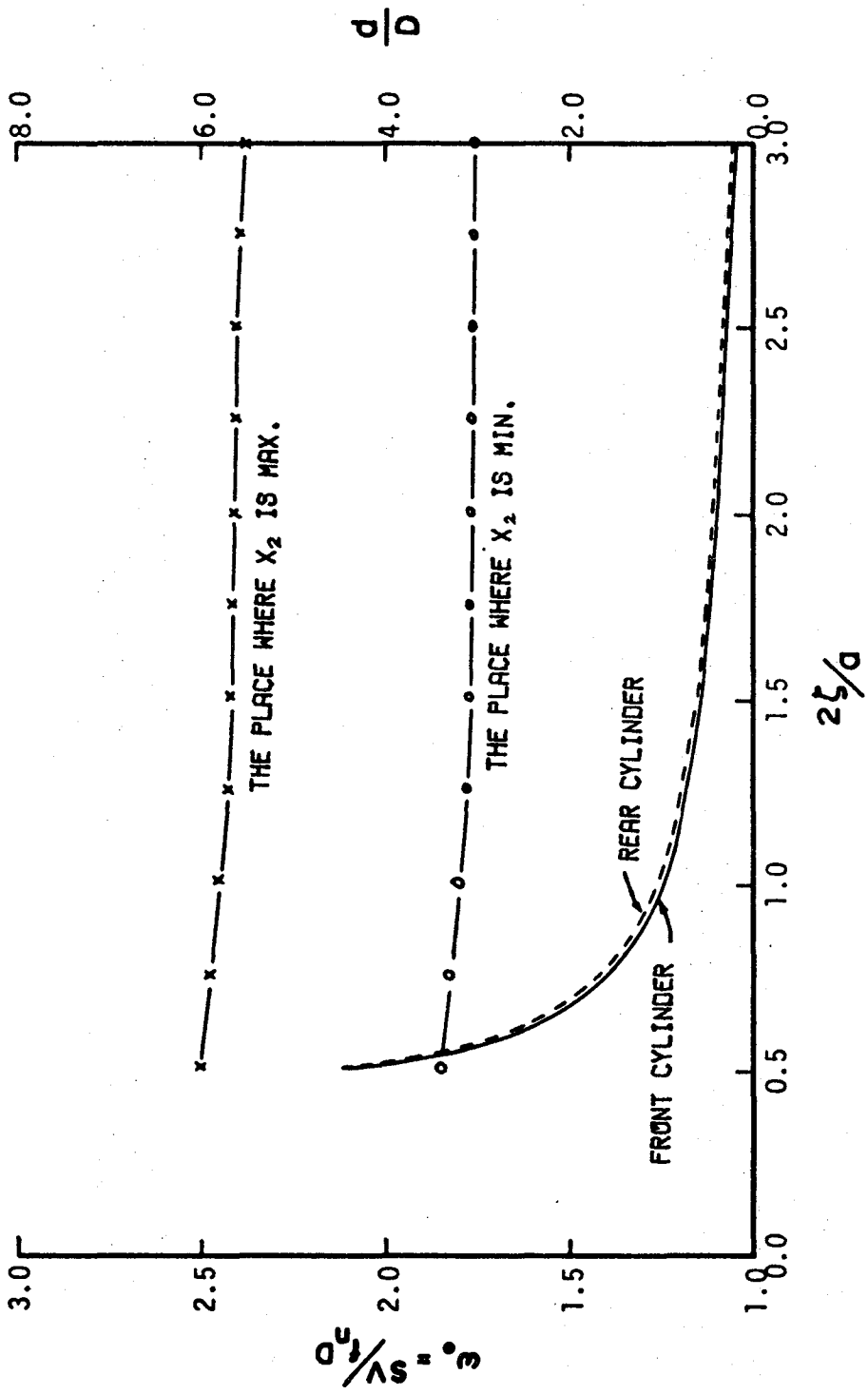

Figure 9. Wind speed versus damping/mass ratio.

The curves shown in Figures 10, 11 and 12 give ranges of ζ, α and b that the amplitude of cylinder vibration will not exceed a definite value assigned. For instance, if one wants the amplitude of a cylinder motion restricted in a range not larger than the cylinder diameter, the ratio of damping coefficient ζ to mass parameter a should be greater than 1.6, α greater than 0.03 and b less than 0.35.

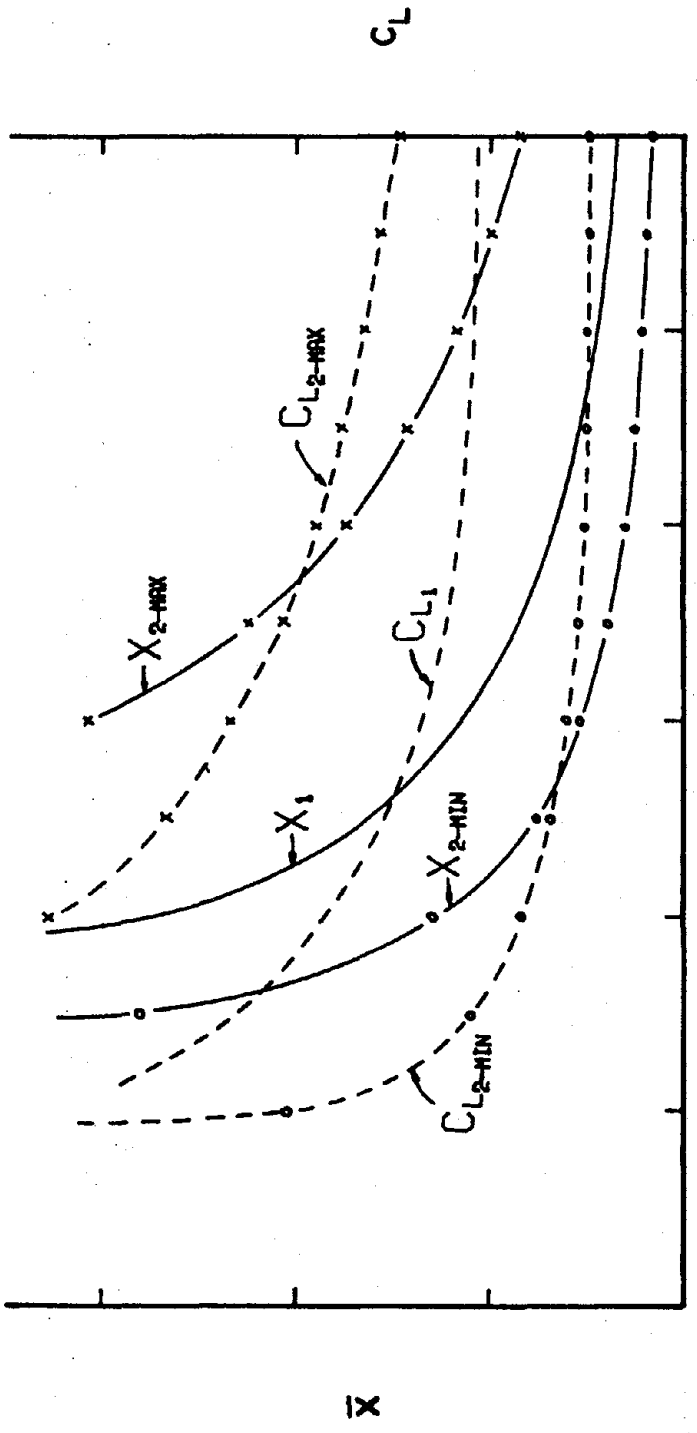

Figure 10. Cylinder amplitude versus damping/mass ratio.

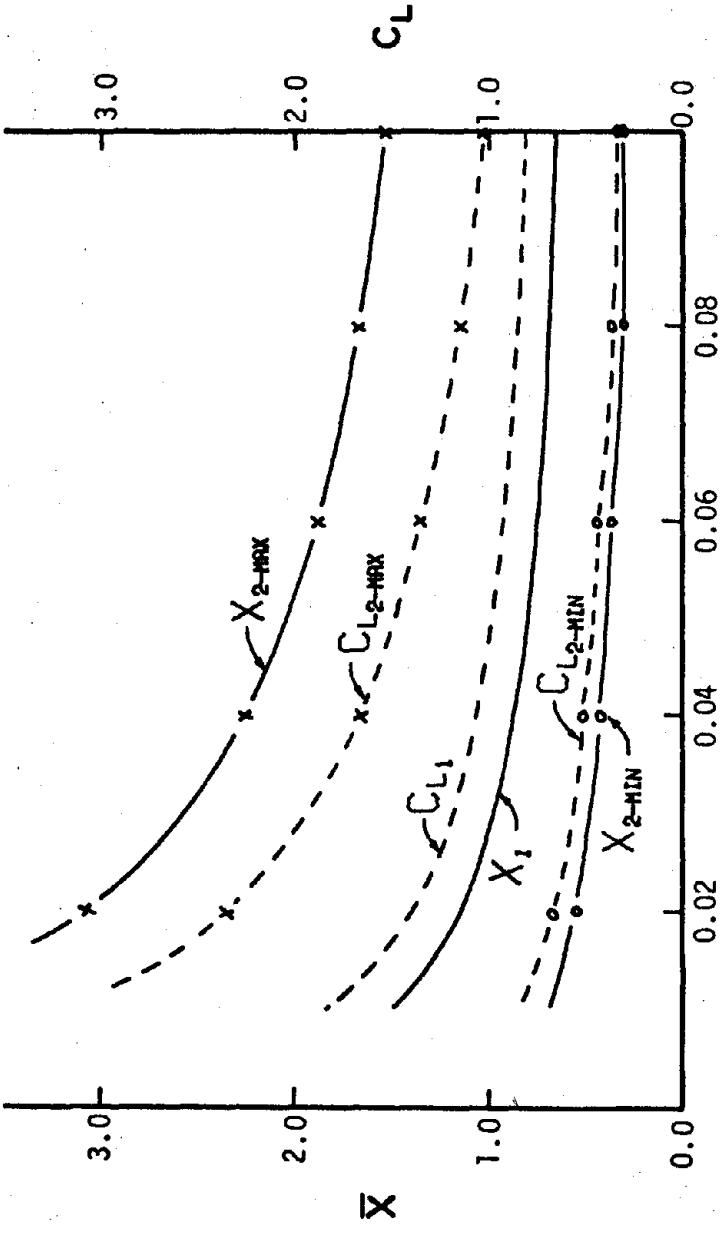

Figure 11. Cylinder amplitude versus α.

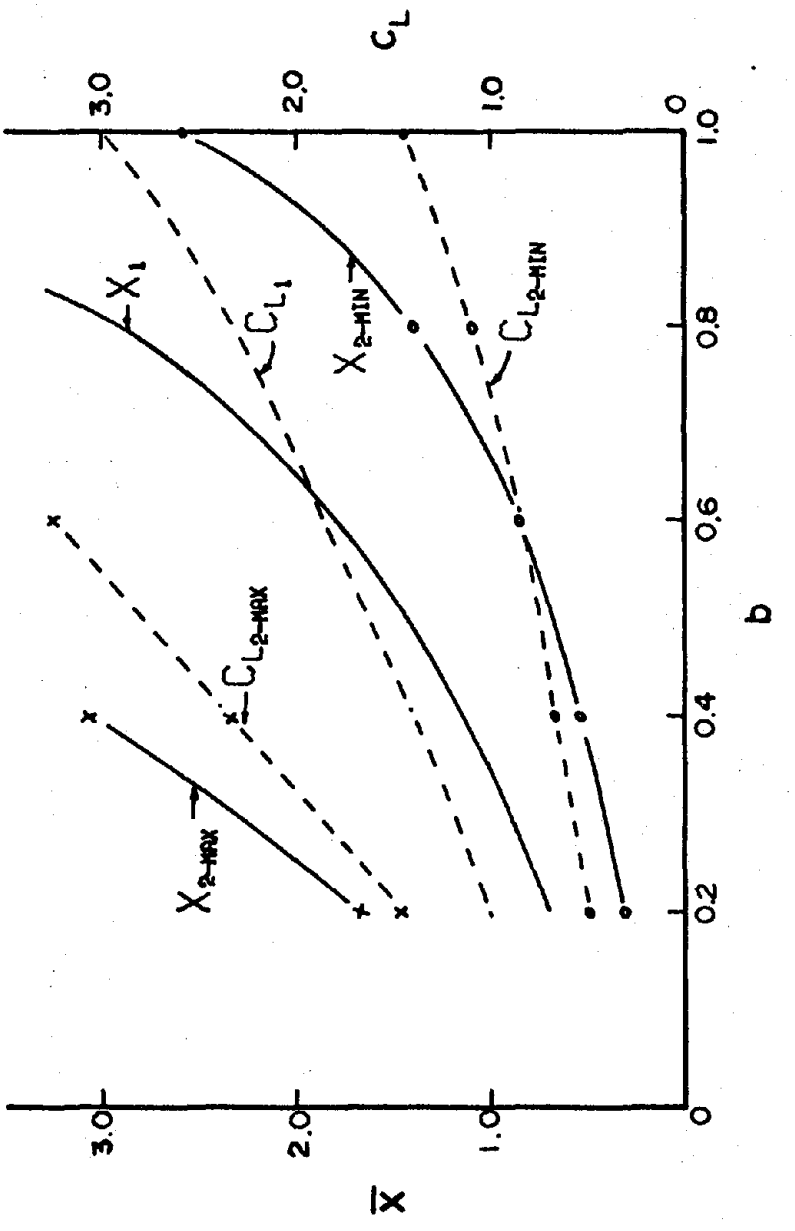

Figure 12. Cylinder amplitude versus interaction parameter.

VI. Summary and Conclusions

A mathematical model that enables one to predict the vortex-excited resonant response of two cylinders in line in the wind direction has been introduced and developed in the present investigation. The model is semiempirical, thus relying on the experimental results for the determination of the introduced constants. In the model a modified van der Pol equation is employed to govern the fluctuating lift force on the cylinder and is coupled to the equation for the oscillatory motion of the cylinder.

The model has been successfully used to predict the motion of an elastically mounted cylinder in the wake of another cylinder. The critical distance between the two cylinders for which the amplitude of vibration of the rear cylinder is minimum or maximum can also be determined by the model and the presents results are in agreement with the experimental data.

REFERENCES

1. Sallet, D. W., "The Lift Force due to von Karman's Vortex Wake," Journal of Hydronautics, Volume 7, No. 4, 1973, pp. 161-165.

2. Sallet, D. W., "On the Spacing of Karman Vortices," Transactions of the ASME: Journal of Applied Mechanics, June 1969, pp. 370-372.

3. Mei, V. C., and Currie, I. G., "Flow Separation on a Vibrating Circular Cylinder," The Physics of Fluids, Volume 12, No. 11, November 1969, pp. 2248-2254.

4. Bishop, R. E. D., and Hassan, A. Y., "The Lift and Drag Forces on a Circular Cylinder Oscillating in a Flowing Fluid," Proceedings, Royal Society, Series A, London, England, Volume 277, 1964.

5. Hartlen, R. T., and Currie, I. G., "Lift-Oscillator Model of Vortex-Induced Vibration," ASCE Proceeding, EM5, October 1970, pp. 577-591.

6. Vickery, B. J., and Watkins, R. D., "Flow-Induced Vibrations of Cylindrical Structures," Proceedings 1st Australian Conference on Hydraulics and Applied Mechanics, 1963, pp. 213-241.

7. Mair, W. A., and Maull, D. J., "Aerodynamics Behavior of Bodies in the Wakes of Other Bodies," Phil. Trans. Roy. Soc. Lond. A. 269, pp. 425-437, (1971).